

Fabrication and Characterisation of Silicon Waveguides for High-Speed Optical Signal Processing

Jensen, Asger Sellerup; Oxenløwe, Leif Katsuo; Frandsen, Lars Hagedorn; Pu, Minhao

Publication date:
2015

Document Version
Publisher's PDF, also known as Version of record

[Link back to DTU Orbit](#)

Citation (APA):
Jensen, A. S., Oxenløwe, L. K., Frandsen, L. H., & Pu, M. (2015). Fabrication and Characterisation of Silicon Waveguides for High-Speed Optical Signal Processing. Technical University of Denmark (DTU).

DTU Library Technical Information Center of Denmark

General rights

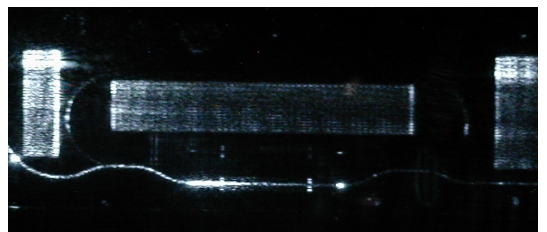
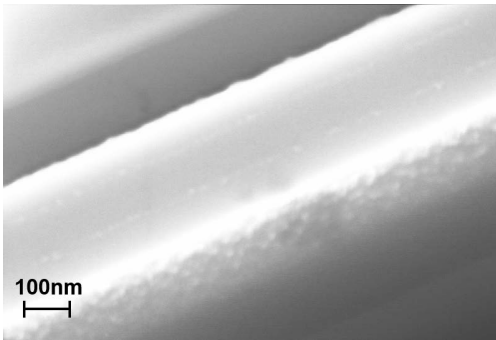
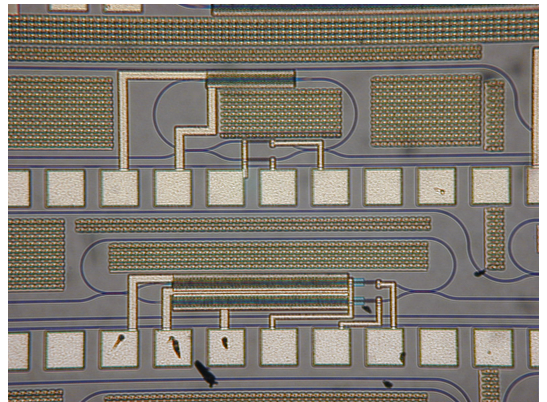
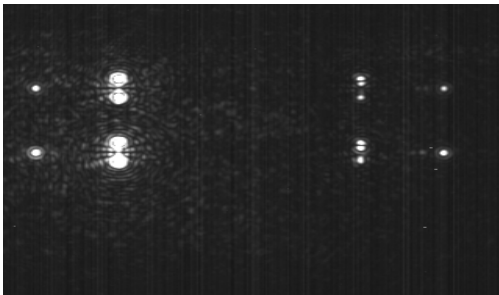
Copyright and moral rights for the publications made accessible in the public portal are retained by the authors and/or other copyright owners and it is a condition of accessing publications that users recognise and abide by the legal requirements associated with these rights.

- Users may download and print one copy of any publication from the public portal for the purpose of private study or research.
- You may not further distribute the material or use it for any profit-making activity or commercial gain
- You may freely distribute the URL identifying the publication in the public portal

If you believe that this document breaches copyright please contact us providing details, and we will remove access to the work immediately and investigate your claim.

Ph.D. Thesis
Asger Sellerup Jensen

Fabrication and Characterisation of Silicon Waveguides for High-Speed Optical Signal Processing



November 2015

DTU Fotonik
Department of Photonics Engineering

Contents

Preface	ix
Abstract	xi
Resumé	xiii
Acknowledgements	xv
Introduction	xvii
1 Silicon waveguides	1
1.1 Waveguide configurations	1
1.2 Waveguide design	4
1.3 Waveguide fabrication	7
1.4 Loss in silicon waveguides	8
1.5 Sources of surface roughness	9
1.5.1 Polymer aggregate dissociation	11
1.5.2 Resist reflow smoothing	14
1.5.3 Semi isotropic plasma etch	18
1.5.4 Isotropic oxidation with buffer oxide	21
1.5.5 DUV stepper lithography	24
1.6 Amorphous Silicon Waveguides	24
2 Nonlinear Signal Processing in Silicon Waveguides	31
2.1 Nonlinear effects in silicon	31
2.2 Signal regeneration using XPM	32
2.3 Wavelength conversion of Nyquist DPSK signal	36

3	Silicon Nitride Waveguides	43
3.1	Hybrid nitride waveguide	44
3.2	Coupling modulated ring model	52
3.3	Hybrid phase shifter fabrication	58
3.3.1	Silicon nitride deposition and stress compensation	59
3.4	Loss characterisation of hybrid waveguides	62
3.4.1	Transition loss	71
3.5	Thermooptic modulation in hybrid waveguides	75
3.6	Forward bias operation	82
3.7	Linear all-optical modulation in a hybrid waveguide	87
3.8	Summary	94
4	Conclusion	97
A	Transmission model derivation	101
B	Reflow heating simulation	105
C	Thermal simulations of SiN hybrid phase shifter	107

List of Figures

1.1	Four types of waveguides found in integrated photonics . . .	2
1.2	Transmitted power and propagation loss of a 450nm×300nm waveguide	9
1.3	SEM images of a typical Si sidewalls	10
1.4	Illustration of polymer aggregate extraction.	12
1.5	EBL defined line in 110nm thick ZEP520A resist	13
1.6	EBL defined line in ZEP520A, which after development underwent descumming	14
1.7	Conceptual outline of the reflow experiment.	15
1.8	SEM images of ZEP520A resist sidewalls	17
1.9	SEM images of sidewall profiles for 50W, 75W and 100W RIE platen power	19
1.10	Sampled propagation loss as a function of wavelength. . . .	20
1.11	Waveguide oxidized for 18 min at 1100°C after an RCA clean and deposition of 50nm PECVD oxide	23
1.12	scanning electron microscopy (SEM) image of two crossing 300 nm wide lines of developed KRF M230Y on a plain silicon wafer.	24
1.13	Refractive index of the grown a-Si based on ellipsometric data. blue and red plots corresponds to a-Si and c-Si data from Pierce[1] and Aspnes[2] respectively.	27
1.14	SEM image of (a) a bend a-Si waveguide and (b) an adiabatic taper section.	28
2.1	Experimental setup for the signal regeneration.	34
2.2	BER (points) for all channels and linear fits to log(BER) (lines).	35
2.3	V-curve openings for a BER of $2 \cdot 10^{-3}$ and $1 \cdot 10^{-6}$ for all channels	36

2.4	Experimental setup for 320Gb/s wavelength conversion. . .	37
2.5	Spectra at various points in the XPM wavelength conversion setup.	39
2.6	BER curves for a converted and a b2b channel	41
3.1	Conceptual image of the hybrid waveguide phase shifter. . .	45
3.2	Conceptual outlines of a hybrid SiN/SOI waveguide	46
3.3	1D simulation data of (a): TM and (b): TE slab mode electric field intensity profiles	47
3.4	Group index versus wavelength for each of the four fabrication splits	49
3.5	Calculated effective refractive index versus gap width	50
3.6	Overlap factors based on numerical data evaluation of equation	51
3.7	Conceptual model of a coupling modulated ring resonator with a racetrack type resonator	52
3.8	Conceptual image of a ring resonator with a feedback waveguide	56
3.9	Transmission spectrum for the device shown on figure 3.8b .	57
3.10	SiN deposition process steps taken to grow and pattern 400nm SiN on a 300mm wafer.	61
3.11	Measured wafer bow evolution for the deposition process described on figure 3.10	62
3.12	Cross sectional domensions and mode profiles for the TM mode in a): the bus waveguide sections and b): the hybrid waveguide phase shifter.	63
3.13	Transmission spectra for various lengths of paper clip type designs	64
3.14	Transmission spectra for the SOI slab thickness / SiO ₂ gaps shown in table 3.1	66
3.15	Propagation loss for the four (SOI thickness)/(oxide gap) splits	67
3.16	Layout of paper clip site used for cutback loss measurement	67
3.17	The four plots show the fast Fourier transform (FFT) spectra for the transmission plots on figure 3.14a	68
3.18	Envelope (black lines) method applied to the spectrums in figure 3.31.	69
3.19	Illustration of the reflection data problem. The solid black line represents a transmission dataset in the absence of reflections (R=0).	70

3.20	Coupling modulated racetrack ring resonators with heater control of the coupling modulation.	72
3.21	Transmission data for (a): Transmission spectra for the device on figure 3.21a for varying applied heater power to the lower MZI arm.	73
3.22	Insertion loss for the intra cavity hybrid waveguide section around 1550nm	74
3.23	Sample transmission spectra showing a sequence of racetrack resonator fringes	78
3.24	Simulated extinction ratio vs lower arm phase shift modulation	81
3.25	Spectral samples for a single resonance etalon around 1550nm	83
3.26	Measured $ S_{21} $ parameter for two phase shifter lengths. . . .	85
3.27	Detected signal after modulation	86
3.28	TE mode profile and dimensions for the structure that make up the hybrid Si/Si ₃ N ₄ phase shifters	88
3.29	Optical modes at 808nm in a SiN waveguide.	90
3.30	Optical modes at 808nm in a hybrid waveguide.	90
3.31	Coupling modulated ring resonator during operation	91
3.32	Comparison of 808nm wavelength scattering through a hybrid waveguide	92
3.33	Normalized transmission vs. 808 nm laser modulation power.	93
A.1	Conceptual model of a coupling modulated ring resonator with a racetrack type resonator	101
B.1	Simulation box for simulating the thermal distribution. The entire box is 3cm wide and 5.5mm high. The air gap between the chip and the wafer is 250 μ m deep.	105
B.2	Conceptual outline of the reflow experiment.	106
C.1	Simulation window with materials indicated.	108
C.2	Temperature profile and material refractive index change .	109

Preface

The work presented in this Thesis was carried out as a part of my Ph.D. project in the period August 15th, 2012 to November 15th, 2015. The work took place at DTU Fotonik (Technical University of Denmark, Department of Photonics Engineering) and at IBM T. J. Watson Research Center, New York, USA.

The Ph.D. project was financed by the FTP project NESTOR and supervised by

- Leif Katsuo Oxenløwe (main supervisor), Professor, DTU Fotonik, Technical University of Denmark, Kgs. Lyngby, Denmark
- Lars Hagedorn Frandsen (co-supervisor), Senior researcher, DTU Fotonik, Technical University of Denmark, Kgs. Lyngby, Denmark
- Minhao Pu (co-supervisor), Postdoc, DTU Fotonik, Technical University of Denmark, Kgs. Lyngby, Denmark

Abstract

This Ph.D. thesis treats various aspects of silicon photonics. From the limitations of silicon as a linear and nonlinear waveguide medium to its synergy with other waveguide materials. Various methods for reducing sidewall roughness and line edge roughness of silicon waveguides are attempted. The methods include enhancements of etch mask roughness as well as etch isotropy and direct reduction of already present sidewall roughness. Although promising roughness assessments were made based on electron microscopy images it did not translate into significantly lower propagation loss in fabricated silicon waveguides. As an alternative to crystalline silicon waveguides for nonlinear optical applications, amorphous silicon was explored using RF sputtering potentially allowing for low density of detrimental hydrogen content in the final material. Unfortunately, the linear optical loss in the material was too high for any practical applications. It is speculated that the attempt at creating a material with low density of dangling bonds was unsuccessful.

Nevertheless, linear losses of 2.4dB/cm at 1550nm wavelength in the silicon waveguides remained sufficiently low that high speed nonlinear optical signal processing could be demonstrated. This includes four wave mixing based wavelength conversion of a 320Gb/s Nyquist OTDM signal and cross phase modulation based signal regeneration of a 40Gb/s OTDM signal.

Finally, a new type of low loss electrically driven optical modulator in silicon and silicon nitride is demonstrated. The device is an attempt to bridge the gap between the low loss platform of silicon nitride and the electrical capabilities of silicon on insulator. In this hybrid waveguide device, light is modulated via evanescent coupling from a nitride strip waveguide to a charge carrier based PiN modulator in a thin silicon slab. The device is demonstrated in conjunction with a coupling modulated ring resonator, a device which benefits from the low loss characteristics of this type of this hybrid waveguide phase shifter.

Resumé

Denne PhD afhandling omhandler silicium komponenter til optisk signalbehandling. Disse silicium-fotoniske komponenter inkluderer bølgeledere til både lineær og ulineær optisk signalbehandling, samt hybride bølgeledere, der kombinerer siliciumnitrid med silicium. Afhandlingen behandler det lineære optiske tab i silicium bølgeledere, og beskriver forsøg rettet mod at reducere tabet ved reduktion af overfladerugheden på bølgeledningens sidevægge. Dette er forsøgt gennem optimering af fabrikationsprocesserne. På trods af lovende SEM billeder, visende stærkt reduceret overfladerughed, resulterede denne optimering dog ikke i reproducerbar reduktion i optisk tab. En reference bølgeleder har tabet 2.4 dB/cm omkring 1550 nm, hvilket er opnået gennem overfladeoxidering. De opnåede 2.4 dB tab er dog tilstrækkeligt til demonstration af optisk signalbehandling ved høj hastighed. I denne afhandling præsenteres eksperimenter der demonstrerer bølgelængdekonvertering af et 320 Gbit/s Nyquist OTDM data signal baseret på firebølgeblanding. Endvidere præsenteres en demonstration af optisk regenerering af et 40 Gbit/s OTDM data signal baseret på krydsfasemodulation. Sluttelig demonstreres en ny type elektrisk drevet optisk modulator, der benytter en hybrid struktur af silicium og siliciumnitrid. Denne struktur kombinerer det lave optiske tab, forbundet med siliciumnitrid bølgeledere, med det hurtige fase- og absorptionsskift forbundet med krystallinsk silicium med en PiN dotering. Det lave optiske tab, samt muligheden for elektronisk styret modulation, gør denne type bølgeleder særdeles velegnet som komponent i en koblingsmoduleret mikroringresonator, der ligeledes er demonstreret i denne afhandling.

Acknowledgements

I owe the opportunity to work at DTU Fotonik and to write this thesis to the FTP project NESTOR and my supervisor Leif Katsuo Oxenløwe whose guidance along with that of my co-supervisors Minhao Pu and Lars Hagedorn Frandsen, has been essential for the success of this work. The broad scope of this thesis would not have been realised without assistance from my fellow research colleagues at DTU Fotonik. I would in particular like to thank Hua Ji and Hao Hu for their patient help and for introducing me to the work in an optical communication lab. Likewise, I would like to thank my colleagues Molly Piels and Francesco Da Ros for their assistance whenever I needed it, which turned out to be more than a seldom event.

Finally, I would like to thank William M. J. Green at T. J. Watson Research Center for the opportunity to visit and work alongside the IBM research staff for 6 months and the subsequent year of cross Atlantic collaboration.

Introduction

Silicon photonics

Silicon is a group IV element situated in the periodic table just below carbon. Both elements are abundant on earth, but where carbon has been the key building block for life as we know it, silicon has been the key building block in modern electronics and brought us through the digital revolution and into the information age. Silicon acquired its fame as the semiconductor material of choice for transistors, a key component in integrated electronic circuits. However, silicon is not the material with the best electronic properties for the job. Materials such as gallium arsenide (GaAs) has superior key electronic properties for fast electronics[3], but silicon makes up for its shortcomings by being non-toxic, having high thermal conductivity, being able to form a well insulating oxide (SiO_2) and most importantly; it is cheap[4]. It is not so much that the raw material is cheap. Silicon is the second most abundant element on earth by mass, but a lot of expensive processing has to take place before the silicon is pure enough to meet the standards required for electronics. The cost benefits has more to do with the billions of dollars and decades of research that has already gone into perfecting the fabrication processes on the silicon platform[4, 5]. Any new material comes with a similar investment requirement, which is why silicon is still a key material and most likely will remain so for a foreseeable future[6]. Regardless of the material used for transistors and the speed at which switching operations are possible, the problem of transporting high frequency electrical signals around, even on the chip to chip scale remains. Metallic circuitry has the unfortunate property that the bandwidth of a circuit is inversely proportional to the electrical impedance. Optical signals (typically in the near infrared spectrum) guided in media such as optical fibers does not suffer from this limitation. Bandwidth is instead limited by dispersion and non-linear effects. This has, over the past few decades, led

to optical fibers being implemented in applications from long haul transmission between continents[7] over thousands of kilometres to ever shorter distances, and is today widely used for communication between nodes in data centres and supercomputers[6] with spans as short as a few metres. Its utility does, however, not end there. The increase in global internet traffic demands, that data centres increase their capacity even further, without consuming the entirety of our global energy resources in the process. An obvious next step is to move optical communication with all its advantageous properties closer to the electrical processing taking place in the CPUs and perhaps, in time, take over some of the signal processing itself. As we move optical communication closer to the CPU, memory etc. more functionality on a limited space is required. Optical fiber technology may be the power horse for hauling data from metres to thousands of kilometres, but it is too bulky for the required functionalities that needs implementation over the distances of a few centimetres available in data center nodes.

Enter integrated silicon photonics. As an optical material, silicon is transparent to the same telecommunication wavelengths as the optical silica fibers most commonly used. At these wavelengths, silicon has a high refractive index of 3.45 while its oxide (SiO_2) only has a refractive index of 1.45. This high index contrast allows for very compact monolithic integration of silicon waveguides embedded in SiO_2 .

As an optical waveguide material silicon is in many ways a formidable material, but as with electronics, it again comes with reservations. Silicon is an indirect bandgap material, which makes it difficult to design efficient laser sources in silicon. Raman lasing in silicon waveguides has been demonstrated [8], but efficiency remains low. Similarly, detectors for wavelengths longer than $1.1\mu m$ are challenging and proper detector materials such as germanium must be deposited in order to obtain detector capabilities [9]. However, silicon does come with an option for lateral PiN diode formation [10]. A silicon waveguide can thus be fabricated with the waveguide core in the intrinsic region of a laterally formed PiN diode. This allows for the charge carrier concentration to be modulated at high speed. An increase in free charge carriers leads to an increase in refractive index of silicon [11] which may be used to modulate light in a silicon waveguide at high speed and with low power consumption [12]. Chapter 3 of this thesis describes the efforts to migrate this functionality over to a low loss silicon nitride (SiN) platform.

The major advantage of using silicon for integrated photonics, is once again the work that has already been done perfecting the processes around fab-

rication. Especially the introduction of silicon on insulator (SOI) wafers to reduce parasitic currents on the electronic platform opened up to research into silicon photonics. The sudden availability of high quality SOI wafers, meant research into silicon photonics took off.

In 2006 California based company Luxtera announced its first SOI based commercial devices featuring flip-chip bonded continuous wave (CW) light sources in III-V semiconductor material and photodetectors grown in Ge [13]. Since then companies like Acacia Communications and Kotura¹ has entered the market for SOI based transceiver modules and active cables pushing towards >100G Ethernet. This lead to multi-source agreement definitions, such as CFP² [14] effectively creating the competitive environment necessary for widespread adoption of the technology.

Unlike the established companies in the semiconductor industry like Intel, Samsung, Qualcomm etc. the photonic industry is currently dominated by fabless companies. The current integrated photonic applications do not lend themselves to high volume production and for this reason foundry services are essential to the continued growth of the integrated photonic industry [15]. However, this is still associated with significant expenses, as custom processes often needs to be developed. Recently, efforts have been made towards adopting the fabless model from silicon electronics such as the IMEC ISIPP25G from 2014 and the IME A*STAR model library and process design kit for photonics from 2015. Having component libraries with reliable specs and performance is an important step towards streamlining the research, development and commercialisation of silicon photonics.

Nonlinear optical signal processing

Photons are through their elementary particle properties as bosons unable to directly affect one another. Photons can however with their oscillating electric and magnetic fields affect matter and in turn be affected themselves. This light-matter interrelationship allows for one light signal to affect another through its interaction with the medium in which it propagates. For light intensities found in nature the polarization P of a medium

¹Kotura was acquired by Mellanox Technologies in 2013 for \$82 million. Same year Mellanox acquired Danish company IPtronics, another fabless photonics company.

²"100G Form factor Pluggable Multi-Source Agreement. Defines the form factor of an optical transceiver to support 40Gbit/s and 100Gbit/s interfaces for Ethernet, Telecommunication and other applications."

is sufficiently explained as proportional to the electric field E

$$P = \epsilon_0 \chi_e E \quad (1)$$

where ϵ_0 and χ_e are the vacuum permittivity and electric susceptibility, respectively. For very strong electric fields such as those generated by lasers, polarisation behaves in a non-linear fashion due to the electric field dependence [16] of the electric susceptibility at high field strengths.

$$\chi_e = \chi_1 + \chi_2 E + \chi_3 E^2 \dots \quad (2)$$

where the third term represents the Kerr effect. The second term is not present in silicon and silica due to their centro-symmetric lattice structure.

In optical fibers and sub-micron waveguides, light is confined to a very small cross-sectional area and as a result intensities may reach levels high enough for nonlinear effects to become dominant, even for moderate power levels. For silica fibers and silicon waveguides the first nonlinear effect seen, as powers increase is the Kerr effect. The Kerr effect manifests itself as a change in refractive index, which is proportional to the intensity of light and in the direction of the electric field. Nonlinear effects associated with the Kerr effect includes self phase modulation (SPM) [17], cross phase modulation (XPM) [18] and four wave mixing (FWM) [19]. In FWM, as the name suggests, four photons of various wavelengths are involved. If two high-intensity continuous wave beams co-propagate, the Kerr effect allows three photons to mix and form new wavelength components of both longer and shorter wavelengths. If two of the wavelength components coincide, only 3 wavelengths are involved and the process is termed degenerate FWM. FWM is a detrimental effect in optical fiber communication systems employing wavelength division multiplexing (WDM) where different data channels co-propagate in the same fiber, each assigned a different wavelength than the rest. Although the intensity may not be high, the distances used are long, allowing the effect to build up over the length of the fiber. Just as described above, the FWM causes signals at different wavelengths to mix and form new wavelength components leading to cross-channel interference. Since the Kerr index change is induced by the electric field magnitude which oscillates in a light beam, FWM is a phase sensitive process. This makes it useful in applications such as phase sensitive amplification and regeneration [20]. Other uses of FWM includes frequency comb generation [21, 22] and wavelength conversion [23, 24].

In the cases of SPM and XPM a high intensity pulse acts to cause a temporal index change in the shape of the pulse. For SPM the intensity profile

causes a frequency chirp across the pulse which causes the spectrum of the pulse to broaden. This is useful for pulse compression, as chirp may be reversed by guiding it through a dispersive fiber or through on-chip adiabatic dispersion engineering [25]. In XPM, a high intensity pulse causes an index change in the shape of the pulse. However, for XPM the phase change is imprinted onto a another beam of another wavelength and as such is able to transfer data from one wavelength to another.

It should be noted that one of the key reasons for the interest in nonlinear optical communication systems is the speed by which these systems may potentially operate. Modulation of an optical signal using electronic effects in silicon, such as carrier induced absorption and phase shifting, is fundamentally limited by the speed and generation of free electrons in a given medium. Nonlinear optical effects on the other hand is limited by the rate of polarisation of a given medium allowing for ultra-fast optical signal processing [24].

Although the functionalities of nonlinear optical signal processing are vast, there is still a plethora of challenges to be addressed as intensities goes up and size comes down. This thesis explores challenges associated with fabrication in particular of low loss optical silicon waveguides for all optical signal processing in chapter 1 and system level experiments where fabricated devices are used for ultra-fast wavelength conversion and signal regeneration in chapter 2.

Aim of study

Although silicon photonics is making its way into commercial products as described above, it still suffers from shortcomings relative to the high ambitions of the new era of the information age.

The work in this thesis aim to address some of the obstacles faced with current silicon waveguide technology in order to pave the way for nonlinear optics based silicon components. The thesis will furthermore explore potential alternative directions for the integrated photonics platforms that does not necessary employ silicon waveguides, but will build on the processes developed for the CMOS platform.

Chapter 1 describes the efforts towards optimizing the silicon waveguide platform with various fabrication techniques specifically designed to reduce line edge roughness (LER) while maintaining control over the cross-sectional profiles. Chapter 2 contains demonstrations of high

speed nonlinear optical signal processing using silicon waveguides at communication wavelengths. Chapter 3 describes the design, fabrication and characterisation of a hybrid SiN/SOI platform with low loss and high speed modulation capabilities.

The first half of this 3 year endeavour was spent at DTU Fotonik in collaboration with colleagues of both the High-Speed Optical Communications group and the Nanophotonic Devices group on the work found in chapters 1 and 2. The second half of the thesis period was spent in part at IBM T. J. Watson Research Center and in part at DTU Fotonik in close collaboration with the photonics research team at IBM. The result of this collaboration is the work presented in chapter 3.

My Publications

- [1] A. S. Jensen, H. Hu, H. Ji, M. Pu, L. H. Frandsen, and L. K. Oxenløwe, “All-Optical 40 Gbit/s Regenerative Wavelength Conversion Based on Cross-Phase Modulation in a Silicon Nanowire,” in *OptoElectronics and Communications Conference and Photonics in Switching*. OSA Publishing, 2013.
- [2] A. S. Jensen, Leif Katsuo Oxenløwe, and William M. J. Green, “Evanescent field phase shifting in a silicon nitride waveguide using a coupled silicon slab,” *Group IV photoniccs conference*, 2015.
- [3] L. K. Oxenløwe, M. Pu, Y. Ding, H. Hu, F. D. Ros, D. Vukovic, A. S. Jensen, and H. Ji, “All-Optical Signal Processing using Silicon Devices,” in *European Conference on Optical Communication, ECOC*, no. 1, 2014, pp. 18–20.

List of abbreviations

SEM scanning electron microscopy

FWM four wave mixing

EBL e-beam lithography

DUV deep UV

SOI silicon on insulator

LER line edge roughness

SiN silicon nitride

TPA two photon absorption

XPM cross phase modulation

SPM self phase modulation

MZI Mach-Zehnder interferometer

c-Si crystalline silicon

FWHM full width at half maximum

FEC forward error correction

OTDM optical time division multiplexing

WDM wavelength division multiplexing

BER bit-error rate

OFDM orthogonal frequency division multiplexing

EDFA erbium doped fiber amplifier
ASE amplified spontaneous emission
BOX buried oxide
CD-SEM critical dimension SEM
IC integrated circuit
CD critical dimension
RIE reactive ion etch
TDH time dependent haze-formation
FCA free carrier absorption
FCD free carrier dispersion
CVD chemical vapour deposition
LPCVD low pressure chemical vapour deposition
PECVD plasma enhanced chemical vapour deposition
CMOS complimentary metal-oxide-semiconductor
FSR free spectral range
FFT fast Fourier transform
EOE electro-optic effect
TOE thermo-optic effect
FDTD finite difference time domain
EME eigen mode expansion
FDE finite difference eigenmode
CMP chemical mechanical polishing
MRR micro ring resonator

Chapter 1

Silicon waveguides

This first chapter describes the fabrication and characterization of silicon waveguides, intended for nonlinear optical signal processing. The focus is on linear loss reduction through sidewall topology optimization. Fabrication induced roughness is an extensive and multidisciplinary field, why the work here is inexhaustive and supplemented by exploration of accomplishments in literature towards low loss, sub micron waveguides.

1.1 Waveguide configurations

A silicon waveguide consists of a silicon core with a high refractive index of ~ 3.5 at communication wavelengths which are the wavelengths from 1260nm to 1675nm which constitutes the six O, E, S, C, L and U telecom wavelength bands. With an indirect bandgap of 1.12eV which corresponds to a wavelength of ~ 1100 nm, intrinsic silicon exhibits negligible absorption in these telecom bands [26]. Importantly, low absorption at these wavelength is a trait shared with its oxide SiO_2 , which is used for fibers and as a cladding material for waveguides. The C-band around 1550nm is of particular interest for nonlinear signal processing as the power requirements for the nonlinear effects are easily supported by erbium doped fiber amplifier (EDFA)s in this region. Because of this synergy, this work will focus mainly on devices aimed towards the C-band. When surrounded by a lower index material, such as SiO_2 , a waveguide defined in silicon confines light and guides it through total internal reflection[27]. Photonic crystals aside, figure 1.1 shows the generalised cross sections of some of the most common waveguide configurations. For silicon strip and rib waveguides n_1 and n_2 are typically silicon and buried oxide (BOX) respectively. n_3 repre-

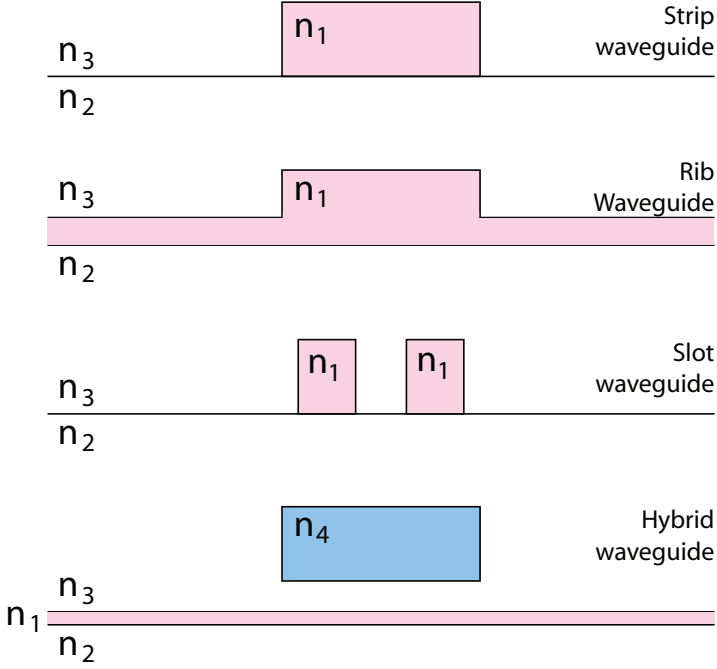


Figure 1.1: Four types of waveguides found in integrated photonics with the exception of the hybrid waveguide. It is seen that the general principle is a high index core (n_1) on a lower index substrate (n_2). The structure is then cladded with another low index material (n_3). In the case of the hybrid waveguide the high index material (n_1) forms a slab and the core (n_4) consists of another high index material with a refractive index between n_1 and n_3 .

sents the upper cladding which could be air but most often its a chemical vapour deposition (CVD) oxide making the refractive indices $n_2 \approx n_3$.

Strip waveguide

The simplest type of waveguide is a strip waveguide, which is a nanowire with a rectangular cross section made in a high index material like silicon, silicon nitride, AlGaAs or similar compounds. The strip is most often cladded with a low index oxide like silicon dioxide. This is not only to hermetically seal and protect the waveguide, but also in order to reduce propagation loss from line edge roughness along the sidewalls. Reducing the index contrast reduces the effect of roughness at the material interface,

which usually is the dominant source of linear loss at moderate intensities in strip waveguides [28]. Although lower index contrast reduces the scattering from roughness, it also lowers the confinement and mode area which is a concern e.g. for nonlinear optical signal processing.

Given the core and cladding material, dispersion is defined by the cross sectional width and height of the core. Obviously, a rectangular shape can be defined in two orthogonal configurations; one standing and one lying down. The standing option is almost never considered for two reasons. First, the vertically aligned rectangular configuration naturally has the highest aspect ratio. The smaller the aspect ratio the easier the dimension control during fabrication. Secondly, the top and bottom surfaces of an etched silicon on insulator (SOI) waveguide are the smoothest surfaces and are often polished to sub nanometer rms roughness [29] in wafer fabrication using chemical mechanical polishing (CMP). These two core/cladding interfaces should thus comprise the largest relative surface contribution to the waveguide, which is why the horizontally aligned waveguide is generally preferred.

Rib waveguides

A rib type waveguide as the one seen on figure 1.1 can be realised in a similar way as the strip waveguide, by only shallowly etching the SOI layer. A disadvantage of the rib configuration is the careful control needed of the rib etch depth. This is a problem in terms of reliability, as etching the correct rib depth without proper monitor equipment can be challenging. Unlike the strip waveguide, the rib does not provide a chemically different etch stop like the BOX. Furthermore, the presence of the slab makes the rib susceptible to bending loss at larger radii than the strip waveguide type, ultimately affecting the density of integration. Finally for integration with electronics or other fully etched features on SOI an extra lithography and etch step is needed to define the rib. These issues are often tolerated as rib waveguides exhibits lower propagation loss [30] than the strip type waveguide due to the smaller waveguide sidewall area. A perhaps more important property, is the option for rib waveguides to have p and n type dopants implanted in the slab, forming a p-i-n (PIN) junction with the waveguide core as the intrinsic region. This allows for modulation through electrical manipulation of the charge carrier density [10, 31]. For nonlinear signal processing a reverse biased PIN junction in the waveguide can be used to extract free charge carriers [32, 33]. Although it does not remove the two photon absorption (TPA), it does prevent the subsequent free carrier

absorption (FCA).

Slot waveguides

Unlike the previous two waveguide examples the purpose of slot waveguides is to confine the electric field of the cladding given by n_3 on figure 1.1. This makes slot waveguides useful for sensing where the cladding could be a gas[34, 35] or a liquid [36] whose optical properties is probed by the mode overlapping with the cladding of interest. The cladding could also be composed of a gain medium in order to achieve amplification [37, 38].

Hybrid waveguide

In this thesis a hybrid waveguide is described. As seen on figure 1.1 it consists of a high index core (n_4) suspended in the cladding (n_3) with a cladding gap between itself and a slab (n_1). Depending on polarisation, this waveguide configuration can be considered a combination of the above three waveguide types. As will be seen in chapter 3, depending on the dimensions employed, the TE mode will take on characteristics similar to the strip waveguide while the electric fields of the TM mode will resemble that of a slot waveguide, the slot being the gap between the core (n_4) and the slab (n_1). The resemblance to the rib waveguide can be seen as the possibility to implant dopants into the slab in order to form a PIN or PN junction, allowing high speed electrical modulation.

1.2 Waveguide design

In order to properly design optical waveguides for any application, one must be aware of the limitations imposed by the available fabrication processes. All silicon waveguides in this chapter are strip type waveguides. Strip waveguides are the simplest waveguides in terms of fabrication as they require only one step of lithography. For strip waveguides the BOX of the SOI acts as a natural etch stop allowing for a higher degree of reproducibility which becomes important when assessing the impact various processes have on the sidewall roughness. Strip waveguides are here considered for their small effective mode area which is an important parameter for nonlinear signal processing as the nonlinear phase shift relates to the intensity of the optical signal and is inversely proportional to the effective

mode area (A_{eff}).

$$\phi_{nl} = n_2 \frac{2\pi}{\lambda} \cdot L \frac{P}{A_{eff}} \quad (1.1)$$

The effective modal area is derived from the transverse electrical field distribution in the waveguide. In sub micron waveguides only few optical modes are allowed. There are various approaches to calculating the mode profiles, all by solving the Helmholtz equation

$$\left(\nabla^2 + k(\mathbf{r})^2\right) \mathbf{E}(\mathbf{r}, t) = 0 \quad (1.2)$$

which can be derived from Maxwells equations and is done so in most books on the subject e.g. [27]. ∇^2 is the Laplace operator, $k(\mathbf{r})$ is the wavenumber which relates to the refractive index n and vacuum wavenumber k_0 as $k(\mathbf{r}) = k_0 n(\mathbf{r})$. If we consider a waveguide cross section in the xy plane we are looking for solutions that propagate in the z direction. Solutions can then be written as

$$\mathbf{E}(\mathbf{r}, t) = \mathbf{E}(x, y) e^{i(-\omega t + \beta z)} \quad (1.3)$$

$\mathbf{E}(x, y)$ describes the mode profile and β is the propagation constant of the mode, which relates to the effective index as $n_{eff} = \frac{c\beta}{\omega}$. Inserting the solution (1.3) into the Helmholtz equation (1.2) yields

$$\left(\frac{\partial^2 \mathbf{E}(x, y)}{\partial x^2} + \frac{\partial^2 \mathbf{E}(x, y)}{\partial y^2} - \beta^2 \mathbf{E}(x, y) + k^2 \mathbf{E}(x, y) \right) e^{-i\omega t} = 0 \quad (1.4)$$

It is clear the time dependence need not be considered in order to solve the problem for the transverse fields. We can then rearrange (1.4)

$$\frac{\partial^2 \mathbf{E}(x, y)}{\partial x^2} + \frac{\partial^2 \mathbf{E}(x, y)}{\partial y^2} = \left(\beta^2 - k^2 \right) \mathbf{E}(x, y) \quad (1.5)$$

This eigenvalues problem allows us to calculate the modal field ($\mathbf{E}(x, y)$) and the propagation constant β for a given wavelength. By calculating the spectral dispersion of β one obtains two other important parameters namely the group velocity dispersion (GVD) often represented by a dispersion parameter

$$D = -\frac{2\pi c}{\lambda^2} \frac{d^2 \beta}{d\omega^2} \quad (1.6)$$

For bulk silicon $D < 0$ for communication wavelengths around 1550nm in the infrared spectrum. Negative group velocity dispersion is called normal dispersion. Confining light in a silicon waveguide alters the dispersion such

that engineering dispersion into the anomalous regime ($D > 0$) as well as changing the zero dispersion wavelength ($D = 0$) is possible.

Unfortunately equation (1.5) can only be solved analytically for simple, i.e. 1D, geometries. Several numerical methods have been developed such as eigen mode expansion (EME)[39], finite difference eigenmode (FDE)[40] and finite difference time domain (FDTD)[41–44] techniques. Common for these solutions are they calculate the field vector at all vertices in a mesh and interpolates the values between the vertive points. This thesis will not treat the algorithms used for these methods as they are beyond the scope of this thesis. Several commercial software solutions exist that employ these algorithms and provide easy to use user interfaces. The designs presented in this thesis have mainly been simulated using Lumerical MODE SolutionsTM.

Confinement factor and overlap analysis

An important parameter when designing and analysing perturbations to the electric field in a waveguide is the confinement factor[45].

$$\Gamma_A = \frac{n_g}{n_A} \frac{\iint_A \epsilon |E|^2 dx dy}{\iint_{\infty} \epsilon |E|^2 dx dy} \equiv \frac{n_g}{n_A} \gamma_A \quad (1.7)$$

Which describes the electrical field E intensity confinement to a given area A . As the mode generally extends into other materials than just the core, the permittivity ϵ is here implicitly considered a function of the spatial coordinates (x, y) as well. The term includes a factor $\frac{n_g}{n_A}$, where n_g and n_A are the group index of the mode and the bulk material given by A respectively. n_A generally refers to the group index as well, but for bulk materials those are often interchangeable. The factor represents a slowing down of the mode relative to the phase velocity in a given material given by its refractive index n_A . This can be explained as any pertubation to the electric field in the structure given by A will be amplified by a slowing down of the signal as it spends more time in that structure than dictated by its phase velocity. The factor

$$\gamma_A = \frac{\iint_A \epsilon |E|^2 dx dy}{\iint_{\infty} \epsilon |E|^2 dx dy} \quad (1.8)$$

represents the spatial confinement of the energy density contribution of the electric field in A relative to the entire structure.

The confinement factor in equation (1.7) is useful for evaluating the impact sidewall roughness will have on propagation loss[46] as the fluctuations in waveguide width, that roughness represents, is seen by the optical mode as perturbations in refractive index at the waveguide sidewall. A high confinement factor at the sidewalls therefore means roughness will be felt more by that particular mode.

The reason it is not sufficient to just consider optical power confinement is the difference in boundary conditions between the electrical and magnetic fields which for sub micron, high index contrast waveguides, such as SOI waveguides, leads to high discontinuities in the electric field at the boundaries[45]. This is an important point to make, as most perturbations in waveguides can be considered perturbations of the complex electrical permittivity $\epsilon = \epsilon_r + i\epsilon_i$ of the waveguide material which strictly relates to the electrical field. This includes electrical and thermal phase modulation (ϵ_r) as well as optical loss and gain (ϵ_i), which has minimal interaction with the magnetic field of an optical mode.

1.3 Waveguide fabrication

The majority of devices fabricated for the work here presented, were fabricated at the DTU Danchip cleanroom facilities. DTU Danchip provides two lithographic patterning techniques suitable for photonic device fabrication; e-beam lithography (EBL) and deep UV (DUV) stepper lithography. A DUV stepper provides fast and reliable patterning and the process itself is fairly cheap once the mask has been purchased. The downsides compared to EBL are resolution, versatility and cost of photo masks. A DUV stepper shines UV light through a reticle with the design, which is then projected onto the wafer coated in photoresist. The SOI wafers used for silicon photonics are expensive compared to plain Si wafers. For that reason it is often not desirable to spend an entire SOI wafer for the purpose of testing small designs. Since DUV steppers aren't designed to accept small wafer pieces, researchers often use EBL to test smaller structures, like single passive waveguide components. Aside from the much smaller features that can be realized with EBL, EBL has the advantage over a DUV stepper that the reticle is defined electronically, as the EBL works by directing a beam of electrons at the wafer exposing an EBL resist point by point. This is of course much slower than DUV exposure in a stepper, but it allows for smaller chip pieces to be used instead of entire wafers and no cost associated with purchase of reticles. For the purpose of this work, the smaller

features available with EBL is less important as the smallest feature in the waveguide designs are the tapers used for coupling light from fibre to the chip. Although they are as narrow as 50 nm in this work, tapers with 100 nm width would only add little to the coupling loss. All silicon waveguides in this work were fabricated using EBL, not only because of the versatility but also for concerns relating to the quality of the available DUV stepper process.

The patterned photo or e-beam resist provides an etching mask for the next fabrication step, where the patterned wafer is exposed to a highly reactive plasma created from a gas e.g. SF_6 or CF_4 . The plasma is typically accelerated towards the wafer and may be aided by passivation steps in forming a highly anisotropic features defined by the mask openings. Finally, the resist mask is removed and an oxide cladding can be deposited using CVD.

Each of these fabrication steps have significant impact on the surface morphology and scattering loss of silicon waveguides. The following sections will discuss various approaches to reduction of scattering loss as a result of fabrication induced roughness.

1.4 Loss in silicon waveguides

Optical loss in SOI waveguides can be divided into two categories; scattering and absorption. For silicon waveguides, scattering loss usually means scattering from line edge roughness (LER), but also includes mode mismatch loss such as the loss associated with coupling between straight and bend sections of a waveguide. Additionally, light may couple across the BOX and escape into the silicon substrate. This is why a thick BOX is necessary for integrated photonics. The required BOX thickness depends on the confinement of light to the waveguide core as the coupling to the Si substrate depends on the evanescent field overlap with the substrate. As such the leakage loss decrease exponentially with BOX thickness [47] and typically become negligible within a few micrometers compared to the other sources of loss discussed here.

Being a semiconductor with an indirect bandgap of 1.12eV, interband transitions for a single photon at typical communication wavelengths are not allowed. However, silicon waveguides usually come with small amounts of impurities that leads to free carriers in the conduction band. These free carriers allow for intraband absorption of infrared wavelengths. For high intensities of light two photons may combine their energy and excite an

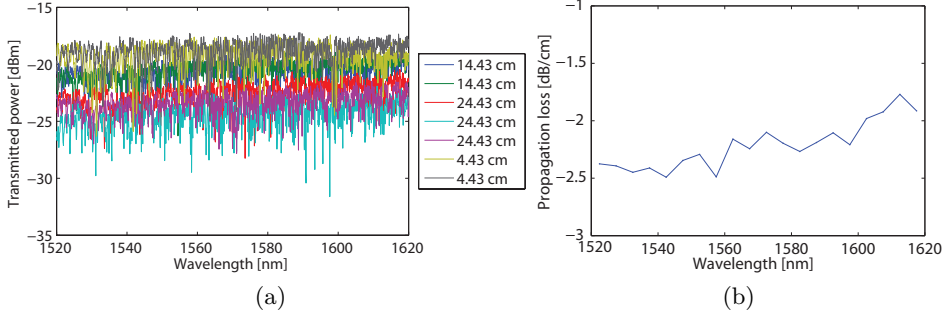


Figure 1.2: Transmitted power (a) and propagation loss (b) of a $450\text{nm} \times 300\text{nm}$ waveguide with a single step oxidation at 900°C for roughness reduction. The apparent noise in the spectra is due to facet reflections from the end facets of the waveguide effectively forming a waveguide Fabry-Perot optical cavity. In order to evaluate the propagation loss in spite of the interfering reflections, the data is sampled as explained in section 3.4 on page 62.

electron across the forbidden energy gap leading to non-linear two TPA and subsequent linear FCA. Although consensus for years have been that TPA sets the main limit on available power in SOI waveguides, recent studies indicate that free charge carriers generated from optical excitation of electrons from interband states at surface defects may contribute to the free charge carrier density by ten(!) times as much as TPA [48]. Improper surface passivation may further induce unwanted free carriers in the form of surface transfer doping, which is largely dictated by the choice of cladding and chemical treatments during fabrication such as etching [49, 50]. It should be noted that absorption through surface states is a single photon process and as such is linear with respect to intensity I , unlike TPA which varies as I^2 .

1.5 Sources of surface roughness

For standard SOI waveguides operated at communication wavelengths, the primary source of propagation loss comes from scattering due to surface roughness on waveguide sidewalls. The polished SOI layer has nanometre smooth surface and BOX-Si interface with rms roughness well below 1 nm [29]. These surfaces therefore contribute very little to scattering loss. In

the case of SOI ridge or rib waveguides the scattering loss primarily comes from the sidewalls. This sidewall roughness is often referred to as LER which is the fluctuation of the edge relative to its design as seen from the top down. As a result, LER is characterised using top-down critical dimension SEM (CD-SEM). This however, does not paint the full picture of sidewall roughness as can be seen on figure 1.3 where typical SOI waveguide edges and sidewalls can be seen captured at a tilted angle. It is clear that important roughness information is lost if only the LER is considered. Only considering LER as a measure of roughness is a practice that likely stems from integrated circuit (IC) research where patterned resist lines can be much smaller than those used to define optical waveguides. For ICs with small critical dimension (CD), the rms of LER can approach the designed feature size. Since LER is the roughness transferred in the reactive ion etch (RIE), dealing with LER is sufficient for IC research. As will be discussed in this section, the conventional, highly anisotropic RIE may not be the process best suited for photonic waveguide fabrication.

First one must understand that the resist used for mask is a polymer resin. The EBL resist used in this work is the ZEP520A chain-scission-type positive resist which is a solution composed of methyl styrene and chloromethyl acrylate copolymer.

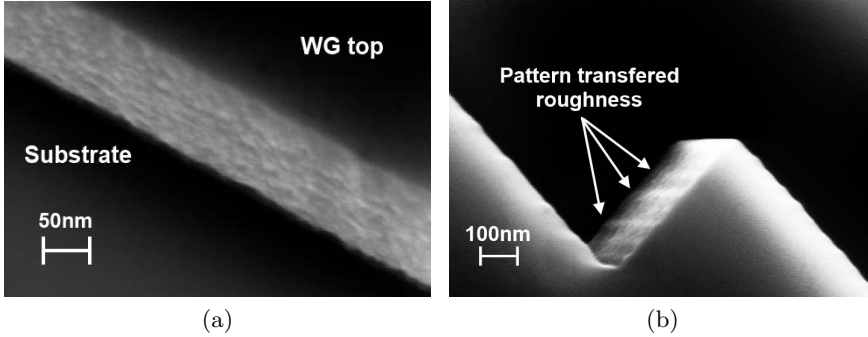


Figure 1.3: SEM images of a typical Si sidewalls showing roughness. LER from pattern transfer is present in both figures but is best seen as the vertical roughness lines indicated on figure (b). The edge on figure (a) shows only little of this, but clearly shows random roughness in both lateral and vertical direction whose source is not direct pattern transfer.

Sidewall roughness comes from fabrication and has several origins and ways to be reduced. The typical patterning technique involves defining

a masking layer of photoresist using a lithographic process, either EBL or DUV, after which the wafer is etched using a RIE. In a RIE process, a plasma of reactive ions are accelerated towards the substrate. Depending on the acceleration voltage and plasma composition, this process can be very anisotropic and transfer the mask features to the SOI with high fidelity.

Any pattern defined by the masking layer is transferred into the SOI layer. This means roughness from sidewalls of the masking layer is transferred as well as the designed pattern, leading to the characteristic vertical lines seen on figure 1.3. Figure 1.3a also shows that direct pattern transfer characterized by the vertical edge features, is not the only source of roughness. The etching process itself adds a significant amount of roughness. Although photoresist masks are chosen in no small part based on their etch resistance, resist will always erode during etching. It is clear that this will contribute to some of etch variation as the pattern being transferred essentially is varying with time.

1.5.1 Polymer aggregate dissociation

A point to be made on resist masks, has to do with the nature of the polymers in the resists. Even if the lithographic process is able to expose a perfectly smooth line, polymer aggregate extraction in the resist will prevent the developed sidewall of the resist from becoming equally smooth[51]. An illustration of the problem can be seen on figure 1.4.

Aggregates in photoresists can be tens of nm in diameter and the issue is the solubility of polymers in aggregates is lower than that of the surrounding polymer[52]. This causes aggregates to stick out of the sidewalls where surrounding polymer has been dissolved but may also leave holes if the entire aggregate is extracted. In order to reduce the impact of aggregates on sidewall roughness of the resist structures, an experiment was carried out where the ZEP520A resin was treated with ultrasound before spin coating. Using ultrasound to dissociate aggregates in solution is a procedure normally used for dissociation of aggregates held together by van der Waals forces, such as protein aggregates, carbon nanotube clusters etc. As can be seen on figure 1.5 there is no visible difference in the resist sidewall roughness as a result of ultrasound treatment. It should be noted that the ultrasound treatment was carried out with an ultrasonic bath which provides quite low and uneven ultrasound transfer to the subject. It seems likely that the intensity is insufficient to break the aggregates apart. For aggregate dissociation, ideally an ultrasonicator dip probe should be used which can be immersed into the resin. On figure 1.5 one may notice the

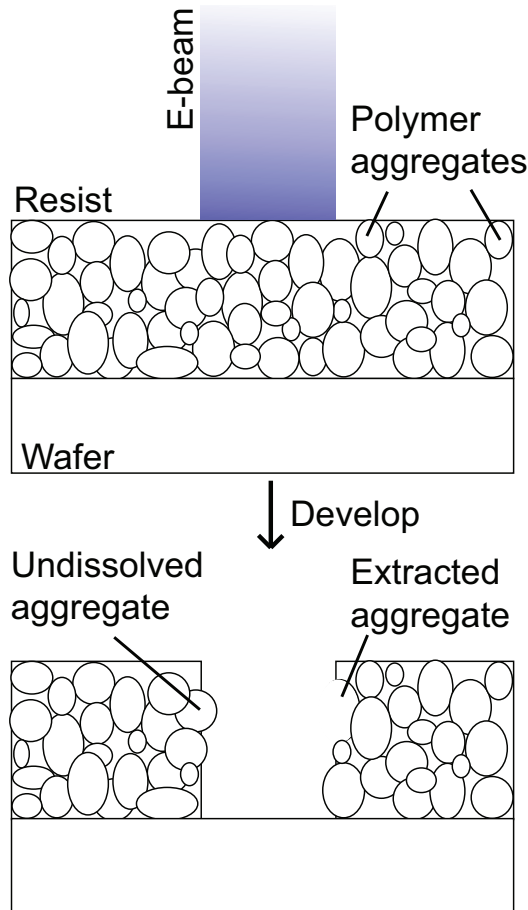


Figure 1.4: Illustration of polymer aggregate extraction. Polymer aggregates are less soluble than their resin suspended counterparts which leaves aggregates at the interface between exposed and unexposed resist either partly embedded in the resist or extracted leaving cavities on the sidewall of the resist.

roughness on the substrate where the resist has been dissolved. This was initially believed to be due to the resist being underdeveloped, but this was ruled out as additional development time does not remove it. Oxygen plasma is used to remove the remaining resist after the SOI layer has been etched, but can also be used to perform a descumming where the wafer is exposed to the oxygen plasma for a short period. As can be seen on figure 1.6a even descumming to the point where the entire resist is virtually gone, does

not remove this roughness. It is thus clear that the roughness is unlikely to originate from the resist. The SOI wafers used for silicon devices in this thesis all come from the same wafer batch and have been more than two years old by the time the picture in figure 1.6 was taken. As a reference an unprocessed SOI wafer was tested and roughness with similar appearance under SEM as that on figure 1.6a is observed on figure 1.6b. The old wafers and appearance of unprocessed wafers could suggest the effect seen is time dependent haze-formation (TDH). Rough SOI surfaces might also help explain why little improvement over legacy SOI waveguide devices is seen in terms of propagation loss, as process optimization is attempted.

ZEP520A may not be the best resist for low sidewall roughness applications. Effects such as polymer aggregation responsible for surface roughness of resists scales with polymer molecular weight[53]. It may seem the obvious solution is to just use low molecular weight polymer based resist, but lower molecular weight polymers has the effect of reducing the development selectivity which itself leads to LER[53]. For the ZEP resist LER has been shown to be reduced by adding crosslinkers to the resist[52] or developing under cold ($<0^{\circ}\text{C}$) conditions[54], although neither has been attempted in this work.

Although ZEP has been used exclusively here, there are promising

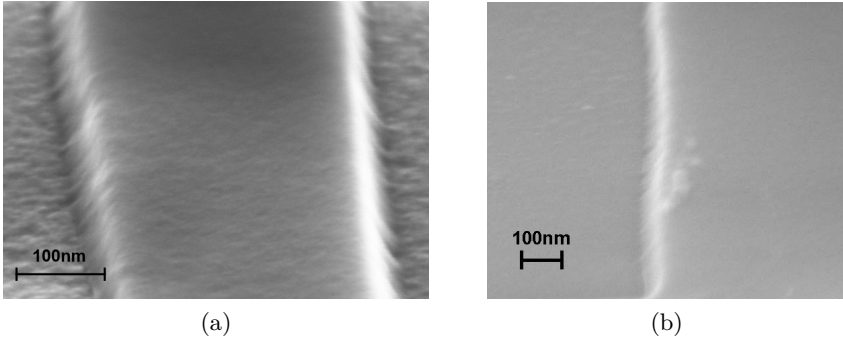


Figure 1.5: (a): EBL defined line in 110nm thick ZEP520A resist.(b): An example of a ZEP520A sidewall after ultrasound treatment of the resin in an ultrasonic bath, patterning using EBL and developing using ZED-N50 for 90s. Even through the poor quality of the image it is seen that the vertical sidewall features from (a) remain with no noticeable difference. The slight curve along the edge is due to shrinkage from e-beam exposure from the SEM

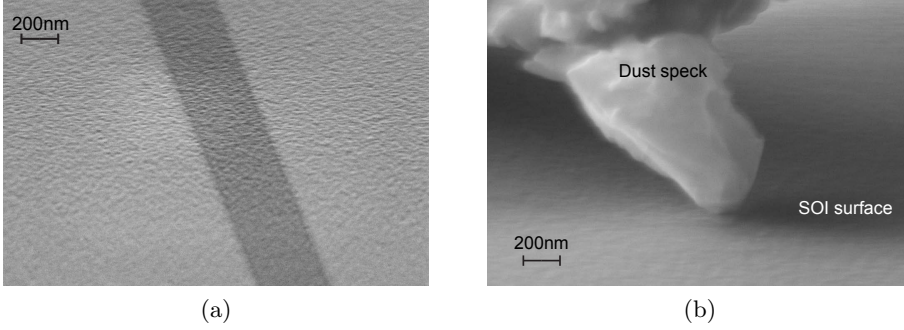
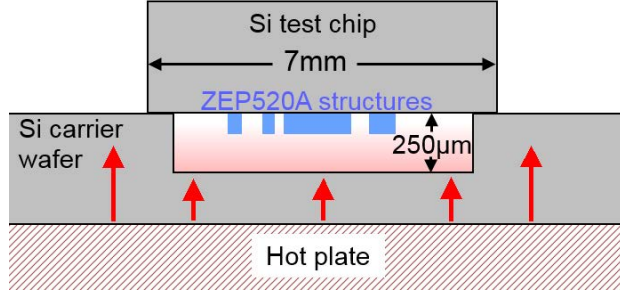


Figure 1.6: (a): EBL defined line in ZEP520A, which after development underwent descumming until almost no resist remained. The dark shadow represents the little resist that remains. (b): Angled SEM of unprocessed SOI wafer with indications of similar surface roughness as seen on (a) even though this image is blurry compared to the image on the left. The dust spec was used for image optimization.

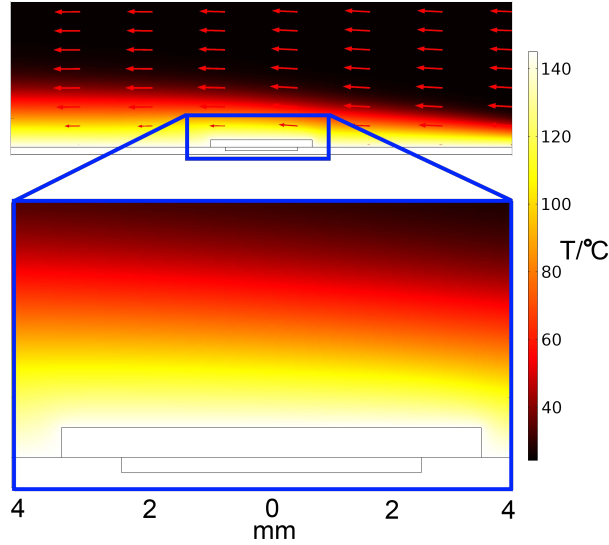
alternatives such as resists employing hyperbranched copolymers[55] or HSQ[56]. HSQ has a 3 dimensional structure and small molecular weight which inhibit aggregate formation[57].

1.5.2 Resist reflow smoothing

Unless the photoresist used, forms crosslinks between the polymer molecules, its viscosity can be controlled with temperature. One way to reduce roughness in photoresist patterns after development is to raise the temperature to the glass transition temperature of the polymers. In a range around this temperature the substance changes its viscosity among other parameters. A rough surface represents a large surface energy which a liquid state substance will smoothen due to surface tension. Reflowing resist patterns around its glass transition temperature has been shown to reduce roughness[58, 59]. Here, this is attempted with the ZEP520A resist where a thin 110nm layer is used in order to minimize the effect of deformation from reflowing. Structures were defined EBL and developed in ZED-N50 for 90s. The sample chips were then placed with structure side down on a preheated wafer with a $250\mu\text{m}$ deep etched trench as seen on figure 1.7a.



(a)



(b)

Figure 1.7: (a): Conceptual outline of the reflow experiment. The test chip is placed upside down on a Si carrier wafer with an etched trench which allows for the air around the ZEP520A structures to reach the reflow temperature and provides some ambient cooling of the chip as the backside is exposed. Relative sizes are not to scale. (b): Finite elements analysis using COMSOL Multiphysics to solve for the steady state temperature distribution during the experiment under typical fumehood air flow. Top image shows the solution for the entire simulation window with red arrows indicating direction of airflow. Bottom image shows a closeup of the structure of interest. Temperature drops less than half a centigrade from the carrier wafer to the exposed test chip backside. Simulation parameters and boundary conditions can be found in appendix B on page 105.

The main reason for placing the test chip as illustrated on figure 1.7a is to provide uniform heating of the resist. The cleanroom hotplates are located in fumehoods with constant air circulation which could cause problems with temperature control had the resist been placed face up. On figure 1.7b a simulated temperature profile is shown for an experiment as described on figure 1.7a where the carrier wafer is placed on a 145°C hotplate under 0.5m/s horizontal airflow and at ambient pressure and temperature. The temperature near the test chip backside exposed to the airflow, deviates from the hotplate temperature by less than half a celsius. The temperature of the stagnant air in the immediate vicinity of the chip backside does not deviate much from the hotplate temperature either. According to this simulation it only drops by $\sim 3^\circ\text{C}$ per $100\mu\text{m}$. This would suggest flipping the wafer is futile. However, reflowing the resist as shown on figure 1.7a has the benefit of protecting the resist side of the chip from particles circulating in the fumehood.

Figure 1.8 shows the effect of thermal reflow of ZEP520A. It is seen on figure 1.9b and 1.9b in particular, that the resist sidewalls have lost their vertical integrity and forms an edge with a very low contact angle with the substrate. In the ideal case the resist would maintain a contact angle $>90^\circ$ after reflow. Low contact angle is a natural consequence of the ability of the resist to stick to silicon and as such is not something that is easily fixed. Since using resists that doesn't stick to silicon is not an option for obvious reasons, what remains is to reflow the resist to the point where the surface of the resist has smoothened but stopping before the bulk of the resist begins to flow. Careful control of the heat profile across the resist or even the wafer using a hotplate is challenging as seen on figure 1.7b. The best option for reflowing resist might in fact be using a high intensity flash lamp which would provide a shallow high temperature flash of heat given the lamp or laser operates at UV wavelengths where the resist absorbs light. This has however not been attempted in this work.

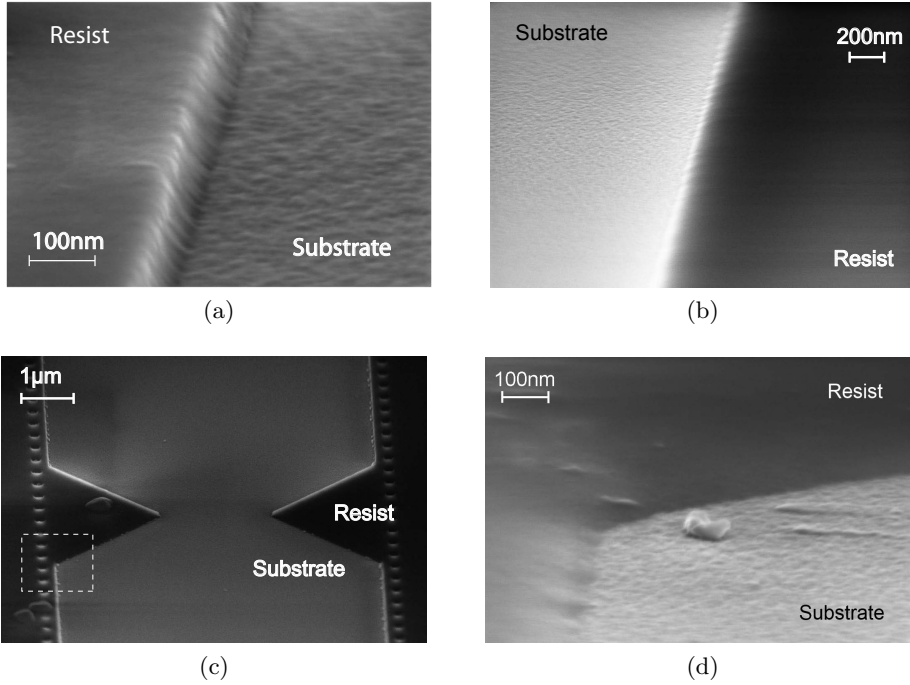


Figure 1.8: SEM images of ZEP520A resist sidewalls of (a): as-developed resist mask showing significant LER along the resist sidewall and (b): after thermal reflow. Although the resist profile has undergone severe deformation due to flow, LER remain visible along the edge. (c): Top-down view of an as-developed ZEP520A test structure. The dashed box corresponds to area of the image shown on figure (d), which shows a close-up of after thermal reflow.

1.5.3 Semi isotropic plasma etch

The way silicon is etched also plays an important role in roughness formation.

The vertical sidewalls shown on figure 1.3 are fabricated using the Bosch process where the etch process cycles between etching using SF_6 and passivation with CF_4 . The SF_6 plasma in the etch is only slowly accelerated towards the wafer. The low acceleration and plasma density causes the plasma to diffuse making the etch isotropic but with enough kinetic energy to sputter off the passivation layer. This creates a number of vertical undulations equal to the number of cycles. Although the undulations are not clearly seen on figure 1.3, the Bosch process is unnecessary for Si thickness well below $1\mu\text{m}$ [60] which single mode Si waveguides necessarily are. Anisotropy of etching with SF_6 is largely governed by platen power, chamber pressure and silicon load. Lower chamber pressure means longer mean free path length and a high silicon load will reduce number of diffusing reactive ions.

The experiment was carried out using a STS MESC Multiplex ICP. Coil power was fixed at 500W and platen samples were etched with 50W 75W and 100W platen power. The size of the test chips used for this experiment was approximately $5\text{mm}\times 5\text{mm}$ which was processed on a 6 inch Si carrier wafer. So even though the chips themselves provided very low Si load, the carrier wafer ensured maximum Si load in the process, promoting anisotropy in the etch. As the equipment does not have etch stop detection, etch rate was determined with a reference run for each platen power level. Profiles of rounded structures can be seen on figure 1.9a. Rounded shapes, such as waveguide bends, are used for sidewall characterisation as they provide a continuum of lattice facets in crystalline silicon (c-Si), so as to reveal any crystal orientation induced effects along the curve.

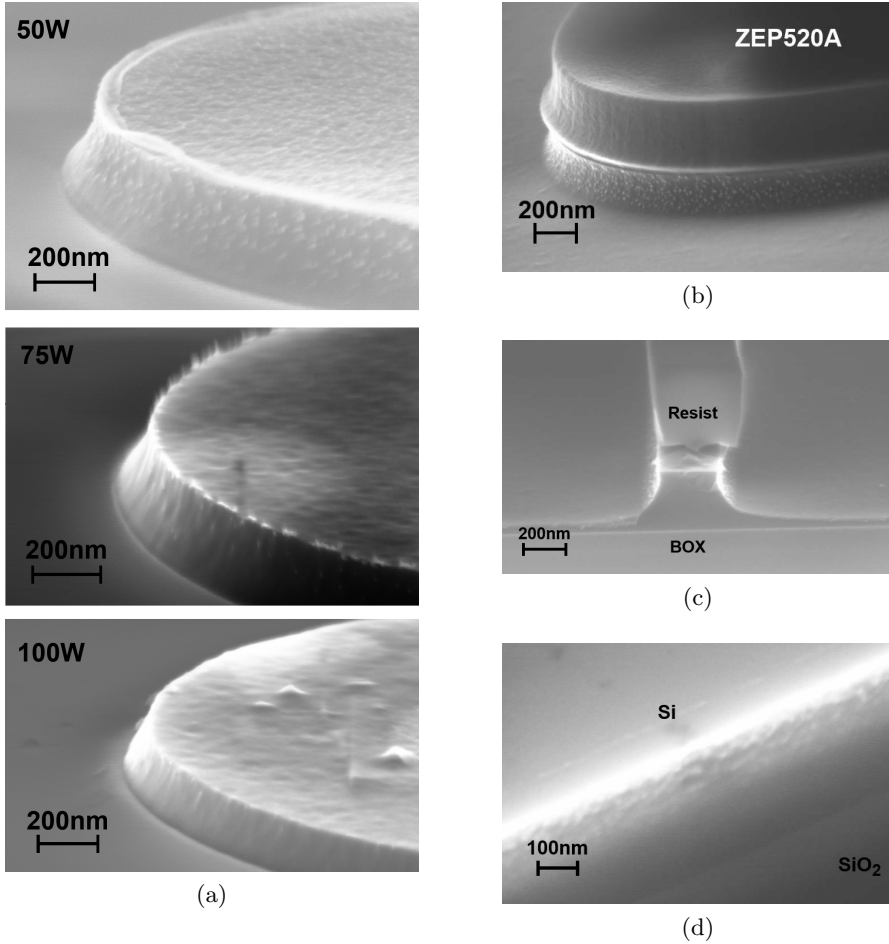


Figure 1.9: (a): SEM images of sidewall profiles for 50W, 75W and 100W RIE platen power with 110nm resist *not* stripped. It is seen that anisotropy increases with power, but so does resist damage. For 100W the resist is mostly gone. In addition, what appears to be resist redeposition seems to be present on the sidewalls, but most notable for 50W. (b): Same structure as in (a) etched at 75W platen power, but with 500nm ZEP520A as resist. Note significant amount of white dots on sidewall assumed to be resist redeposition. (c): Cross section of a nanowire also etched with 75W platen power and resist left on for SEM imaging. The cross section reveals underestimated etching time, evident by the 10-20nm SOI left. Resist is partly peeled off by the cleaving. (d): Nanowire after O₂ cleaning. Significant roughness can be seen along the sidewall similar in occurrence to the redeposited ZEP520A.

It is seen on figure 1.9a that a semi isotropic etch is achieved with increasing anisotropy with increasing platen power. It is also clear from the figure that the standard 110nm ZEP520A mask layer was insufficient for this etch. As can be seen, only little resist remain in all 3 cases. It should be noted from figure 1.9a that almost no roughness of the vertical line type seen on figure 1.3 appear on the sidewalls as a result of the chemical nature of the etch process. However, the absence of this type of roughness reveals a problem with resist redeposition seen as white deposits on the sidewalls on the SEM images. This is seen for all platen power levels, however with highest prevalence at low power and almost none at 100W platen power. This is speculated to be due to the absence of the overhanging mask resist leading to sputtering of the sidewall. For 100W the resist is mostly sputtered away exposing the sidewall to subsequent sputtering. This also explains the low occurrence of redeposition on the lower part of the sidewalls for the 50W and 75W samples, as the lower part seems to extend beyond the protective resist overhang. Regardless of the apparent smoothness of the high power etched profiles on figure 1.9a, using a sputter intensive RIE as in this experiment is not advisable as a post treatment to sputter off resist deposits. Without resist protection, one risks inducing roughness on the very smooth top surface of the SOI layer which is detrimental propagation loss more than what can be gained from improving the sidewalls.

75W platen power is chosen for further waveguide studies as it provides

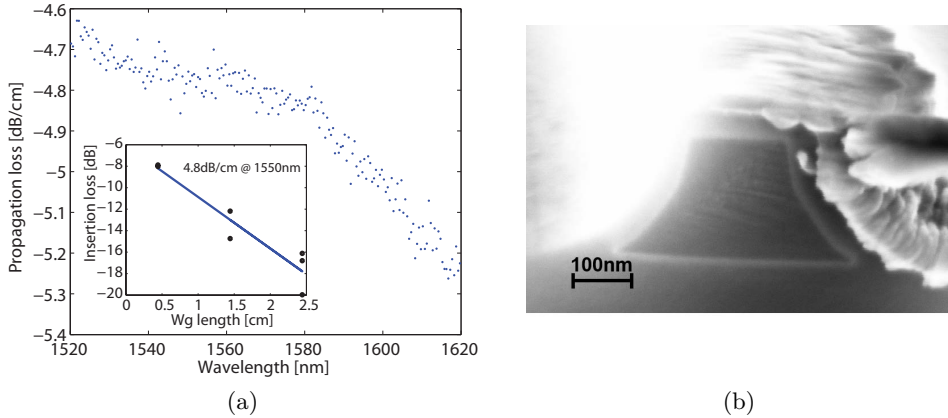


Figure 1.10: (a): Sampled propagation loss as a function of wavelength. Inset shows cutback data at 1550nm with linear fit. (b): Cross section profile of the waveguide with 40nm PECVD oxide for outline contrast.

a good tradeoff with high degree of chemical smoothing while not creating too wide undercuts which would be a problem with slim features like tapers for coupling. Figure 1.9b show a SEM image of the same structure as on 1.9a but processed with 500nm ZEP520A instead of 110nm in order for the resist to sustain the plasma sputtering from 75W platen power. This also means the undercut sidewalls are protected from subsequent sputtering. As a result there is a high occurrence of redeposited resist particles on the sidewalls. The redeposited particles are themselves not a problem as they are removed in the O₂ plasma etch used to remove the remaining resist. The problem is particles deposited on the sidewall acts as tiny etch masks themselves which will transfer to the sidewalls. This is seen on figure 1.9d where O₂ plasma has been used to remove resist from the chip. What remains is roughness with the approximate distribution and size as that seen as resist redeposition on figure 1.9b. Figure 1.10b shows the cross section of a waveguide, patterned as the waveguide on figure 1.9c, but etched through to the BOX and with 40nm PECVD oxide. The etching mask defined a 450nm×300nm waveguide cross section. It is seen that the chemical undercutting has caused a significant dimensional discourse from the mask defined rectangular waveguide. Narrowing of the waveguide ultimately forces the field of the guided mode out of the core and increases the overlap with the surface roughness. This inevitably increases propagation loss. This is seen on figure 1.10b which shows the propagation loss dispersion. Even though roughness assessment using SEM suggest improved surface morphology, the propagation loss lands around 4.8dB/cm for wavelengths near 1550nm.

1.5.4 Isotropic oxidation with buffer oxide

Thermal oxidation of waveguides is a well known way to reduce surface roughness[61]. Oxidation of silicon for oxides thicker than 30nm is described by the Deal-Grove model [62]. The first 30nm of oxide is grown at a rate that starts as high as approximately four times that predicted by the Deal-Grove model[63]. For waveguide fabrication, dimension control is of paramount importance. Controlling the oxide thickness is easiest for dry oxidation and at low temperatures as the oxidation rate has an exponential dependence on temperature. The problem with low temperatures is that the oxidation anisotropy becomes increasingly apparent[64]. This is seen as a sidewall orientation dependence of the oxide thickness and in extension; waveguide width. Furthermore, when thermally growing oxides at temperatures below 1000°C the growing oxide expansion causes compres-

sive stress which may slow down oxygen diffusion[65]. However at higher temperatures viscous flow occur and the SiO_2 grows in a stress free state of with little tensile stress and a more abrupt Si-SiO₂ interface[66, 67].

In order to oxidize at high temperature without the rapid initial oxidation that follows, as etched silicon chips were coated with a 40nm PECVD oxide before oxidizing. This oxide acts as a buffer, slowing down the oxidation. Additionally, PECVD is slightly directional, applying a thicker oxide to the top surface than to the sidewalls means the top surface will be oxidized less relative to the sidewalls. This is an added benefit as the top surface does not need smoothing and will prevent unnecessary silicon consumption. The reason 40nm is chosen is due to the impact correlation length of sidewall roughness has on scattering loss[68]. For waveguide widths around $1\mu\text{m}$ the most detrimental correlation length is between 10nm and 100nm depending on rms of roughness, waveguide dimensions, wavelength and polarisation. In order to smoothen features with long correlation length a buffer oxide of at least similar thickness must be applied. When the oxide is too thin it will cover features much smaller than its thickness, but follow the overall envelope of features with correlation length longer than its thickness.

The waveguides post-processed with this technique were patterned and etched as described in [1.5.3 on the preceding page](#). Propagation loss was measured using the cutback method. The waveguides were designed with a $450\text{nm}\times 220\text{nm}$ cross section and lengths varying from 3mm to 24mm. However as can be seen on figure [1.10](#) the dimensions are distorted in accordance with the etch profiles on figure [1.9](#). Adiabatic tapers with a SU8 mitigation waveguide[69] are used for coupling with lensed fibers which provides a minimum of reflections as well as low coupling loss evident from the insertion loss on figure [1.10a](#).

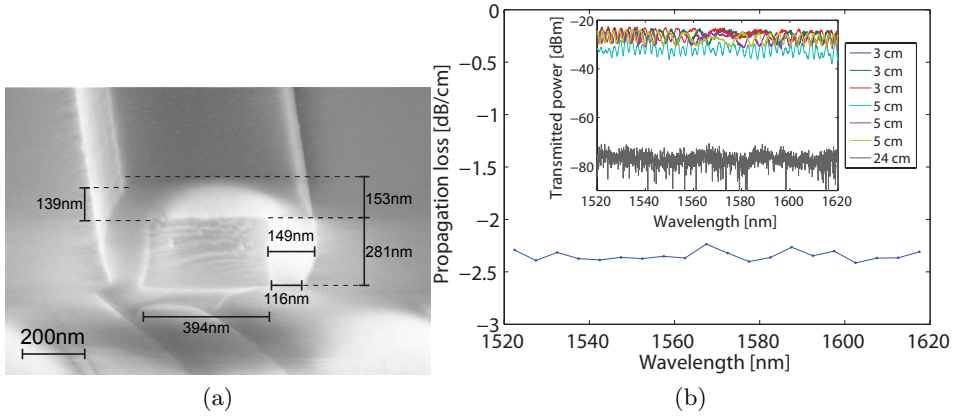


Figure 1.11: (a): Waveguide oxidized for 18 min at 1100°C after an RCA clean and deposition of 50nm PECVD oxide on the sidewalls and $\sim 95\text{nm}$ on the top. 27nm silicon is consumed from the sidewalls, while only $\sim 20\text{nm}$ is consumed from the top surface due to a thicker PECVD top surface oxide. (b): Propagation loss of the waveguides as the one in (a) measured using the cutback method. Due to reflections with extinction of several dB as seen on the inset, the spectral data is sampled as discussed later in 3.4 on page 62.

1.5.5 DUV stepper lithography

The cleanroom facilities at DTU Danchip offers a DUV stepper lithography process using a Cannon FPA-3000EX4 DUV stepper with a KrF excimer laser and 5x magnification using KRF M230Y as resist. On fig. 1.12 a SEM image of a KRF M230Y from this process shows significant edge roughness. Poor edge quality and large minimum feature size of around 200nm, which is too large for optimal coupler designs, makes the available stepper unsuitable for the photonic components fabricated for this thesis.

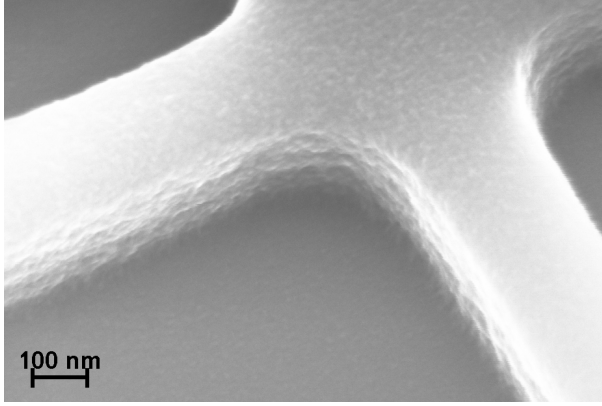


Figure 1.12: SEM image of two crossing 300 nm wide lines of developed KRF M230Y on a plain silicon wafer.

1.6 Amorphous Silicon Waveguides

Two of the major disadvantages with regards to silicon as a waveguide material are TPA which limits its use for nonlinear optical signal processing and its SOI starting material which requires either expensive wafer bonding or SIMOX preparation. Reserving the SOI layer for photonic components additionally means that the real estate cant be used for electronics on the same chip.

A very promising allotrope of silicon is amorphous silicon (a-Si) which has similar refractive index as crystalline silicon (c-Si) but a wider bandgap [70], effectively decreasing the nonlinear absorption. As a result FWM experiments in a-Si has been demonstrated[23] and shows promising results. A great advantage of a-Si is that it can be deposited on most substrates using a mixture of silane (SiH_4) and H_2 at 700°C in an LPCVD or even

PECVD process at lower temperatures. This leads to hydrogenated amorphous silicon (a-Si:H) where dangling bonds in the amorphous structure is terminated by hydrogen. Hydrogen termination of dangling bonds lower the linear optical loss as unterminated bonds creates interband states allowing light to be absorbed [71, 72]. a-Si:H waveguides have been employed [73]

Unfortunately a-Si:H is unstable and deteriorates when light passes through. The effect is known as the Staebler-Wronski effect [74, 75] discovered in 1976, and manifests as an increase in linear absorption over time due to an increase in bulk defect density of around two orders of magnitude [76, 77]. The effect can however be reversed, but it typically involves heating the photonic chip to around 200°C. This optical instability is the major limitation to a-Si:H as a candidate material for nonlinear signal processing. The nature of the Staebler-Wronski effect is still unknown although there has been several theories since its discovery, attempting to explain the effect. Theories that rely on C, N or O impurities have been shown to be insufficient to explain the high observed absorption [77]. Others have claimed that variation in Si-Si bond strengths in amorphous may lead to photo induced breaking of a Si bond leading to two dangling bonds, however electron spin resonance spectroscopy studies have shown dangling bonds does not come in pairs [78].

One theory called the *hydrogen collision model* [79] suggests that recombination of electron hole pairs may excite mobile hydrogen from the Si-H bonds leaving behind trefold-coordinated Si with single dangling bond. If two mobile H collide they may form a metastable complex leaving two metastable dangling bonds in the Si as well. This is supported by work with NMR spectroscopy that showed indications of formation of a metastable hydrogen complex [80]. To further complicate things, a more recent study suggests that defects caused by micro voids may play a significant role as well [81].

Current consensus thus seems to be, that deterioration starts with optically induced carrier recombination which causes breaking of weak bonds in the amorphous structure including Si-H bonds to form meta stable complexes which can be returned to their original bond configuration through annealing.

Since the loss is so strongly correlated with the density of defects, it makes sense to reduce the amount of dangling bonds and potential dangling bonds in the form of Si-H bonds i.e. promote Si-Si bonds. Fabricating the material with lower density of defects and dangling bonds in many ways

corresponds to making the material more crystalline. This can be achieved both by annealing a-Si and using epoxy or e-beam deposition techniques. Polycrystalline silicon waveguides has been demonstrated but suffers from high propagation loss around 1550nm wavelengths [46, 82].

For this thesis, a-Si waveguides were fabricated on a virgin silicon wafer with 2 μ m thermal oxide, using RF sputtering of silicon. The idea is to *not* introduce hydrogen during the deposition in order to avoid immediate dangling bond termination with hydrogen. This should promote formation of more Si-Si bonds in the absence of hydrogen. Strong Si-Si bonds can be promoted by running the deposition process at the lowest available pressure. This increases the mean free path length of the sputtered atoms which increases their kinetic energy i.e. energy available to form bonds. Promotion of strong bonds can be further enhanced using ion assisted deposition (IAS) where ions are accelerated towards the wafer at lower energy than the sputtering beam. This secondary beam "knocks off" weakly bonded atoms leaving a denser and more crystalline film. The deposition was carried out on a Lesker CMS 18 sputter system. For waveguides 200nm material was deposited at 3mTorr and room temperature. The deposition rate was around 3Å/s.

The resulting material was characterised with ellipsometry. The ellipsometry data is fitted to a Tauc-Lorentz model [83] which does well in describing polarization in amorphous materials. Figure 1.13 shows the fitted refractive index for the DC sputter grown a-Si. The Tauc-Lorentz model estimates the bandgap of the material to be 1.2eV-1.4eV only slightly larger than crystalline silicon. In order to efficiently get rid of TPA around 1550nm it needs to be higher than 1.6eV. Introducing hydrogen gas during the sputter process may further increase the bandgap [84] but it is unclear what effect it might have on the optical stability. Unfortunately this is not an option on the equipment used here. The Tauc-Lorentz model also allows for the extinction coefficient k of the complex refractive index $\tilde{n} = n + ik$ to be determined. However, the Tauc-Lorentz model does not include intraband transitions and as a result does not predict extinction coefficients well for photon energies well below the electronic bandgap energy.

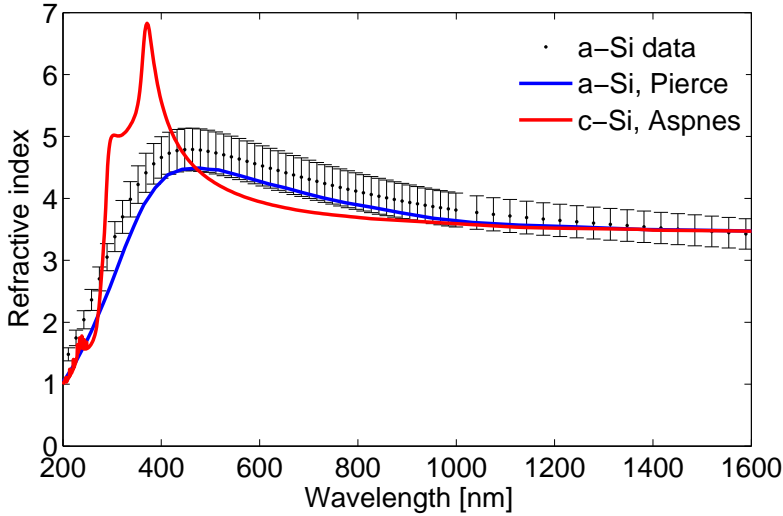


Figure 1.13: Refractive index of the grown a-Si based on ellipsometric data. blue and red plots corresponds to a-Si and c-Si data from Pierce[1] and Aspnes[2] respectively.

In order to estimate the material impact on propagation loss, 540nm wide waveguides were patterned into the 200nm a-Si using e-beam lithography and etched using SF_6 plasma. Finally the waveguides were cladded with $2\mu\text{m}$ PECVD oxide. Characterisation was carried out around a wavelength of 1550nm. Chips were fabricated with both vertical grating couplers and adiabatic tapers for butt coupling. However, efforts to couple measurable light through even the shortest waveguide of 8mm, proved fruitless. This is possibly due to very high insertion loss. Sidewalls were inspected with SEM as can be seen on figure 1.14. The sidewall roughness as seen from the SEM did not differ significantly from what is seen for c-Si waveguides. In addition the top face also appear smooth compared to the sidewalls. This leaves coupling and material loss. both adiabatic and vertical grating couplers were used with designs that typically contributes with 1dB to the insertion loss per transition, when the same design is used for Si waveguides. Since the ellipsometry data suggests similar refractive index at 1550nm it is unlikely that the couplers themselves would be the reason transmission cannot be achieved. Left is the material loss, which suggests the DC sputtered a-Si contain a high amounts of internal scattering sites and/or dangling bond defects. Alternatively, since we are dealing with

plasma sputter deposition there is the risk of metal contamination as well which would significantly increase the propagation loss.

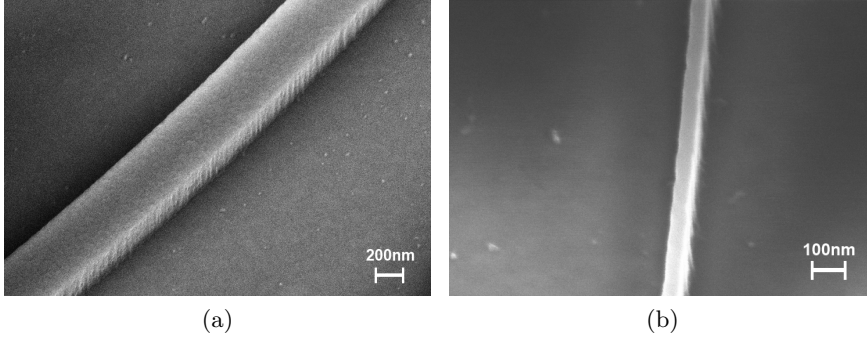


Figure 1.14: SEM image of (a) a bend a-Si waveguide and (b) an adiabatic taper section.

In conclusion DC sputtering of a-Si in order to reduce hydrogen content and dangling bonds does not seem viable with the approach here described.

Outlook and summary

This chapter presents the attempts towards reducing surface roughness on waveguides fabricated using EBL and SF_6 plasma etching. Several approaches are attempted, including resist reflowing, ultrasound aggregate dissociation, semi isotropic plasma etching and isotropic oxidation using a PECVD buffer oxide. Reflowing led to a smoother resist/substrate edge but at the cost of contact angle which was significantly reduced lending the resist near the mask edge prone to erosion during etching. In addition roughness was still present possibly due to polymer aggregates. Dissociation of polymer aggregates in ZEP520A was attempted with ultrasound before spin coating the wafers. Unfortunately no effect was observed on the sidewall roughness. This is either due to polymer aggregate formation after the ultrasound treatment of the resist resin or where polymers in the resin aggregate into aggregates of the same size as before treatment, or the intensity of the ultrasound treatment may have been insufficient. Considering only a ultrasound bath was available the latter explanation cannot be excluded. Ideally, a dip sonicator should be used, if available.

In order to produce smooth sidewalls by modifying the etch process, a semi-isotropic etch was tested. The sidewall roughness was assessed us-

ing SEM. Sidewall roughness was significantly reduced at the expense of disrupted dimensions. The resulting propagation loss was measured to be around 4.8dB/cm which should not immediately be interpreted as failure to reduce propagation loss as the waveguide became narrower as a result of the process. Narrowing of waveguides generally increase the propagation loss as a result of higher mode overlap with the roughness of the surface.

Of the treatments tested here, oxidation using an oxide layer as buffer, proved most promising as a post etch treatment. Although it didn't improve the propagation loss relative to oxidation smoothing without buffer layer, it introduced a convenient way to slow down the oxidation. Slowing the oxidation allows for high temperature (1100°C) oxidation with good dimension control. Although superior to lower temperature oxidation in terms of waveguide deformation, high temperature oxidation is rapid and will consume a significant amount of silicon before a reliable oxide thickness is formed. With the PECVD oxide buffer layer, the initial oxidation rate is controlled by the oxide thickness. In addition the anisotropy of the PECVD process can be used to deposit a thicker layer of oxide on the top surface than the sidewalls which promote oxidation at the sidewalls where smoothing is needed.

Although oxidation smoothing is shown to be successful at reducing propagation loss to around 2.0dB/cm for the waveguide dimensions used in this work, propagation loss is still dominated by surface roughness. If the equipment is available hydrogen annealing where the silicon surface is directly reconstructed at high temperature in a low pressure hydrogen atmosphere, should be considered. With hydrogen annealing it is possible to reduce surface roughness to a level where its contribution to propagation loss becomes negligible compared to material loss[85], albeit at the expense of some structural deformation.

Finally, amorphous silicon (a-Si) is considered as an alternative to silicon. Low propagation loss in a-Si waveguides is not expected. a-Si makes up for high propagation loss with low nonlinear absorption and subsequent FCA. With lower loss at high optical power levels, higher threshold intensities should be achievable. The a-Si presented here was deposited on wet thermal oxide using RF sputtering. Cutback loss characterisation was unsuccessful. It is speculated that the propagation loss due to dangling bond density was too high for sufficient light to pass through the fabricated waveguides.

Chapter 2

Nonlinear Signal Processing in Silicon Waveguides

This chapter describes the use of silicon waveguides as a nonlinear optical signal processing medium. The two experiments reported in this chapter demonstrates both signal regeneration and wavelength conversion of high speed optical time division multiplexing (OTDM) signals.

2.1 Nonlinear effects in silicon

Silicon is subject to Kerr nonlinearities at high intensities of light. The effect derives from the nonlinear susceptibility

$$\chi_e = \chi_1 + \chi_2 E + \chi_3 E^2 \dots \quad (2.1)$$

which relates to the electric polarisation P of a material as

$$P = \epsilon_0 \chi_e E \quad (2.2)$$

Due to the centrosymmetric structure of both silicon and SiO_2 , the second term in (2.1) vanishes, and at the intensities and wavelengths considered here, only the first and third term are observed. The third order susceptibility is responsible for a number of phenomena, including the Kerr effects: four wave mixing (FWM), self phase modulation (SPM) and cross phase modulation (XPM) which are often used in nonlinear signal processing. It should be noted though, that the susceptibility is generally a complex parameter with the imaginary terms representing linear and nonlinear loss terms.

Third order nonlinear loss includes two photon absorption (TPA). Owing to a band gap E_g of only 1.12eV silicon is subject to TPA [86] where two photons with energy $E_{photon} \geq \frac{1}{2}E_g$ combine to excite an electron from the valence band across the band gap and into the conduction band of silicon. TPA of course leads to loss of optical signal power, as it absorbs two photons, but also because the excited electron leads to subsequent free carrier absorption of infrared light through intraband absorption in the conduction band. TPA effectively limits the light intensity achievable in silicon and in extension the power available for nonlinear signal processing. TPA is innate to silicon and is not easily manipulated. Obviously, increasing the wavelength beyond the photon energies required for the TPA alleviates the effect, but is often not desirable. Instead, efforts are focused towards removing the generated charge carriers, using rib waveguides with implanted PIN structures, which when reverse biased, extracts generated carriers allowing for high nonlinear conversion efficiencies [32]. In this work such structures were not attainable and the experimental demonstrations in this chapter uses strictly passive strip waveguides without charge carrier removal.

2.2 Signal regeneration using XPM

The following section describes the successful demonstration all-optical regeneration of a 40 Gb/s signal based on XPM in a silicon nanowire. bit-error rate (BER) measurements show an average of 1.7dB improvement in receiver sensitivity after the regeneration.

Motivation

In long-range communication systems, optical regenerators may play a key role in increasing the data capacity [87]. Regenerative wavelength conversion may also find use in high-performance computing systems (HPCS) and may be of particular interest when performed on a silicon platform [88]. Silicon has a high nonlinear coefficient and a high refractive index and thus allows for very efficient optical signal processing and dense component integration with silicon electronics. The ultra-fast Kerr effect in silicon have been used to realize different functionalities including wavelength conversion and regeneration [24, 88, 89]. In this section the first all-optical regeneration of a 40 Gb/s signal based on XPM in a silicon nanowire is demonstrated. The performance of the regeneration is evaluated with eye diagrams and BER measurements, which clearly reveal the

regeneration performance.

Setup

The silicon nanowire is a $300\text{ nm} \times 450\text{ nm} \times 4.4\text{ mm}$ ridge waveguide with inverted taper couplers [69] for low coupling loss. Figure 2.1 shows the experimental setup for the XPM-based all-optical regeneration of a 40 Gb/s serial data signal using a silicon nanowire. The basic parts include a 40Gbit/s serial data signal transmitter, the silicon nanowire-based regenerator and a 10 Gbit/s receiver. The 40 Gbit/s data signal is here generated by OTDM as seen in ref [90], but with an ERGO laser at 1557nm and a central output wavelength of the transmitter at 1544nm with a pulse FWHM of 1.5ps. The degradation unit is used to add noise to the generated 40 Gb/s data signal. A broadband amplified spontaneous emission (ASE) noise source with power level of 3 dBm is launched into the silicon nanowire together with the data signal. The bias voltage of the Mach-Zender modulator is adjusted to 1.4 V to add “noise” on the ‘0’ level to the data signal. The inset (a) and (b) in 2.1 shows the eyediagrams of the degraded and regenerated data signal, respectively. To regenerate the degraded data signal, a continuous wave (CW) optical signal with wavelength of 1558.1 nm is used as a probe in the regeneration unit. After amplification and filtering, the degraded data signal and the CW probe are launched into the silicon waveguide together, where XPM occurs. Their polarization states are aligned to the TE-mode of the silicon nanowire by using a polarization beam splitter (PBS) and a polarization controller (PC). The average power of data signal and CW probe coupled into the silicon nanowire is measured to 20.9 dBm and 17.5 dBm, respectively. The data signal at the input to the silicon nanowire has a 1.7 ps FWHM pulse width. At the output of the silicon nanowire, a 1 nm OBF is used to suppress the original data signal. After an EDFA, an optical tunable filter (OTF) is used to filter the XPM product at the long wavelength side. A fiber Bragg grating (FBG) is used to remove the CW probe. By tuning the bandwidth of the OTF, the output pulses can have different pulse duration. Here, the bandwidth is selected to 1.2 nm. Figure 2.1(c) shows the spectra measured during the experiment. The regenerated 40 Gbit/s data signal is demultiplexed to four 10 Gbit/s data signal channels by using a nonlinear optical loop mirror (NOLM). Finally, the regenerated 10 Gbit/s data signal is sent into a preamplified receiver and the BER performance is measured.

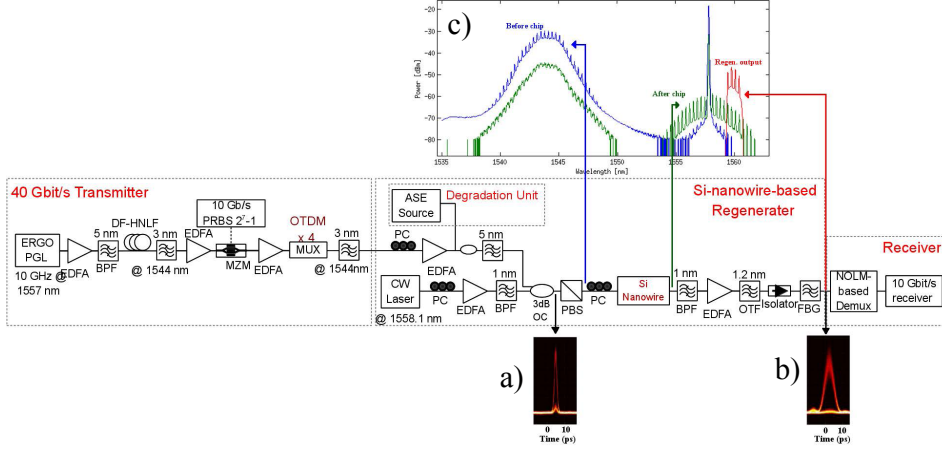


Figure 2.1: Experimental setup for the signal regeneration. The insets (a) and (b) shows the eye diagrams of the degraded signal and the regenerated signal respectively. Inset (c) shows the spectra at (blue): before chip, (magenta): After chip and (red): After regeneration.

Results

BER performance and BER-based V-curves of the degraded and regenerated data signals are measured for all channels before and after regeneration. BER for all four channels before and after regeneration are shown in figure 2.2a. Figure 2.2b shows the receiver sensitivities, extracted from the fitted curves on figure 2.2a. It is clearly seen that the signal BER is improved for all channels by on average 1.7 dB. Note that the channel numbering between degraded and regenerated channels is uncorrelated in all figures. V-curves (BER based) are plotted on figure 2.3a and shows that the 1-level is broadened by the regenerator, while the 0-level is suppressed relative to the degraded signal. This is what leads to the lower receiver sensitivity for the regenerated signal as seen in figure 2.2b. With forward error correction (FEC), a system can operate at high BERs. The dashed lines in figure 2.3a mark BERs of $2 \cdot 10^{-3}$, where FEC would normally be employed and $1 \cdot 10^{-6}$. The widths of the openings in the V-curves are plotted in figure 2.3b. These values represent the tolerated span in threshold voltage at a given BER, and indicate increased performance of the regenerated signal at BERs where FEC would be employed.

The pulse broadening seen on figure 2.1b is a result of the narrow bandwidth filtering seen on 2.1c. As is seen the 3dB bandwidth of the converted

2.2 Signal regeneration using XPM

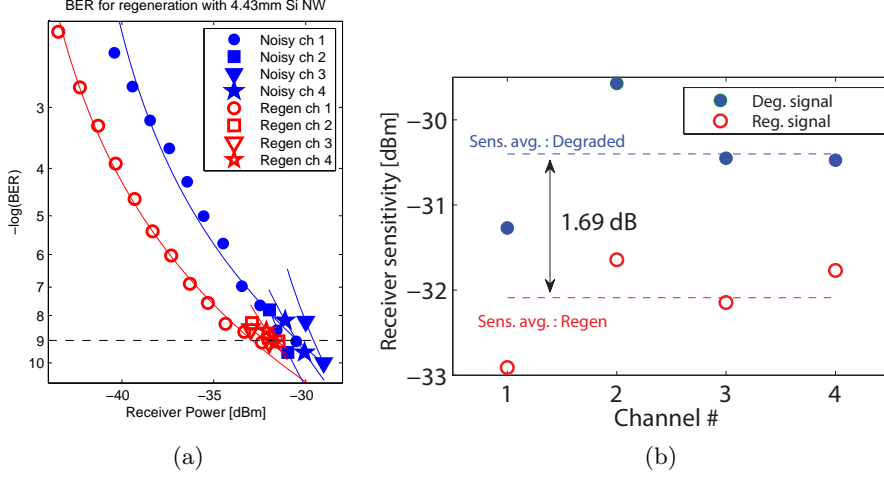


Figure 2.2: (a): BER (points) for all channels and linear fits to $\log(\text{BER})$ (lines). Solid blue points represent BER of the noisy signal and open red points are regenerated data. (b): Receiver sensitivity for all channels at $-\log(\text{BER}) = 9$, showing an average improvement of 1.69 dB for the regenerated signal. The data points are generated from the linear fits in (a)

signal is similar to the original signal. Recovering a narrow pulse from converted signal is thus possible, and would require only a simple notch filtering of the CW pump. However in this case, it would also mean introducing a significant amount of the ASE embedded in the input signal (blue) on figure 2.1c around 1555 nm.

Summary

XPM-based regeneration of a 40 Gbit/s OTDM data signal in a silicon nanowire is successfully demonstrated. All four 10 Gbit/s channels have increased performance after regeneration and an average improvement in receiver sensitivity of 1.7 dB at a BER of $1 \cdot 10^{-9}$. Eye diagrams and V-curves of the signal reveal significant suppression of the 0-level after regeneration. V-curves also reveal a larger span of operation for the threshold voltage both at bit-error-rates of $2 \cdot 10^{-3}$ and $1 \cdot 10^{-6}$.

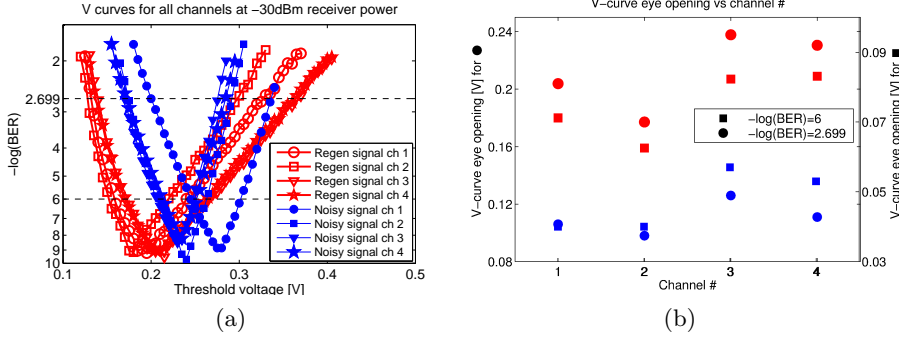


Figure 2.3: (a): V-curve showing how BER changes with threshold voltage for all channels at constant receiver sensitivity. A clear suppression of the 0-level and some broadening of the 1-level is seen for the regenerated signal. Dashed lines mark the BERs of the V-curve opening data plotted in (b). (b): V-curve openings for a BER of $2 \cdot 10^{-3}$ and $1 \cdot 10^{-6}$ for all channels.

2.3 Wavelength conversion of Nyquist DPSK signal

This section describes the experimental demonstration of the wavelength conversion of a 320Gb/s Nyquist OTDM signal. The success of the experiment is attributed to a mere 0.44dB average penalty to receiver intensity relative to the original signal, at the FEC BER limit $3 \cdot 10^{-3}$.

Motivation

Current optical communication systems are under constant pressure from the continuous increase in network traffic [91]. This has in recent years been addressed by e.g. introducing more spectrally efficient data formats, and space division multiplexing to reduce the amount of fibers that needs to be handled. One approach to higher spectral efficiency is to utilize orthogonality between densely spaced channels, either by sinc-shaped subcarriers in the frequency domain, for orthogonal frequency division multiplexing (OFDM), or sinc-shaped pulses in the time domain, for Nyquist wavelength division multiplexing (WDM). Nyquist channels may be made even more spectrally efficient, if they are put on high symbol rates [92], which may be achieved, e.g. by OTDM and optical Nyquist filtering, reaching Tbit/s Nyquist channels [93]. Silicon photonics provides a platform for

high density integration and ultra-fast optical signal processing [94], allowing for switching of highly spectrally efficient data signals. In this paper, we present the first demonstration of FWM based wavelength conversion of a Nyquist OTDM (N-OTDM) signal in a silicon nanowire. We demonstrate wavelength conversion of a 320 Gbit/s DPSK N-OTDM signal with a bit error rate performance far below the forward error correction (FEC) limit for all tributaries, and with less than 0.5 dB average power penalty at the FEC limit. The N-OTDM signal is generated by optical Nyquist filtering an RZ-OTDM signal.

Experimental procedure

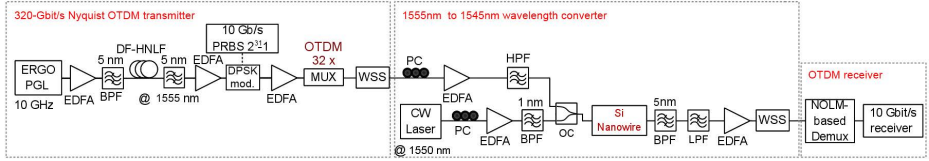


Figure 2.4: Experimental setup. The 320 Gbit/s RZ DPSK signal is obtained by OTDM of a single 10 Gbit/s RZ DPSK channel. A wavelength selective switch (WSS) is used to apply a rectangular filter to the signal after the MUX stage in the transmitter.

In order to create an N-OTDM signal with a minimum bandwidth, the RZ-OTDM signal passes through a Nyquist filter (rectangular filter with a bandwidth equal to the baud rate). This ensures that the tributaries occur at the zero crossings of the neighboring pulses thereby avoiding inter-symbol interference (ISI). The setup used in the wavelength conversion experiment is shown on figure 2.4, which mainly consists of a 320 Gbit/s Nyquist-OTDM transmitter, a silicon nanowire based wavelength converter and an OTDM receiver. In the transmitter, 10 GHz short pulses with a broad spectrum (figure 2.5a 2(a)) are DPSK modulated by a 10 Gbit/s data pattern with a PRBS of 231-1 and OTDM'ed by a factor of 32, resulting in a 320 Gbit/s RZ-DPSK signal. The 320 Gbit/s Nyquist signal is then generated by shaping the RZ-OTDM spectrum using a wavelength selective switch (WSS) programmed as a rectangular filter with a bandwidth of 320 GHz. The generated 320 Gbit/s Nyquist-OTDM signal centered at 1555 nm is then combined with a continuous wave (CW) pump at 1550 nm before coupling to the TE mode of a silicon nanowire using a butt-coupling

scheme. The launched powers of both the signal and the pump are 15 dBm. At the output of the silicon nanowire, the wavelength converted signal at 1545 nm is selected using cascaded filters and then received by a nonlinear optical loop mirror (NOLM) based OTDM receiver. The 320 Gbit/s signal is demultiplexed into 10 Gbit/s tributaries and bit error ratio (BER) measurements are performed. The FWM process occurs in a 6 mm long silicon ridge nanowire with a 514 nm by 232 nm cross section and a 40 nm oxide cladding. Efficient coupling is achieved by using adiabatic tapers with SU8 overlaying waveguides of dimension 3.4 μm by 3.4 μm as a mediating medium. The silicon nanowire is patterned using e-beam lithography and reactive ion etching with a mixture of SF₆ and CF₄. The resulting nanowire has a propagation loss around 4.4 dB/cm and a coupling loss of 1.7 dB/facet. For a pump at 1550 nm, as in this experiment, the 3-dB conversion bandwidth measured under CW conditions is 30 nm at a pump power of 12 dBm. The FWM bandwidth is not as wide as we have previously shown⁴, but the conversion efficiency is higher, enabling wavelength conversion of more spectrally efficient, but OSNR demanding formats like Nyquist channels.

Results

Figure 2.5a shows the spectra for the generation of the Nyquist channel. A broad Gaussian spectrum from a 320 Gbit/s RZ-OTDM data signal is filtered with a rectangular filter yielding the narrow spectrum, as shown in the middle of Figure 2.5a, which clearly shows much improved spectral efficiency. The 6-dB and 20-dB bandwidths of the resulting spectrum are 321 GHz and 330 GHz respectively. Figure 2.5b shows the spectra of the N-OTDM signal and the CW pump at the input to the nanowire together with the output spectrum from the nanowire. A clear rectangular idler spectrum is obtained as a result of the FWM. The conversion efficiency measured at the output is 28 dB. The obtained optical signal to noise ratios (OSNR) are 42 dB for the converted signal and 49 dB of the original signal. Figure 2.5c shows the idler after filtering and pre-amplification in front of the receiver. The 6-dB and 20-dB bandwidths are 321 GHz and 360 GHz, respectively, confirming a good Nyquist signal.

Bit error rate characterisations

The BER measurement of the demultiplexed idler reveals a successful silicon nanowire-based wavelength conversion of the 320 Gbit/s Nyquist-OTDM

2.3 Wavelength conversion of Nyquist DPSK signal

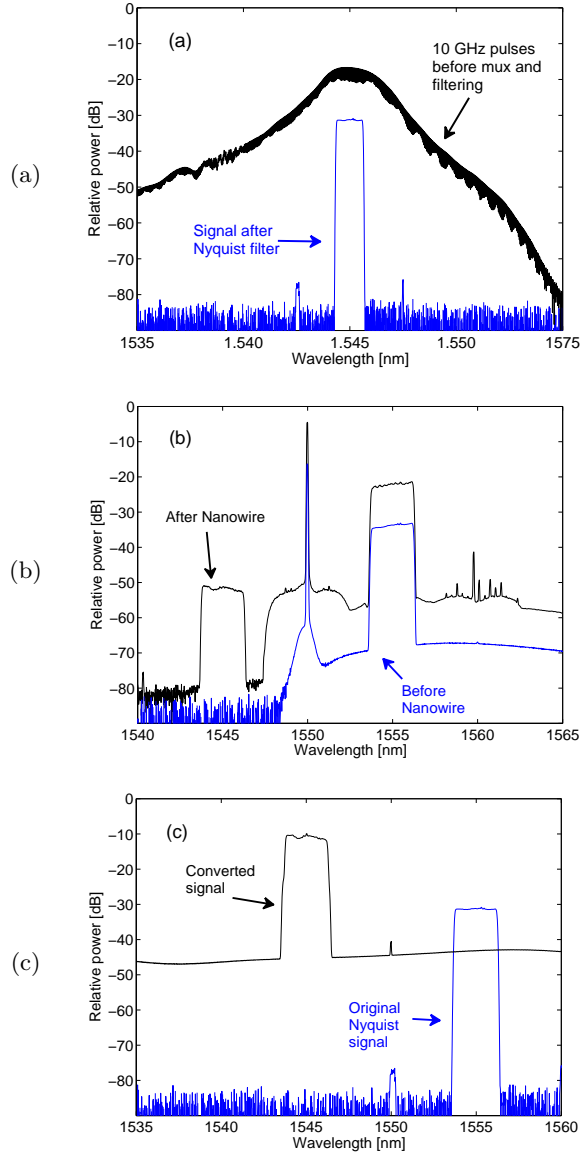


Figure 2.5: (a): Spectra before multiplexing (black) and after multiplexing and Nyquist filter (blue). (b): Spectra before coupling signal and pump into the Si nanowire (blue) and after (black). (c): Spectrum at the receiver (black) plotted with the original signal from (a) for comparison.

DPSK signal. Figure 2.6a shows a BER curve for a 10 Gbit/s tributary of both the back-to-back (b2b) signal and the converted channel, and the converted signal reveals a BER performance well below the forward error correction (FEC) limit of . There is however an error floor visible for the converted signal at a BER around . The error floor for the converted signal is attributed to the degraded OSNR after the FWM as a result of the limited FWM conversion. The degradation of OSNR can also be seen in figure 2.5c, where both the converted and b2b 320 Gbit/s Nyquist signals are plotted. The lower OSNR of the converted signal could be improved by increasing the power into the silicon nanowire somewhat, but in this case the allowed input power is limited by the butt-coupling structure that includes an SU8 polymer waveguide which melts when the nanowire gets too hot. It should be noted that the BER of the converted signal converges with the b2b signal at lower receiver powers, so there is a negligible penalty at the FEC threshold BER of figure 2.6b shows measured receiver sensitivities at the FEC limit ($\text{BER} = 3 \cdot 10^{-3}$) for all 32 tributaries of the b2b and the converted signal. The measured receiver sensitivities in figure 2.6b for the entire range of channels show that all channels are successfully converted with performance at the FEC limit and indeed with similar performance to the b2b signal with an average difference in receiver sensitivity between converted signal and b2b of only 0.44 dB. The data in figure 2.6b shows a spread of about 3 dB in receiver sensitivities between OTDM channels both before and after conversion. Since the deviations of both the converted and b2b data sets are similar, it is expected that the reason lies in the multiplexing of the OTDM signal, since Nyquist shaped pulses will be very sensitive to small displacements in temporal position of the N-OTDM channels. So different tributaries may suffer from different overlaps with neighboring channels, therefore, different amounts of ISI may occur. There is also some difference in power distribution between channels in the multiplexer, which will also result in variations in sensitivity among channels. Nevertheless, the data shows that the entire 320 Gbit/s N-OTDM signal was successfully wavelength converted in the silicon nanowire, thus demonstrating that such spectrally efficient signals can be handled by silicon nanowires.

Summary

We have reported on the first demonstration of wavelength conversion of a 320 Gbit/s Nyquist OTDM signal in a silicon nanowire. The resulting signal showed a performance similar to the b2b signal at the FEC limit of $3 \cdot 10^{-3}$ with an average receiver sensitivity of -43.1 dBm. It was noted

2.3 Wavelength conversion of Nyquist DPSK signal

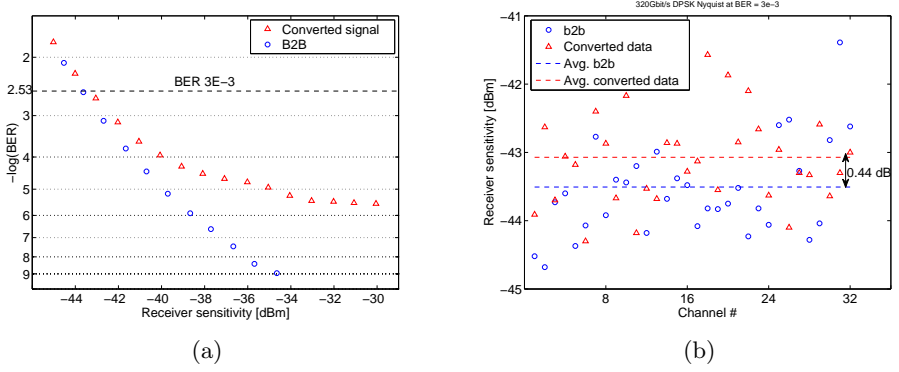


Figure 2.6: (a): BER curves for a converted and a b2b channel showing the error floor being reached for the converted signal at a BER of $\sim 10^{-6}$. It is also seen that the performance of the two signals is similar at the FEC limit $3 \cdot 10^{-3}$ (b): Receiver sensitivities for all 32 Nyquist OTDM channels at a BER = $3 \cdot 10^{-3}$. The difference between the mean values of the b2b and the converted signals is 0.44 dB and the standard deviation of the b2b and the converted signal sensitivities are 0.70 dB and 0.66 dB, respectively.

that the converted signal did not achieve error free performance at higher power levels but hit an error floor at a BER around $1 \cdot 10^{-6}$. This is likely due to ISI of the original signal and degraded OSNR after the conversion which could be improved by increasing the power of the pump and signal into the nanowire, which in this case was limited by the power allowance of the butt-coupling scheme.

Acknowledgements

To the Danish Council for Independent Research (FTP) for support to the NESTOR project and the project Terabit Ethernet on Silicon Photonic Chips.

Chapter 3

Silicon Nitride Waveguides

In order to circumvent the high linear and nonlinear loss in silicon for optical signal processing in waveguides, silicon nitride (SiN) is considered. SiN can be prepared with various compositions. In this work only stoichiometric Si_3N_4 is considered. The abbreviation SiN should thus not be confused with silicon mononitride (SiN).

SiN is a well known material in the CMOS industry where it has been used for many years as an insulator and implant masking material. SiN has gained attention as waveguide material for several other reasons, although it has some shortcomings relative to silicon based photonics. The refractive index is only around 2.0 for communication wavelengths, but the material is transparent for visible as well as infrared wavelengths. The lower refractive index compared to silicon affects waveguide performance through e.g. less dense integration and lower nonlinear Kerr effect. In addition, SiN is an electrical insulator, and does allow easy implementation of active components such as free carrier absorption (FCA) and free carrier dispersion (FCD) based waveguide components, which is easily implemented on the silicon platform. Aside from broadband transparency, SiN offers some key properties that makes it very interesting for waveguide components. First, low loss ($<1\text{dB/cm}$) strip waveguides are easily achieved without any post processing as we shall see. The obvious benefit of low propagation loss aside, the low loss to some extent, alleviates the lower nonlinear effect in SiN, as nonlinear effects SiN can build up over longer distances with lower loss waveguides. Nonlinear processing in SiN waveguides such as frequency comb generation has already been demonstrated[21]. For SiN to truly become a contender as the waveguide material of tomorrow, key waveguide functionalities for communication such as fast phase shift

modulation should be migrated.

3.1 Hybrid nitride waveguide

Since it is not possible to easily induce free charge carriers in SiN, silicon waveguides are sometimes used in conjunction with SiN waveguides to take advantage of its free carrier modulation capabilities and higher thermo-optic coefficient [95, 96]. This is done with adiabatical coupling of light between a SiN waveguide and a silicon on insulator (SOI) waveguide which is patterned in an underlying layer. This does however not solve the problems with propagation loss in the SOI waveguides, and adds coupling loss every time light is coupled between the two waveguide layers. Obviously, since signals can be modulated efficiently in SOI waveguides the SOI waveguide sections can be kept rather short and couplers can be carefully designed to reduce the loss associated with coupling. Lowest coupling loss for C-band wavelengths reported are 0.1dB for coupling in and out of a SOI waveguide with adiabatic coupling to a SiN waveguide [95]. Although this value is low, it is still detrimental when used in combination with ring resonators as is discussed later in [3.2 on page 52](#).

One approach would be to bring a thin slab of SOI in sufficiently close proximity to the SiN waveguide. This can be realised by fabricating the SiN waveguide on an SOI wafer with an oxide spacing layer. The SOI slab can be doped before SiN deposition to form PN junctions below the SiN waveguides where electric modulation is needed. Through careful design, light can be primarily confined to the SiN waveguide and only couple evanescently to the SOI slab. It is here important that the effective index of the guided mode is significantly higher than any non-guided slab modes. The concept is depicted on figure [3.1](#). If the slab mode index surpasses that of the guided mode the guided mode will effectively leak into the slab mode and dissipate.

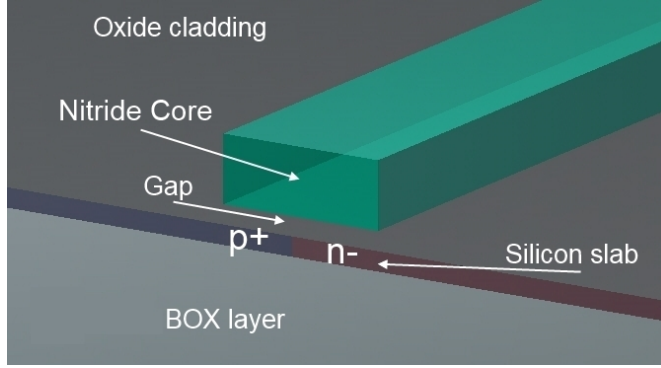


Figure 3.1: Conceptual image of the hybrid waveguide phase shifter. A thin SOI layer with implanted PN junction is either oxidized or oxide is deposited to create a buffer oxide onto which a SiN waveguide is fabricated. The buffer oxide then acts as a low index gap separating the SiN and the active region in the silicon slab. The $p+$ and $n-$ indicates a positive and negative implanted doping impuriti regions respectively.

It is obvious that the efficiency of modulation in this hybrid structure depends on the confinement factor Γ_{Si} in equation (1.7) for the active region in the SOI slab. It is seen that the confinement factor derives from the electric field distribution. Figure 3.2 shows contours of the electric field intensity for a given design used in the experiment in section 3.5 on page 75 where the SiN core cross section is $400\text{nm} \times 1\mu\text{m}$, the gap is 230nm and the slab is 90nm thick. This in combination with the before mentioned slab modes leads to an trade-off since both effective refractive index n_{eff} and the confinement factor Γ_{Si} from equation (1.7) increases with slab thickness. The effective index as a function of slab thickness can be seen on figure 3.3. It is seen that the TE mode has a more significant increase in n_{eff} as thickness of the slab increases than does the TM mode. This becomes impractical when designing devices for TE operation which are typically devices where strong electric field confinement is needed e.g. for dispersion engineering and nonlinear optical signal processing. It should be noted though that for the SiN cross section of $400\text{nm} \times 1\mu\text{m}$ the n_{eff} of the TE slab mode does fall below the guided mode in the hybrid waveguide for slab thicknesses around 50nm and gaps between 50nm and 250nm as seen on figure 3.5a.

The point of this design is to provide the means to modulate light from SiN waveguides at high speed with minimum loss. With low confinement to

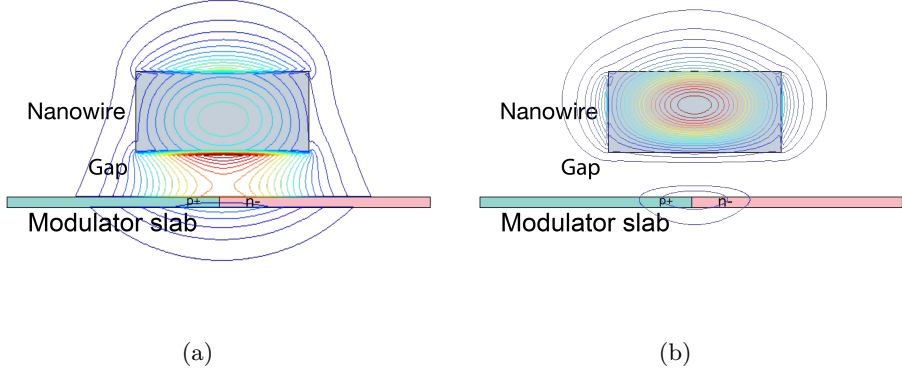


Figure 3.2: Conceptual outlines of a hybrid SiN/SOI waveguide with implanted PN junction in the silicon slab. The SiN nanowire measures $400\text{nm} \times 1\mu\text{m}$ and the slab thickness is 90nm with a gap of 230nm . These dimensions correspond to the ones used for the experiment in [3.5 on page 75](#). Overlaid are contour plots of the electric field intensity for (a): TM and (b): TE polarisation.

the active region the hybrid waveguide would need to be longer which increases the associated loss. This leads to the figure of merit $FOM = V_\pi L \alpha$ where V_π is the voltage required in order to produce a π phase shift, L is the length of the phase shifter and α is attenuation in units of inverse length. Since the evanescent fields only constitute a fraction of the total electric field, the hybrid waveguide phase shifter would need significantly more length than an all SOI waveguide phase shifter. Aside from the additional footprint, the extra length directly translates into insertion loss, defeating the purpose of this endeavour. However, there are devices that do not require a full π phase shift to effectively modulate a signal. These devices are coupling modulated ring resonators and will be discussed in [3.2 on page 52](#).

Figure 3.6 shows overlap factors obtained through numerical evaluation of the expression in equation (1.8) on electric field distributions obtained with MODE Solutions software. The general trend is higher overlap with increasing slab thickness and smaller gaps. According to equation (1.7) the confinement factor is obtained by multiplying the spatial overlap factor with n_g/n_A .

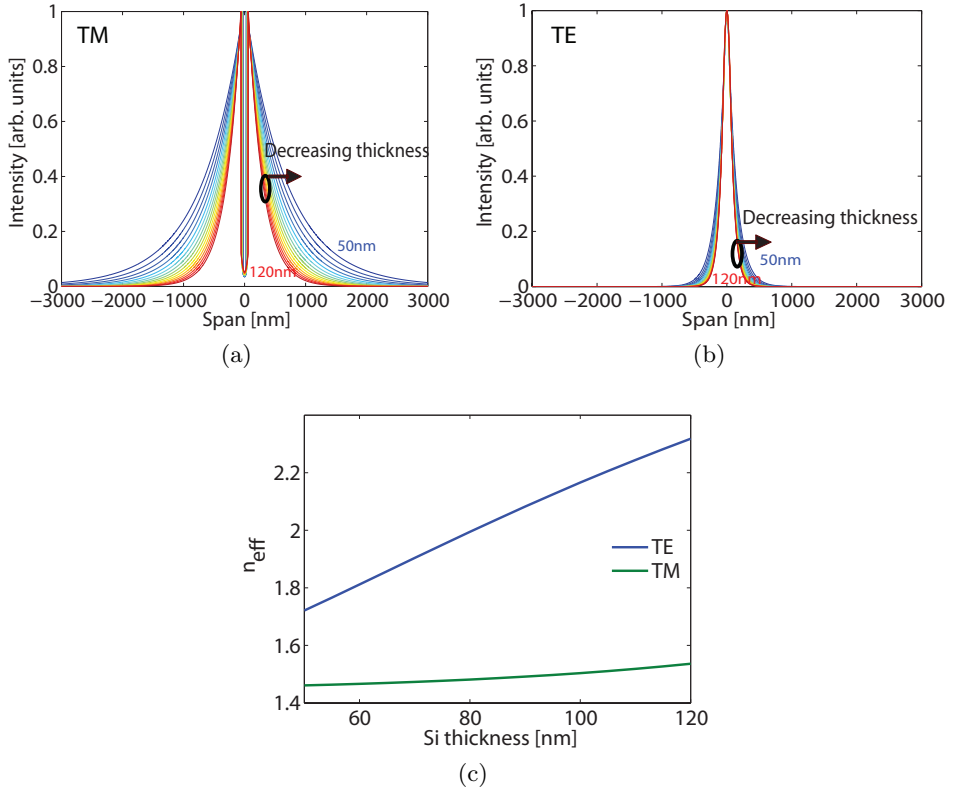


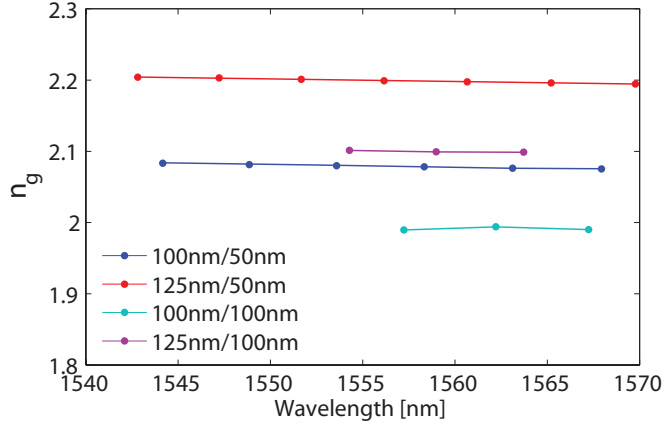
Figure 3.3: Numerical 1D simulation data of (a): TM and (b): TE slab mode electric field intensity profiles for slab widths between 50nm and 120nm. (c): Effective indices for slab modes as a function of slab thickness. Cladding modeled as SiO_2 .

The group index n_g is an important parameter that governs a multitude of fundamental effects other than confinement in waveguide optics, as we will see later. It is probably determined the easiest by using waveguide loaded ring resonators. From the transmission spectra of such devices can be determined from the free spectral range (FSR) as [97]

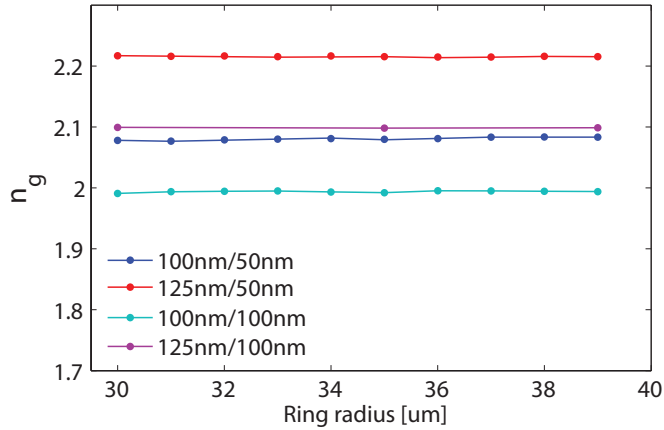
$$n_g(\lambda) = n_{eff}(\lambda) - \lambda \frac{dn_{eff}(\lambda)}{d\lambda} \approx \frac{\lambda^2}{L\Delta\lambda} \quad (3.1)$$

where $\Delta\lambda$ is the FSR in units of wavelength, L the circumference of the ring resonator and λ the wavelength. Ring resonator devices with various splits of SOI/oxide gap thickness, but all with $400\text{nm} \times 1\mu\text{m}$ SiN core were fabricated. The ring resonators were fabricated with varying radii loaded to bus waveguides with a 900nm coupling gap. All waveguide dimensions, both the ring and bus waveguide are defined by the dimensions of that split which are also described in 1.3 on page 7. The measured n_g can be seen on figure 3.4. As is seen on figure 3.4, the n_g turns out fall around 2.1 ± 0.1 for the structure splits presented in this work. The ratio $n_g/n_{eff} \approx 0.6$ regardless of split considered which can be multiplied into the values on figure 3.6 to get an estimate of the confinement factor of the SOI slab.

Unfortunately for this work it was never possible to get a PN junction implanted into the SOI layer directly below the SiN. A series of devices were fabricated at IME Astar on behalf of IBM. The process used at IME Astar only allowed for a PiN junction to be implanted. This allowed me to demonstrate the evanescent coupling in forward bias but restricted the modulation speed to less than 1GHz .



(a)



(b)

Figure 3.4: (a): Group index versus wavelength for each of four fabrication splits of SOI/gap oxide thickness. (a): Group index versus ring resonator radius around a wavelength of 1560nm showing the group velocity for each fabrication split to be approximately constant from 30 μm to 40 μm radius.

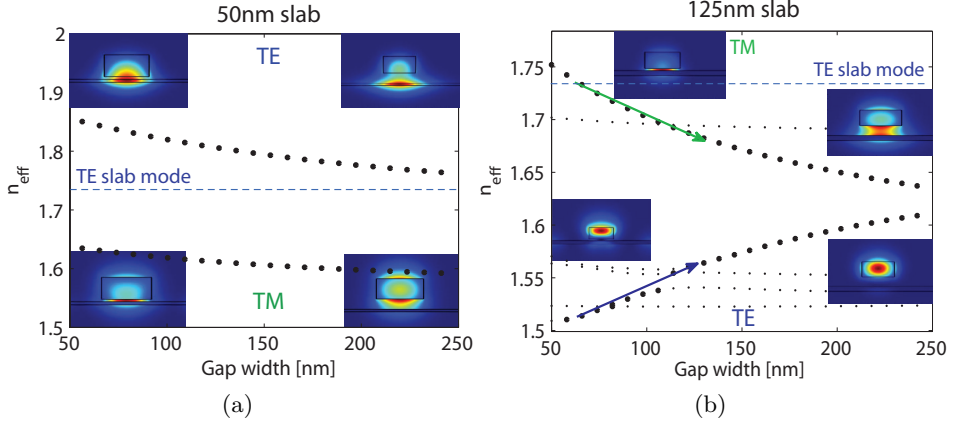


Figure 3.5: Calculated effective refractive index versus gap width for slab thicknesses of (a): 50nm and (b): 125nm. Inserts show normalized electric field intensity profiles for the TE and TM modes at gaps of 50nm to the left and 250nm to the right. The dashed line in (a) indicates the TE slab mode n_{eff} for a 50nm Si slab taken from figure 3.3c. Notice that the TM slab modes fall below 1.5 and are not depicted. The same goes for the slab mode for a slab thickness of 125nm with a n_{eff} of 2.3. The deemphasised points in (b) represents modes that are a result of the reflective boundary conditions and are not guided in the real structure.

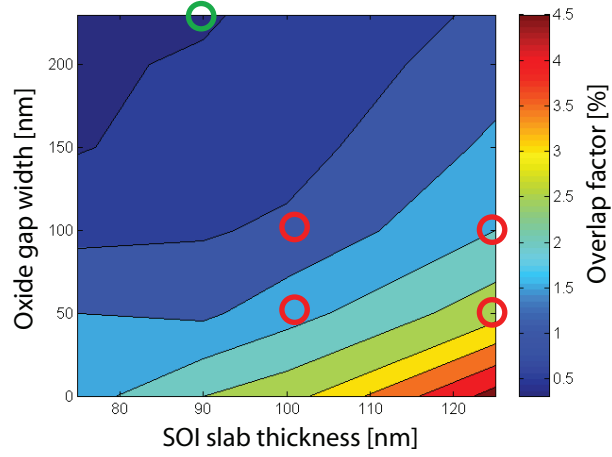


Figure 3.6: Overlap factors based on numerical data evaluation of equation (1.8), versus gap width SOI slab thicknesses for TM polarisation. Marked with red circles are the fabrication splits corresponding to the devices in this thesis fabricated at the MRL cleanroom at IBM while the green circle marks the overlap factor for devices fabricated at IME A*star.

3.2 Coupling modulated ring model

In order to accommodate the low $V_\pi L \alpha$ of the hybrid waveguide introduced in section 3.1, the hybrid waveguide phase shifter may be implemented into a coupling modulated ring resonator device[98–102]. The advantage of this application is that only a fraction of a π phase shift is needed in order to modulate a signal when modulating the coupling coefficient of a ring resonator. Furthermore, this fraction depends on the roundtrip loss of the compound. A way to realise coupling modulation is to incorporate a

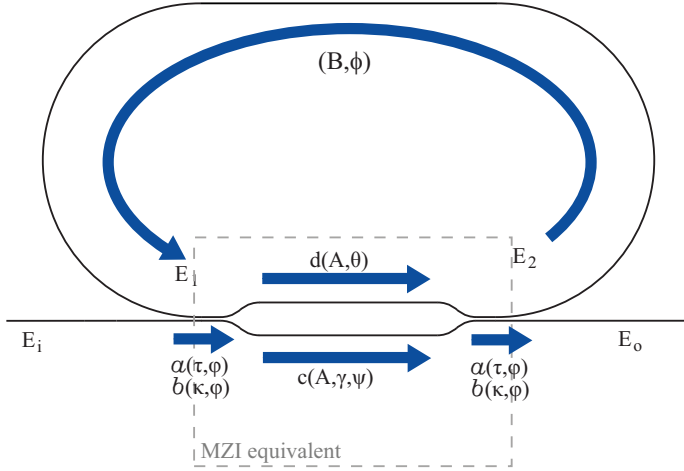


Figure 3.7: Conceptual model of a coupling modulated ring resonator with a racetrack type resonator and MZI coupling modulator. Blue arrows indicate light pathways with their corresponding dependent variables and parameters.

waveguide Mach-Zehnder interferometer (MZI) in the coupling region between the bus waveguide and the ring resonator. This concept can be seen on figure 3.7. Mathematical models for the operation of these types of devices have been constructed. However loss associated with the entire coupling is often omitted[98, 102] as the problem can be greatly simplified this way. However, since the phase modulator which may be the single greatest source of loss, considering an otherwise low loss ring, is placed directly in the coupling region this approach is *not* viable when analysing the impact of exactly the phase shifter. I therefore derive the static input/output relation for the device shown on figure 3.7. Using the matrix-transfer method,

the normalised electric field transmission can be derived using a coupling matrix for each 3dB coupler in the MZI and a lossy transmission matrix for the phase shifter section.

$$\begin{bmatrix} E_o \\ E_2 \end{bmatrix} = \begin{bmatrix} a & b \\ b & a \end{bmatrix} \begin{bmatrix} c & 0 \\ 0 & d \end{bmatrix} \begin{bmatrix} a & b \\ b & a \end{bmatrix} \begin{bmatrix} E_i \\ E_1 \end{bmatrix} \quad (3.2)$$

$$= \begin{bmatrix} E_i (ca^2 + db^2) + E_1 (abc + abd) \\ E_i (abc + abd) + E_1 (da^2 + cb^2) \end{bmatrix} \quad (3.3)$$

Where E_i and E_o are the input and output fields respectively. The variables a , b , c and d are here merely placeholders for the expressions

$$a = \tau e^{-i\varphi} \quad (3.4)$$

$$b = \kappa e^{-i(\varphi + \frac{\pi}{2})} \quad (3.5)$$

$$c = A\gamma e^{-i\psi} \quad (3.6)$$

$$d = Ae^{-i\theta} \quad (3.7)$$

$$(3.8)$$

Which are also indicated on figure 3.7. A here is the transmission coefficient for the phase shifter region between the couplers. τ and κ are the transmission and coupling coefficients for the couplers which for lossless coupling relates as $\kappa^2 + \tau^2 = 1$. φ is the phase change associated with the couplers. ψ and θ are the phase change associated with the lower and upper arm of the MZI region respectively. This also includes phase modulation $\phi = \theta + \delta\psi$ where δ is phase modulation applied to the lower arm. The reason this model does not assume symmetric or anti-symmetric modulation is due to the limitations imposed by the available devices. Only PiN junctions in the SOI slab were available which causes push-pull operation to be inherently inefficient. All data presented later in this chapter was collected with forward bias on the lower arm in the MZI region. Injecting carriers also causes additional absorption in the phase shifters. This is represented in the model as γ . The ring section is included via the relation

$$E_1 = Be^{-i\phi} E_2 \quad (3.9)$$

Where B is the transmission coefficient for the ring section and ϕ the associated phase change. This leads to the following expression for the trans-

mission

$$\begin{aligned} \frac{I_o}{I_i} &= \left| \frac{E_o}{E_i} \right|^2 \\ &= \left| Ae^{-i2\varphi} \left(\gamma \tau^2 e^{-i\psi} - \kappa^2 e^{-i\theta} \right) - \frac{A^2 B \tau^2 \kappa^2 e^{-i(\phi+4\varphi)} \left(\gamma e^{-i\psi} + e^{-i\theta} \right)^2}{1 - AB e^{-i(\phi+2\varphi)} \left(\tau^2 e^{-i\theta} - \gamma \kappa^2 e^{-i\psi} \right)} \right|^2 \end{aligned} \quad (3.10)$$

The full reduction from (3.3) and (3.9) to (3.10) can be found in appendix A on page 101.

The first term in (3.10) describes the output in the absence of the ring i.e. $B = 0$ where light can take either of two paths through the MZI region represented by the two terms in the small bracket of the first term. The second term is the resonator term. The numerator contains the terms describing the non resonant roundtrip pathways i.e. describing the two overcoupled pathways. The terms in the denominator describes the two resonant pathways and sets the resonant condition

$$C = |C| e^{-i\Psi} = AB e^{-i(\phi+2\varphi)} \left(\tau^2 e^{-i\theta} - \gamma \kappa^2 e^{-i\psi} \right) \quad (3.11)$$

where resonances occur whenever $\Psi = 2n\pi$, ($n = 1, 2, 3, \dots$). From (3.3) it is seen that critical coupling occurs when the two terms reaches the same value and cancels out. This can be interpreted as whenever the circulating field of the second term cancels out the transmitted field from the first term. For even moderate Q resonators, the circulating field of a resonator can be many times higher than the transmitted field. Only a fraction of the circulating field is then needed in order to destructively interfere with the transmitted field. This stands in contrast to the conventional MZI modulator where the power is split 50/50 between the arms and the full fields of both arms have to be out of phase at the output in order cancel out. Furthermore it should be noted that the phase components θ and ψ , corresponding to the phase shift in the MZI arms, contribute to the accumulated phase shift twice as much as the intra-cavity phase shift ϕ . This means any phase modulation $\delta\psi$ or attenuation γ is twice as effective as intra-cavity modulation for this device.

It is clear that in order to take full advantage of the potentially low loss hybrid waveguide platform, the remaining losses must be kept down as well in order to increase the Q factor and through that reduce the modulation bias. Obviously this means using ring bend radii large enough to suppress

bending loss. Figure 3.7 has been depicted with straight sections and various changes in curvature along the resonant pathways. Each curvature represents a different set of optical modes. The modes in bend sections and straight sections may not differ much in terms of n_{eff} , but their electric field distributions are offset relative to each other which means transition between two sections of different curvature brings with it a loss penalty, albeit a small one, in the form of coupling loss. For high Q resonators these small contributions to the roundtrip loss of a resonator can be detrimental to the total Q of a resonator. Ideally the resonator is a perfect ring. A device with the same functionality as the one on figure 3.7 can be constructed with a ring as seen on figure 3.8, but one pays the price of imbalanced MZI arm lengths[101]. This can to some degree be compensated for by matching the phase shift contribution of the outer arm with half of the ring circumference. This does prove a bit impractical since the length differences between the two arms are significant so even slight variations in fabrication will undermine this phase matching condition. Figure 3.9 shows a transmission spectrum for this device type where a ring with a radius of $60\mu\text{m}$. The spectrum features a single critically coupled resonance around 1558nm with a Q_c of ~ 51000 . According to equation (3.13) on page 71 this Q corresponds to a propagation loss of $1.37\text{--}1.74\text{dB/cm}$ depending on the resonant pathway considered in the calculation i.e. the roundtrip length.

This device is described in detail elsewhere[100]. Devices of the type seen on figure 3.7 were fabricated at IME Astar on behalf of IBM and devices of the type seen on 3.8 were fabricated at the MRL cleanroom facilities at IBM during a research stay at T. J. Watson Research Center. These will hereafter be referred to as the IME and MRL lots respectively. The two lots represent different fabrication flows and architecture and although the SiN core has the same dimension in both lots, the gap and SOI layer thickness differ.

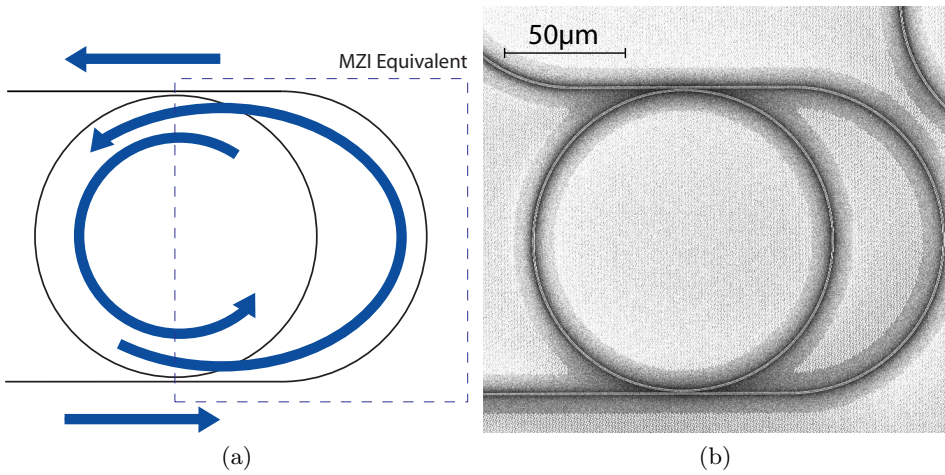


Figure 3.8: (a): Conceptual image of a ring resonator with a feedback waveguide on the right. The blue arrows indicate input, output and resonant pathways. Not shown are the two non-resonant pathways, characterised by a single pass through the device. The region enclosed by the dashed line is the equivalent of an imbalanced MZI in contrast to the balanced MZI in figure 3.7. (b): SEM image of a fabricated device featuring a $60\mu\text{m}$ ring.

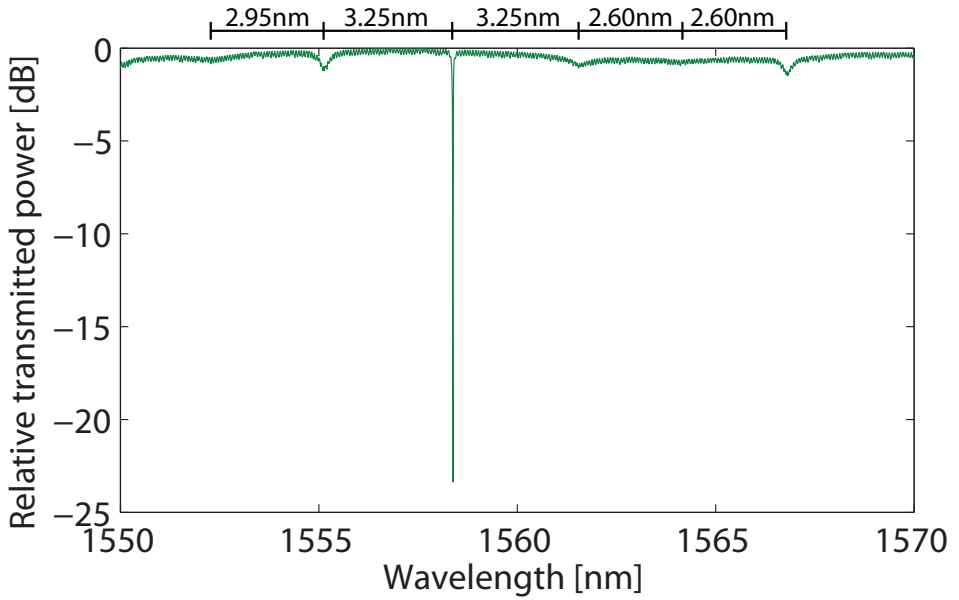


Figure 3.9: Transmission spectrum for the device shown on figure 3.8b with 100nm/100nm SOI slab/oxide gap thickness. The discrepancies in extinction ratios and FSR (indicated above the figure) is due to phase imbalance between the resonant pathways depicted on figure 3.8a. The resonance Q at critical coupling is here 51000 making the intrinsic Q 102000.

3.3 Hybrid phase shifter fabrication

First step in fabricating the hybrid waveguide is ion implantation of the SOI layer to create PN junctions for the phase shifters. Since PN junctions were not realised in this work I will not go further into implementation of these. However, the IME lot does feature a PiN region. For the IME lot the SOI layer was patterned so the hybrid waveguide structure only exists in the phase shifter region as can be seen on figure 3.12 on page 63 which allows for the transition loss between the SiN and hybrid waveguide sections to be estimated. For the MRL lot the SOI layer was not patterned and is present throughout the wafer. It should be noted that no wafers in this work were fabricated with SOI slab thickness less than 90nm which means significant propagation loss for TE operation according to the analysis in section 3.1. For this reason all design and characterisation was carried out for TM operation. TE operation might be favourable though as the TE mode tends to have SOI confinement factors 5-10 times higher than TM and expands applications to nonlinear optical signal processing where TE operation is required due to the stronger SiN confinement.

For the IME lot the gap is realised with PECVD of 230nm SiO_2 . For the MRL lot the gap is formed by thermal oxidation and etching of the SOI layer to form four splits of gap thickness and SOI slab thickness.

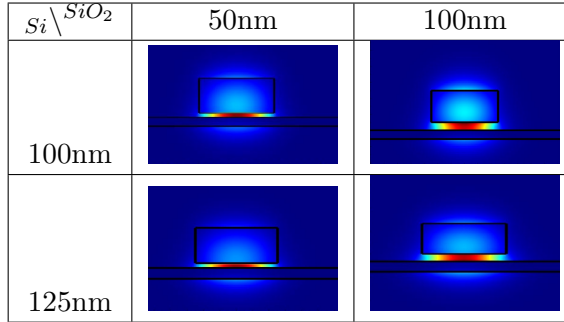


Table 3.1: Table showing TM mode profiles for the four splits in gap and slab thickness. Note the SiN core dimensions are the same in all four images. The difference in appearance is due to difference in axis scaling.

3.3.1 Silicon nitride deposition and stress compensation

Depending on deposition method, SiN will contain bound hydrogen in the form of Si-H and N-H bonds. These bonds cause optical absorption for wavelengths around 1520nm. The hydrogen content is much higher for plasma enhanced chemical vapour deposition (PECVD) nitride than it is for low pressure chemical vapour deposition (LPCVD). The hydrogen can however be degassed from the nitride with annealing, effectively removing the absorption peak around 1520nm[103]. In this work annealing was not attempted and as a result the additional absorption from the N-H bonds is seen in the propagation loss data on figure 3.13b and 3.15.

One of the main hurdles to overcome with SiN is growing a layer of significant thickness. Thick layers are required for high confinement waveguides as well as dispersion engineering. The SiN used in this work was deposited using LPCVD of ammonia (NH_3) and dichlorosilane (SiCl_2H_2) at 700°C. LPCVD SiN films deposited this way produces high tensile stress which fractures films thicker than $\sim 250\text{nm}$. For thicker films the tensile stress exceeds fracture str and the film cracks. Thick SiN films have been reported[104] where the film is fabricated through several cycles of deposition and thermal anneal to relieve stress. It is also possible to deposit a low stress version by increasing the dichlorosilane concentration in the LPCVD process[105]. It should be noted that this produces a silicon rich nitride with slightly different properties than stoichiometric SiN. In this work a 400nm SiN film was achieved through a series of processing steps depicted on figure 3.10. Here an initial 200nm LPCVD nitride was first deposited. Next, the 200nm backside nitride was removed by first depositing a PECVD oxide on the front followed by a wet backside strip in phosphoric acid. The removal of the backside SiN causes the wafer to bow and relieve stress from the front side SiN. This allows us to strip the front side oxide and grow an additional 200nm LPCVD nitride to a total of 400nm on the front and 200nm on the back. A downside with this process is the wafer will have a net positive bow before patterning from the 200nm difference in SiN thickness between front and backside. If the applied pattern is sufficiently dense, all stress on the front side will be relieved after etching and the bow will change sign since the backside 200nm SiN now dictates the bow. With this process flow the total bow never exceeds that induced by 200nm SiN even though there is 400nm SiN on the front side of the wafer. Had 400nm SiN been used for the backside not only would the film like have fractured, but the wafer would have succumbed to bow from the accumulated tensile stress of 400nm SiN as stress is completely relieved on the

front side during patterning. Large bow values pose a problem as certain complimentary metal-oxide-semiconductor (CMOS) processing equipment cant handle wafers with high bow values. For this reason SiN among other materials is often used for stress compensation. If wafer bow is a problem in the remaining processes the frontside can once again be applied a PECVD oxide and the backside stripped with phosphoric acid.

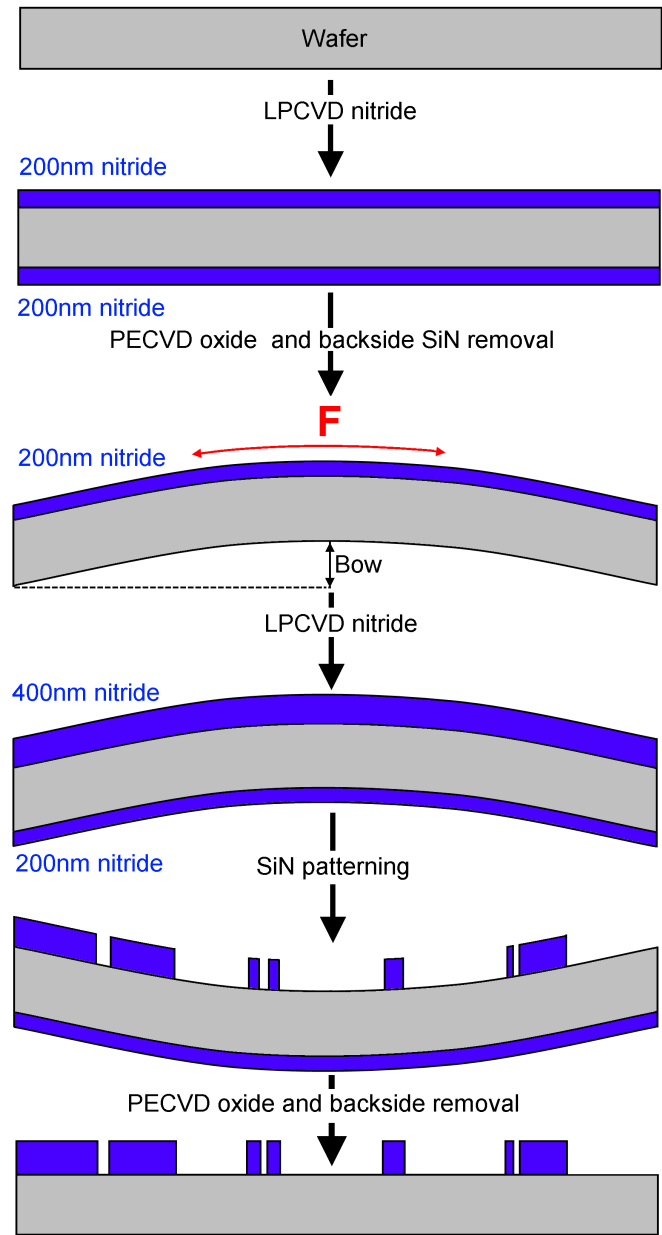


Figure 3.10: SiN deposition process steps taken to grow and pattern 400nm SiN on a 300mm wafer.

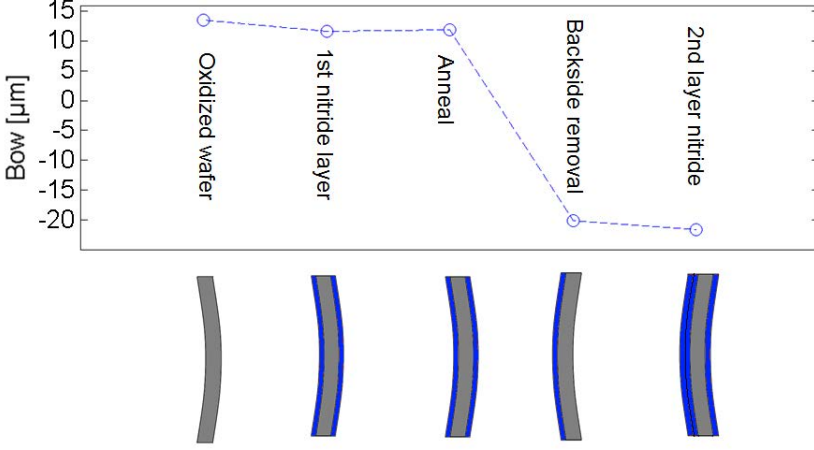


Figure 3.11: Measured wafer bow evolution for the deposition process described on figure 3.10. The initial oxidation and etch causes the wafers to have a net bow of $13\mu\text{m}$ before SiN deposition. As the backside is removed the bow changes by $\sim 34\mu\text{m}$ in negative direction resulting in a bow of $-21\mu\text{m}$.

3.4 Loss characterisation of hybrid waveguides

The propagation loss of the hybrid waveguide structure was characterised with paper clip structures of varying length on the MRL lot where the SOI slab extends the entire wafer. Light is coupled to the waveguides using adiabatic tapers, but unlike the IME lot, the facets are cleaved rather than etched. As can be seen on figure 3.14 and the inset in figure 3.18 the transmission spectra corresponding to the two fabrication splits with 100nm SOI slab are dominated by fast repeating features. It is furthermore noticed that the amplitude increases with waveguide length. Fringes due to reflections are normal however these have extinction ratios around 15dB at certain wavelengths for the devices with 100nm SOI slab and are almost absent for samples with 100nm SOI. This makes evaluating propagation loss rather difficult and calls for closer scrutiny. If it is reflection we are seeing the frequency of the dominant fringes will represent the FSR of the cavity or in this case the entire waveguide, facet to facet. The relation is similar to (3.1) and is given as

$$L = \frac{\lambda_0^2}{2n_g\Delta\lambda} \quad (3.12)$$

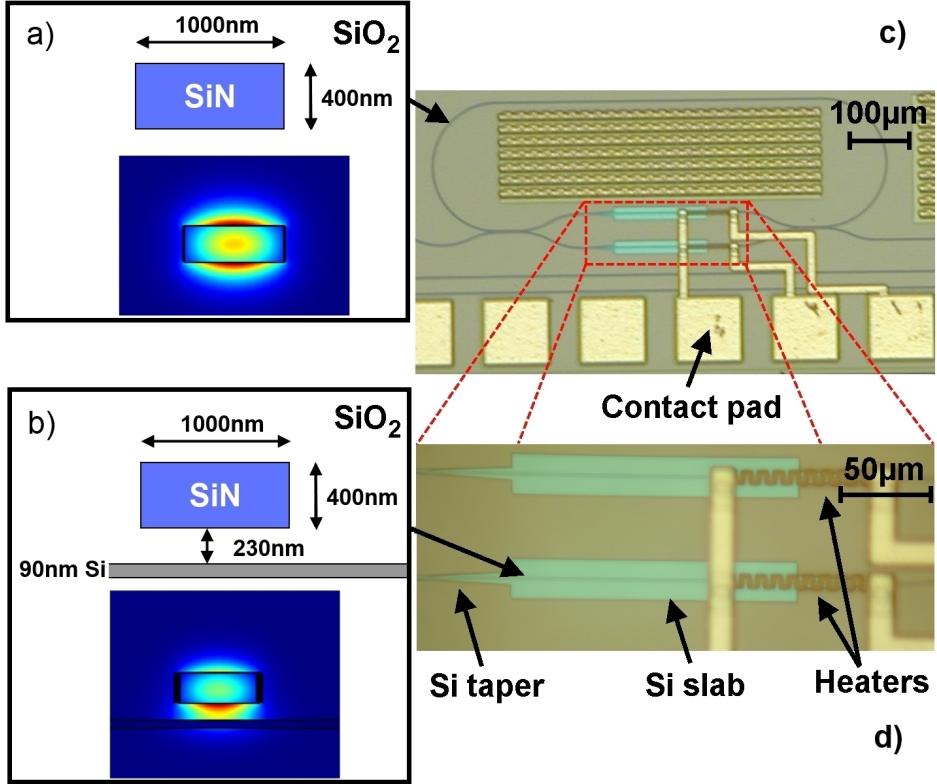


Figure 3.12: Cross sectional dimensions and mode profiles for the TM mode in a): the bus waveguide sections and b): the hybrid waveguide phase shifter. c): Top down photo of the coupling modulated ring resonator from the IME lot with heaters over the hybrid waveguide sections but without PiN doping and contacts to the SOI layer. b): Up close picture of the waveguide phase shifter region. The light is coupled between the SiN waveguide sections and the hybrid sections via adiabatic tapering of the SOI slab. This tapering is present on both left and right not visible below the heaters on the right.

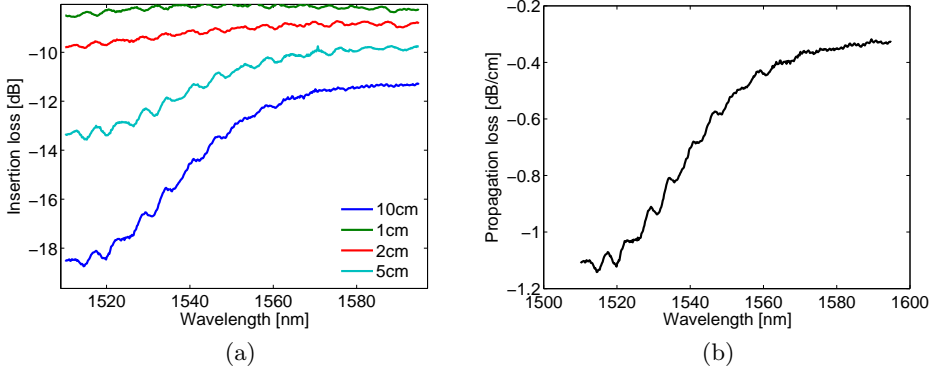


Figure 3.13: (a): Transmission spectra for various lengths of paper clip type designs for $400\text{nm} \times 1\mu\text{m}$ SiN waveguides fabricated at the IME Astar foundry. (b): The derived propagation loss showing increased loss near the N-H absorption band.

Where L is the cavity length, n_g the group index and $\Delta\lambda$ the FSR. The factor of 2 is due to the roundtrip being twice the length of the cavity, i.e. the length of the optical cavity is $2L$. As can be seen on the inset on figure 3.18 these oscillations cannot be described by a single frequency sinusoid. The FSR would therefore have to be extracted by fast Fourier transform (FFT) of the spectra. Figure 3.17 shows an example of FFT amplitude spectra for the $100\text{nm}/100\text{nm}$ plot on figure 3.14a. Notice the amplitudes are plotted against inverse metres. If the inverse of these frequencies are interpreted as waveguide cavity FSR, equation (3.12) allows us to extract the corresponding cavity length. For the two shortest waveguides on figure 3.17a and 3.17b there is a clear roll-off in the FFT plot corresponding to the accumulated lengths of the respective paper clips. The frequency components below these roll-off points correspond to shorter cavities. The continua of resonances that are seen for frequencies below the roll-off points could point towards reflective interfaces within the paperclips forming cavities with all combinations of the straight section lengths. Due to dispersion in n_g all resonance peaks broaden and overlap with neighbouring peaks causing the continua of states. The source of reflections appear to be in the bended sections and could be caused by mode mismatch between the straight section mode and bend section mode.

Unfortunately we can't just low-pass filter the transmission data on fig-

ure 3.14 with the inverse Fourier transform of the FFT data on figure 3.17. Since the mean value of the harmonics forming the base for the FFT is zero, low-pass filtering will produce a curve that follows the local mean value of the original data. This is problematic since the local mean depends on the extinction ratio of the reflection fringe which in turn depends on the reflection coefficient. In fact the values we are interested in are the local maxima which represents minimum reflection. The problem with reflections of varying extinction ratio is illustrated on figure 3.19. It is clear that the values needed for propagation loss characterisation forms an envelope of the data. Figure 3.18 shows the data from figure 3.14a where envelopes (black lines) to each spectrum is formed by the maximum for every 2nm wavelength. The propagation loss resulting from applying this method to the transmission data can be seen on figure 3.13b.

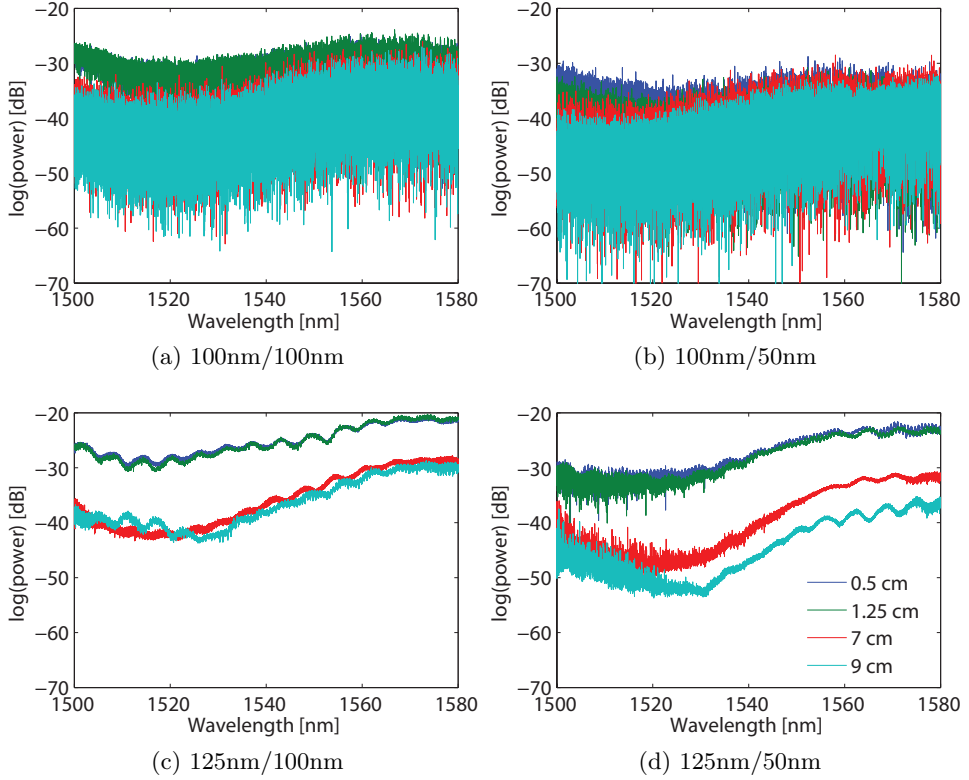


Figure 3.14: Transmission spectra for the SOI slab thickness / SiO₂ gaps shown in table 3.1 and indicated below each figure. The corresponding propagation loss can be seen on figure 3.15.:

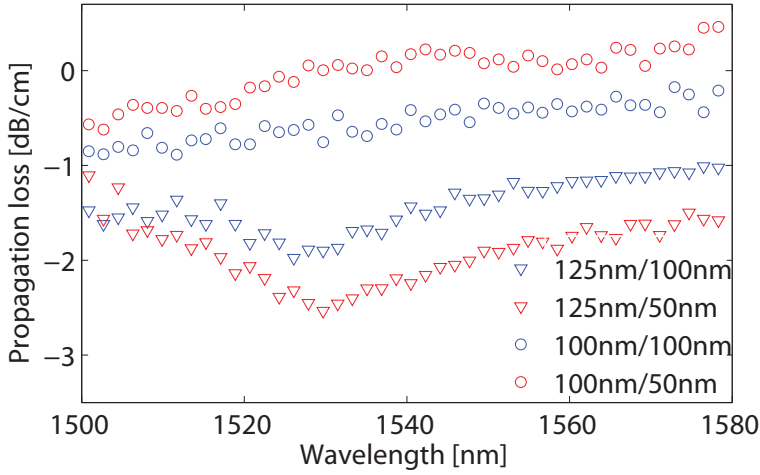


Figure 3.15: Propagation loss for the four (SOI thickness)/(oxide gap) splits shown in the legend. The N-H bond absorption band around 1530nm is observed for the tow splits with 125nm SOI slab thickness. The reason this feature is not seen for the splits with 100nm SOI slabs is like due to lower confinement to the the SiN core. It is also seen that propagation loss changes to positive values for the splits with 100nm SOI. This is not due to gain in the waveguide but rather shows the limitations of the method used to salvage propagation loss from low loss signals dominated by reflection etalons.

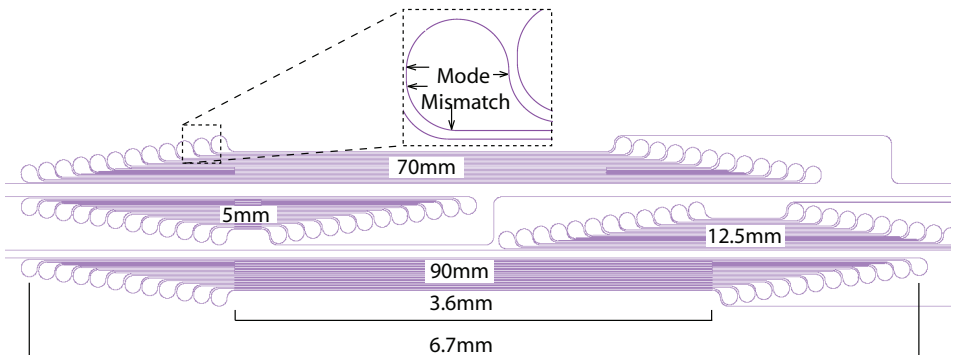


Figure 3.16: Layout of paper clip site used for cutback loss measurement. Total center section lengths from top to bottom are 70mm, 5mm, 12.5mm, 90mm.

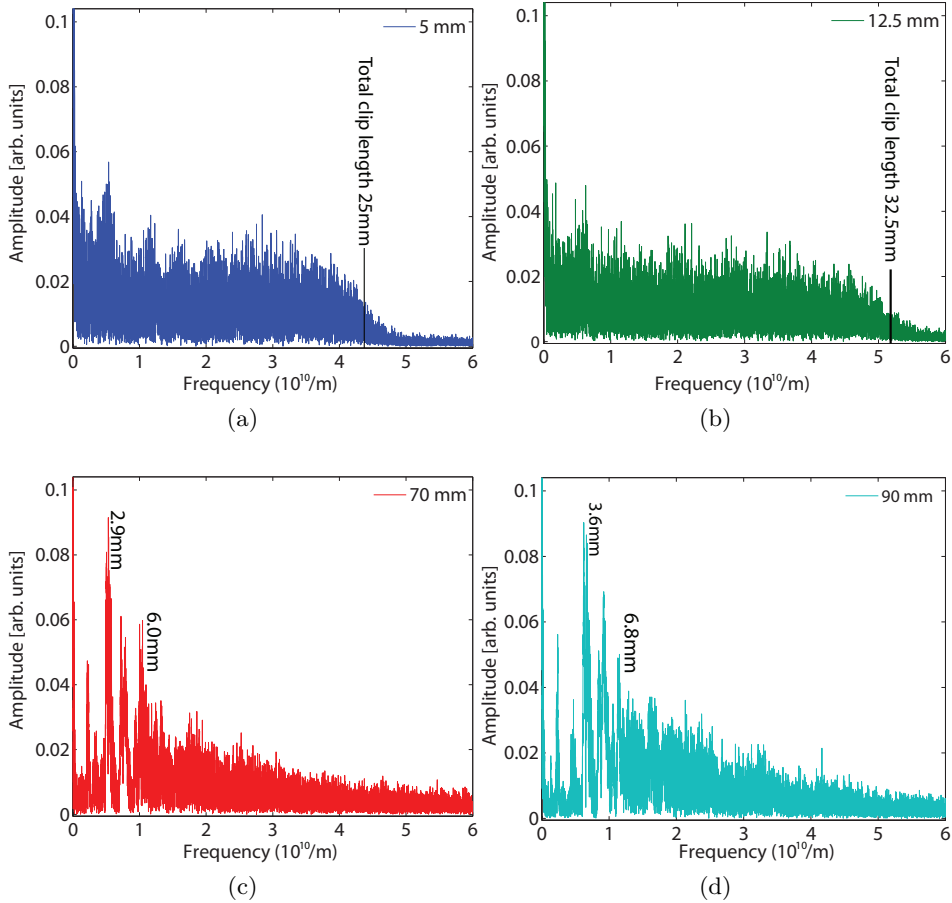


Figure 3.17: The four plots show the FFT spectra for the transmission plots on figure 3.14a. Using the relation (3.12), and the inverse frequencies as FSR, the FFT spectra can be associated to resonator lengths. For (a) and (b) the roll-off frequency is seen to correspond to the total clip length. For (c) and (d) any roll-off is smeared out over a wide frequency band. However strong resonances are seen at frequencies corresponding to the longest and shortest straight sections of the respective clips.

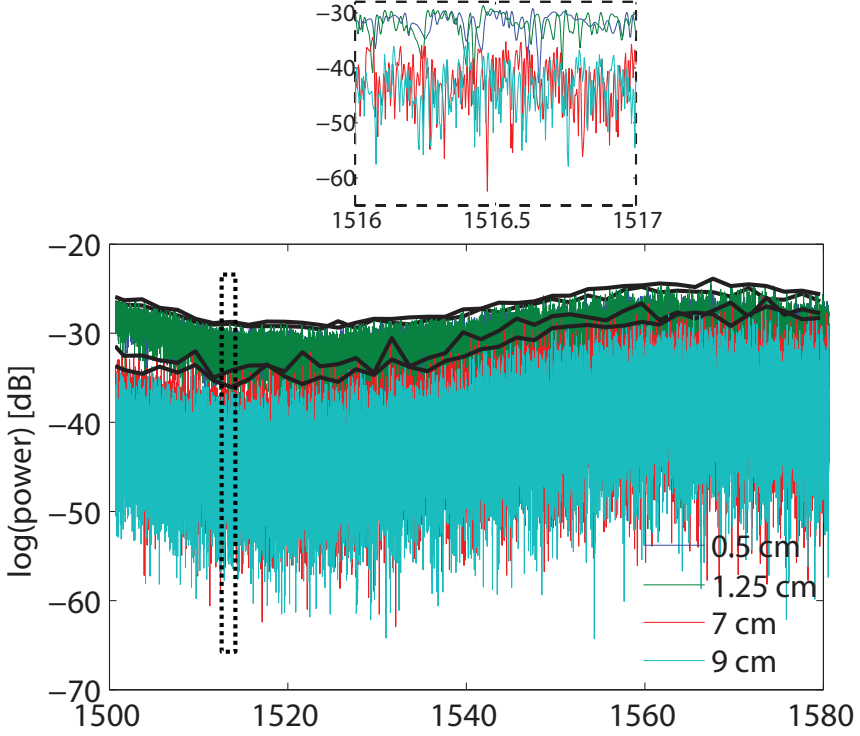


Figure 3.18: Envelope (black lines) method applied to the spectrums in figure 3.31. These envelopes form the basis of the propagation loss plot on figure 3.15. The inset shows a 1nm sample of the spectrum around 1516.5nm where the amplitudes of the fringes are small enough to distinguish spectra corresponding to the longer waveguides from the shorter ones.

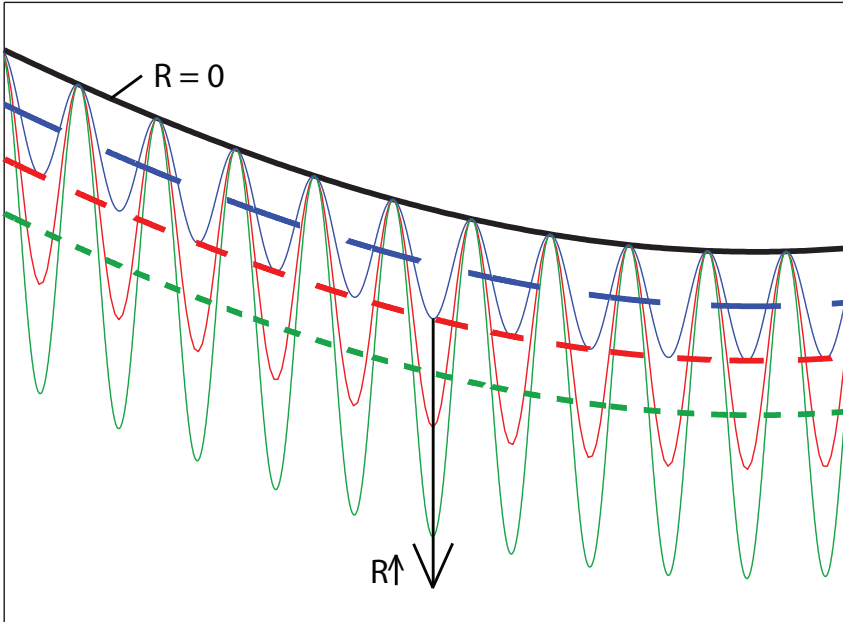


Figure 3.19: Illustration of the reflection data problem. The solid black line represents a transmission dataset in the absence of reflections ($R=0$). As reflection is introduced ($R>0$) the local mean curve of the data, here represented as dashed curves, is moved accordingly. If low pass filtering is performed on the datasets in colour the corresponding mean curves are obtained while the reflection-less envelope is formed by the local maxima.

3.4.1 Transition loss

In the case of the IME lot, the SOI slab is etched so it is only present where modulation is needed. In this design, light has to couple between a SiN waveguide and the hybrid waveguide modulator. The hybrid waveguide in the IME lot has 90nm/230nm (SOI slab/oxide gap). Simulated power coupling between the SiN waveguide and the hybrid waveguide for TM polarisation suggest a transition loss of 0.12dB/transition for abrupt transition. This value is already lower compared than the lowest achieved transition loss between a SiN waveguide and Si waveguide on a similar platform with tapering of both waveguides[95]. For use in high Q coupling modulated ring resonators this loss is still high compared to the roundtrip loss. Therefore the coupling is assisted by tapering of the SOI slab over a 50 μ m span as can be seen on figure 3.12d. The ideal way to measure the transition loss would be to cascade various numbers of transitions and extract the transition loss in a cutback fashion. Such structures are unfortunately not included in the design from IME, so the loss will have to be deduced in some other way.

Assuming loss-less coupling to a ring resonator, the quality factor $Q_{unloaded}$ for an isolated resonator relates to the roundtrip power loss α of the ring as [97]

$$Q_{unloaded} = \frac{\lambda_0}{\Delta\lambda} = \frac{\pi L n_g}{\lambda_0 \alpha} \quad (3.13)$$

Where L is the resonator roundtrip length and λ_0 is the resonance frequency and $\Delta\lambda$ is the full width at half maximum (FWHM) of the resonance etalon. Here $0 < \alpha < 1$, and it is seen smaller α leads to higher Q . Notice the use of n_g and not n_{eff} which is sometimes wrongfully used in even highly quoted papers [98, 106]. It is possibly an approximation from Fabry-Perot cavity theory where phase velocity and group velocity often doesn't differ significantly. For waveguides, as already discussed in section 1.7 on page 6, this assumption doesn't hold and $n_g \neq n_{eff}$ should generally be assumed.

In the following experiment the hybrid waveguide is placed in the resonator cavity as seen on figure 3.20, not the coupling region as we saw on figure 3.12. Knowing the propagation loss in the SiN bus waveguide from 3.13b we can deduce the loss contribution from the hybrid waveguide. Equation (3.13) then takes the form

$$Q_{unloaded} = \frac{\pi (L_{SiN} \cdot n_{g,SiN} + L_{hyb} \cdot n_{g,hyb})}{\lambda_0 (\alpha_{SiN} \cdot \alpha_{hyb})} \quad (3.14)$$

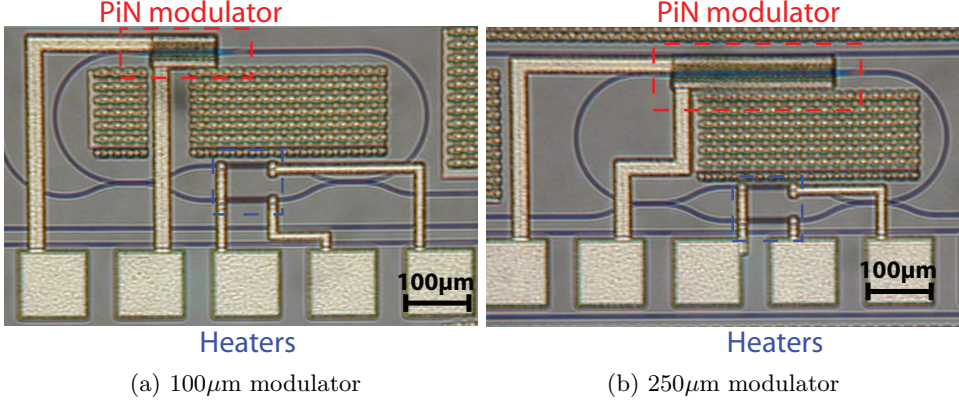


Figure 3.20: Coupling modulated racetrack ring resonators with heater control of the coupling modulation. The waveguides that make up the device is a SiN waveguide, however the intra cavity modulator, indicated with dashed red lines, is a hybrid waveguide with PiN junction in the SOI slab. Light is coupled to the (a): 100μm and (b): 250μm hybrid waveguide sections with 50μm long taper sections at each end.

Where $L_{SiN} \cdot n_{g,SiN}$ and $L_{hyb} \cdot n_{g,hyb}$ are the length times group index of the SiN and hybrid waveguide sections respectively. α_{SiN} and α_{hyb} are the power attenuation coefficients associated with the SiN and hybrid sections respectively. The power attenuation α_A and propagation loss a_A in units of dB/length for a given section A of length L_A relates as

$$\alpha_A = 10 \left(\frac{a_A L_A + 2a_t}{10} \right) \quad (3.15)$$

Where a_t is the transition loss per taper in dB. We already know the length of the sections from design, the n_g 's are deduced from the FSR of the transmission spectra and the propagation loss a_{SiN} from figure 3.13.

$Q_{unloaded}$ is not easily observed, but it relates to the quality factor at critical coupling Q_c as $Q_{unloaded} = 2Q_c$. The critical coupling condition is achieved with the heaters seen on figure 3.20 considering critical coupling when a resonance etalon with extinction ratio >20dB is achieved. In the calculations its assumed that the taper sections are part of the hybrid section and shares n_g with the hybrid section.

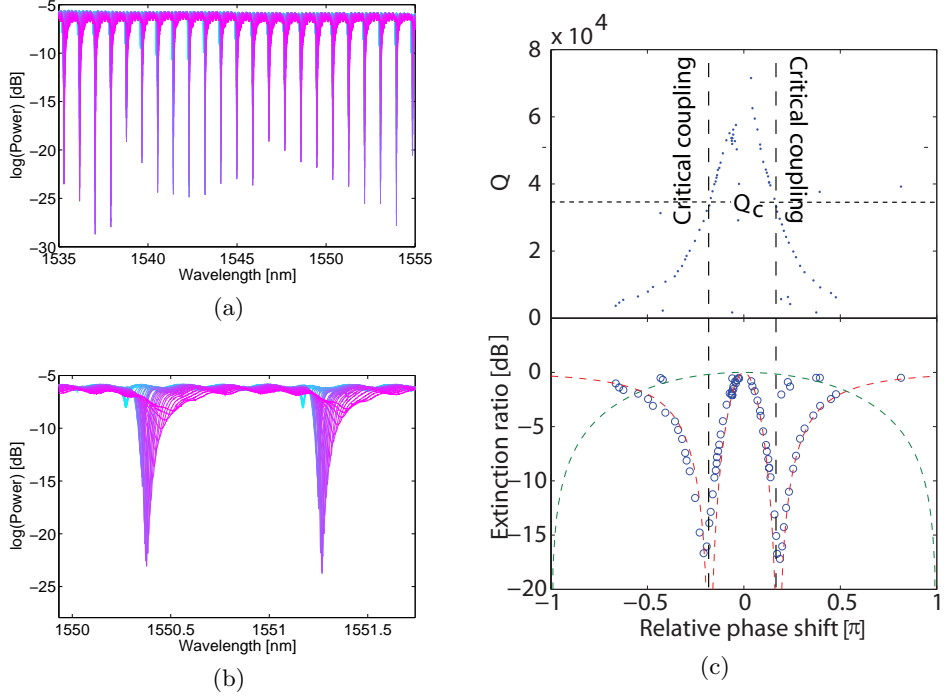


Figure 3.21: Transmission data for (a): Transmission spectra for the device on figure 3.21a for varying applied heater power to the lower MZI arm. (b): Close-up of the etalons near 1550nm showing a red-shift of the resonance wavelengths for increasing heater power. (c): Quality factor (top) and extinction ratio (bot) versus heater induced phase shift relative to undercoupled/unloaded Q. Negative phase implies phase shift induced in the upper MZI arm. Red dashed line represent a fit using the model (3.10) assuming no loss in the coupling region The green dashed line is a simple MZI model for reference. The vertical dashed black lines indicate the critical coupling point. Between the two critical coupling points the the resonator is considered undercoupled. Outside the undercoupled region the resonator is considered undercoupled.

The dispersion in extinction ratio on figure 3.21a for a given induced phase shift in the MZI section, is due to the accumulated dispersion in coupling coefficient κ , group index n_g , and loss A , B and γ in the expression (3.10) which all have wavelength dispersion.

Although the propagation loss data on figure 3.22 is too uncertain to

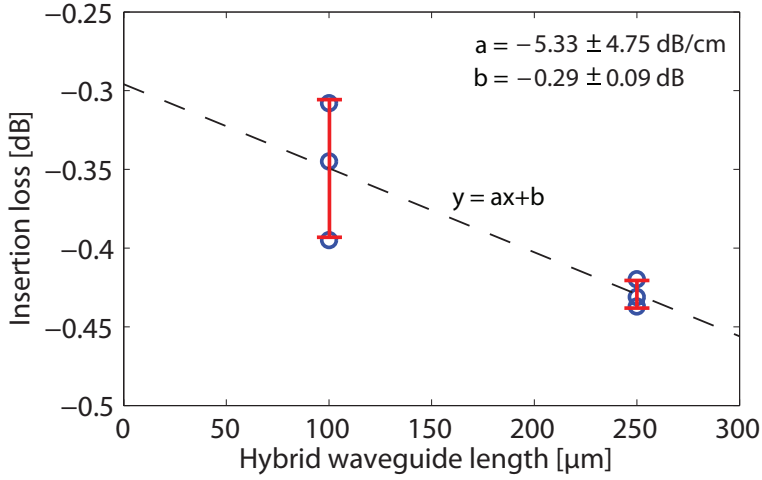


Figure 3.22: Insertion loss for the intra cavity hybrid waveguide section around 1550nm calculated from the quality factor of resonance resonances at critical coupling. Errorbars represent the standard deviation, the dashed line is a linear fit to the data with the coefficients a and b . a and b are given in the top right corner with 95% confidence intervals. Note that the transistion loss b is the loss contribution for both input and output combined.

draw any conclusions from, the transition loss $\left(\frac{1}{2}b\right)$ appear to land between 0.1dB and 0.2dB with some confidence. This is similar to the best reported transition loss between SiN and SOI waveguides[95] and coincides with the simulated power coupling loss of 0.12dB for an abrupt butt coupled transition. However this was not an abrupt transition and adiabatically coupling the light between the two sections should significantly reduce the transition loss. Unfortunately, devices with butt coupling between SiN and hybrid sections were not fabricated. There may be a couple of reasons the measured transition loss is higher than expected. Equation (3.13) assumes lossless coupling to the ring resonator. However, the MZI section that constitutes the coupling region has a span of $400\mu\text{m}$ and an associated insertion loss of $\sim 0.02\text{dB}$ which is somewhat low compared to the total roundtrip loss of $\sim 0.3\text{dB}$, why it was omitted in the first place. Another reason also related to the MZI region is the heater placement. The TiN heaters in the IME lot is situated only $1.5\mu\text{m}$ above the waveguide, which is close enough to cause scattering into surface plasmons significantly increasing loss. For this reason, the heaters in the MRL lot, are deposited on top of $3\mu\text{m}$ cladding oxide. This does reduce the effectiveness of the heaters as heat is distributed through a thicker oxide before heating the waveguide structure, but as long as they are able to produce enough phase shift for the switching requirements of these experiments without burning it, it is well worth it.

3.5 Thermo-optic modulation in hybrid waveguides

The following section describes the experimental demonstration of modulation in the hybrid waveguides of the IME lot, i.e. 90nm SOI and 230nm oxide gap. Tunability is achieved with TiN heaters, embedded in the cladding oxide. The device used for this experiment can be seen on figure 3.12 on page 63

Introduction

As a high index contrast waveguide platform, silicon nitride (SiN) has the advantage of significantly lower optical propagation loss than silicon on insulator (SOI) waveguides, over a wide range of wavelengths from the visible spectrum into the infrared. Although progress has been made in terms of reducing propagation loss on the SOI platform [107], it is still often large

in comparison to SiN. With a refractive index near 2 at telecommunication wavelengths, SiN is an excellent material for compact passive components ranging from delay lines [108] to arrayed waveguide gratings[109]. Within the fields of nonlinear optics and all-optical signal processing, the low nonlinear absorption and propagation loss of SiN have been key factors in the development of high-performance four-wave mixing-based devices, including nonlinear wavelength converters [110] and frequency comb generators [21]. However, in contrast to SOI waveguides, SiN waveguides are not directly amenable to high-speed electrooptic modulation, for example by integration of a PN diode free-carrier phase-shifter.

Here, we propose a hybrid SiN/Si waveguide design in which the SiN-confined optical mode evanescently couples to an underlying thin SOI slab, as shown on figure 3.12 on page 63. The optical mode of this hybrid waveguide can remain largely confined within the SiN core, to maintain the low-loss characteristics of the SiN platform. At the same time, a PN junction embedded within the thin SOI slab can be used to evanescently modulate the mode's phase, without the need for potentially lossy complete modal transfer from the SiN waveguide to a high-confinement SOI phase-shifter [96]. While we do not yet demonstrate PN diode electrooptic modulation functionality here on account of fabrication process flow limitations, we are able to characterize the hybrid phase-shifter using a representative thermooptically actuated resonator system.

Design

A cross section of the demonstrated hybrid SiN/Si phase-shifter is shown on 3.12a. A 400nm by $1\mu\text{m}$ LPCVD SiN waveguide constitutes the primary planar waveguide core structure. This waveguide is evanescently coupled to a 90nm-thick SOI slab located below the SiN waveguide, separated by a 230nm-thick silicon dioxide (SiO_2) spacer layer. A $2\mu\text{m}$ -thick buried oxide layer is present between the SOI slab and the Si handle wafer. Figure 1a) also illustrates the E_y field of the TM-polarized mode ($\lambda=1550\text{nm}$) supported in the hybrid SiN/Si waveguide, in which this phase-shifter is designed to operate.

In order to evaluate the characteristics of this phase-shifter, we utilize a racetrack resonator device with a Mach-Zehnder interferometer (MZI) as tunable directional coupler, as shown on figure 3.12c. The principle of operation of this configuration is detailed elsewhere [106]. The racetrack uses conservative $100\mu\text{m}$ radius bends, and has a $510\mu\text{m}$ straight section. Optical coupling into the racetrack is controlled via the MZI, comprised

of two TM-mode 3 dB directional couplers, and 145 μ m-long hybrid SiN/Si waveguide phase-shifter sections. The mode mismatch between the fundamental TM mode of an isolated SiN waveguide (figure 3.12b) and the TM mode in the SiN/Si phase shifter will induce loss when coupling between the two waveguide regions. To reduce this loss, 50 μ m-long mode transformation tapers are introduced within the Si slab layer as seen in 3.23a 1d). Finally, titanium nitride resistive heaters are fabricated over top of the hybrid SiN/Si regions as thermo-optic phase shifters (figure 3.12d). These are connected to contact pads with aluminum vias and interconnect wiring. The devices shown on figure 3.12 were fabricated using the IME-A*STAR silicon photonics process.

Experiment

Figure 3.23a shows collected racetrack spectral transmission data for a resonator fringe near $\lambda=1545\text{nm}$, for various levels of coupling, as controlled via the thermo-optically tunable MZI coupler. Complete resonator tuning through under, critical, and over coupling characteristics is achieved. Figure 3.23b plots the on-resonance transmission as a function of the thermo-optically generated MZI relative phase shift, as well as the resulting tunable coupler transmission coefficient $|t|$. At critical coupling $|t|$ equals the roundtrip racetrack transmission coefficient α , which is found to be 0.96 by fitting to the simplified model outlined in [106]. Quality factor Q values are obtained by fitting the racetrack resonance fringes as a function of MZI relative phase shift as shown in figure 3.23c, demonstrating $Q = 37,000$ at critical coupling and an intrinsic Q_i of approximately 74,000.

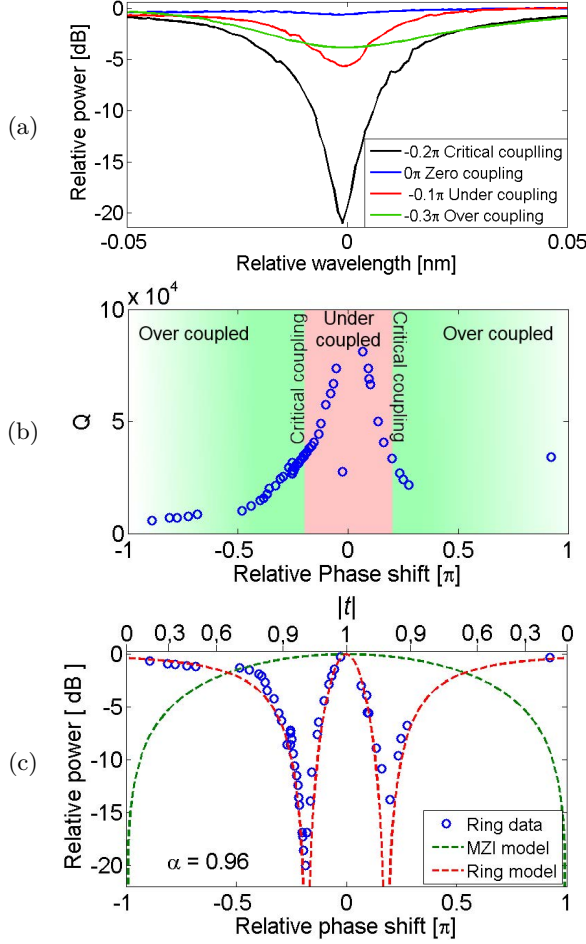


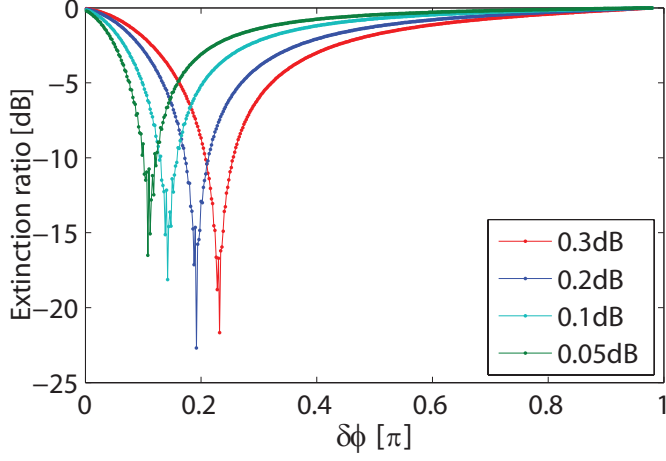
Figure 3.23: a): Sample transmission spectra showing a sequence of racetrack resonator fringes near $\lambda=1545\text{nm}$, at various degrees of coupling. b) Extinction ratio as a function of the induced phase shift within the MZI tunable coupler. Here, zero relative phase shift corresponds to zero coupling to the racetrack. The top axis plots the transmission factor $|t|$ for the MZI tunable coupler. At critical coupling where the transmitted power drops by 20dB $|t| = \alpha = 0.96$. The thermo-optic heaters used for MZI tuning dissipate 345mW electrical power to generate a π relative phase shift, which could be significantly reduced if the heaters were embedded directly within the thin SOI slab. c) Measured resonator quality factor Q values plotted against the relative phase shift. The intrinsic $Q_i = 74,000$ around 0π corresponds to twice the Q at critical coupling.

Assuming the propagation loss in the SiN waveguide sections follow the trend on figure 3.13 on page 64, the model in equation (3.10) can be used to estimate the impact of the insertion loss A of the MZI region of the resonator device. With a SiN waveguide propagation loss of ~ 0.8 dB/cm around 1545nm wavelength and a resonator length of $981\mu\text{m}$, the ring transmission parameter $B = 0.991$ which corresponds to 0.04dB of insertion loss through the ring section. The loss contribution of the ring resonator could be lowered by moving to a longer wavelength as seen on figure 3.13. At a wavelength of 1560nm the propagation loss approaches 0.3dB/cm which would make the transmission parameter $B = 0.993$ or 0.03dB of insertion loss. This improvement doesn't change the phase shift required for full extinction by any significant amount compared to and improvement in the transmission coefficient A for two reasons. First, as discussed in section 3.2 the parameter A factors twice into equation (3.10) and second, the loss contribution of the ring to the total roundtrip loss is dwarfed by that of the insertion loss of the hybrid waveguide phase shifter. Fitting to the data in figure 3.23 suggests a phase shifter transmission factor $A = 0.933B$. which translates to an insertion loss of 0.18dB This includes the short sections of SiN waveguide between the 3dB couplers and the hybrid waveguide sections as seen on figure 3.27b on page 86. Even though this value includes the loss of the entire phase shifter section it is lower than the SiN to hybrid waveguide transition loss estimated with the method in section 3.4.1 which coincidentally is lower than the lowest reported SiN to SOI waveguide transition loss [95].

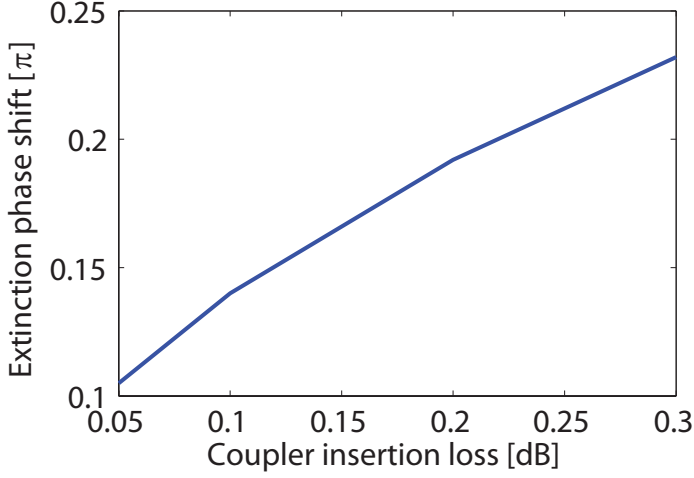
Figure 3.24 shows the impact a reduction in phase shifter insertion loss would have on the phase shift required for full extinction and hence the voltage required for switching. The results are produced assuming 0.8dB/cm propagation loss in the ring section and modulation exclusively from phase shift in the lower arm i.e. $\gamma = 1$. As can be seen on figure 3.24b a reduction from 0.18dB in phase shifter insertion loss to just 0.10dB would mean a decrease in the phase shift required for modulation by $\sim 25\%$. It is clear that evaluating the performance of this type of device the typical figure of merit $V_\pi L \alpha$ for conventional waveguide modulators does not capture the mechanisms that govern the performance of a coupling modulated ring resonator. First the parameter v_π should be replaced by the voltage V_{ext} required to produce a full swing from on to off state. The power dissipated in the phase-shifter still depends on the length so that should remain included. As we have seen, the propagation loss α

matters little compared to the transition loss between the SiN and hybrid waveguide. It is of course possible to avoid the transition loss altogether as with the devices presented in section 3.1 where the slab spans the entire wafer. Additionally, there is no trade-off between loss and $V_{ext}L$ unlike the isolated since loss directly affects V_{ext} as seen on figure 3.24b and is thus already included. It therefore makes sense to define the figure of merit as simply $V_{ext}L$.

Unfortunately, as already mentioned the thermo-optic effect (TOE) dominates the static characterisation making assesment of V_{ext} challenging. However, a V_{pp} of 0.9V in is used to dynamically switch the signal in section 3.6 on page 82 which would mean $V_{ext}L = 0.009V \cdot cm$ for the $100\mu m$ over which voltage is applied. This value will of course increase significantly for high speed modulation.



(a)



(b)

Figure 3.24: (a): Simulated extinction ratio vs lower arm phase shift modulation $\delta\phi$ for various values of phase shifter insertion loss. (b): The phase shift required for full extinction extracted from (a) versus phase shifter total insertion loss.

Summary

We have proposed an alternative approach for enabling active modulation of optical signals in SiN waveguides, using an evanescently coupled thin SOI slab. We characterize a thermo-optically tuned version of the hybrid SiN/Si structure using a racetrack resonator system. These results suggest that use of a PN diode electrooptic phase-shifter within the SOI slab can be a promising route to high-speed modulation of optical signals within the low-loss SiN waveguide platform.

3.6 Forward bias operation

The switching bandwidth of the coupling modulated ring resonator is dictated by the bandwidth of the PiN diode in the SOI layer. Modulation is achieved via a combination of electro-absorption $\Delta\alpha$ and index dispersion Δn due to free charge carriers [11].

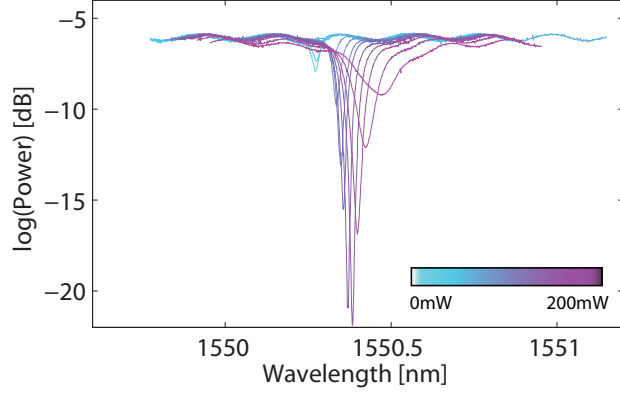
$$\Delta n = -\frac{e^2\lambda^2}{8\pi^2c^2\epsilon_0n}\left(\frac{\Delta N_e}{m_e} + \frac{\Delta N_h}{m_h}\right) \quad (3.16)$$

$$\Delta\alpha = \frac{e^3\lambda^2}{4\pi^2c^3\epsilon_0n}\left(\frac{\Delta N_e}{m_e}\mu_e + \frac{\Delta N_h}{m_h^2}\mu_h\right) \quad (3.17)$$

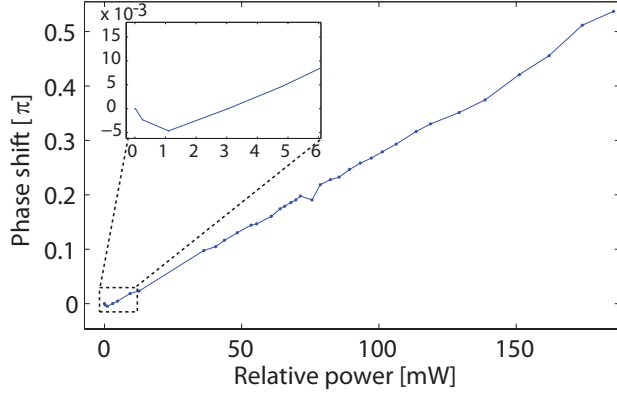
where e is the electronic charge, ϵ_0 is the permittivity of free space, n is the refractive index of intrinsic silicon, m_e and m_h are the effective mass of electrons and holes respectively and ΔN_e and ΔN_h are charge carrier concentrations of electrons and holes respectively. Finally, μ_e and μ_h are the electron and hole mobilities. Note that a positive change in charge carrier concentration leads to a negative change in refractive index. This stands in contrast to the TOE [111] where an increase in temperature leads to a positive change in refractive index for the materials considered here. The TOE is relevant as the PiN diode will heat during operation as any resistive medium when a current runs through it. Unlike electro-optic effect (EOE) which is restricted to the light confined to the SOI slab where charge carriers are present, the TOE accumulates contributions to a change in refractive index from both heated oxide and SiN where the majority of light is confined to. For static characterisation the EOE adds to the TOE. Since they act in opposite directions a static characterisation will only reveal which of the effects is stronger at a given electric current. It should here be noted that the EOE is proportional to the current density which is proportional to the total current I through the slab whereas the TOE is

3.6 Forward bias operation

proportional to the temperature which relates to the electrical power and thus the current squared I^2 . As can be seen on figure 3.25b the wl shift and thus the refractive index change is positive and varies linearly with power. The produced change in refractive index from the TOE is the



(a)



(b)

Figure 3.25: (a): Spectral samples for a single resonance etalon around 1550nm as current is dissipated through the PiN junction of the lower phase shifter arm on figure 3.27b in forward bias. (b): Phase shift versus dissipated electrical power. The positive phase shift corresponds to a red shift in resonance etalon in (a). The inset shows a close-up of the low power regime where the EOE dominates TOE.

accumulated contribution from the entire heated structure. Additionally, the thermo-optic coefficients for all materials involved in this structure are

positive which counteracts the EOE in (3.17). For static characterisation of these components where the confinement factor for the SOI slab is low, the EOE is dominated by the TOE as seen on figure 3.25 where only a weak blueshift from EOE is seen before the data is dominated by redshift of the resonance as current is injected. When operated in reverse bias, electrons are removed from the intrinsic region increasing the refractive index according to equation(3.17). However operation of the device on figure 3.27b in reverse bias mode didn't yield an observable phase shift. This is expected since the device is a PiN type diode with moderate doping (built in potential 1.1V) and wide intrinsic region ($\sim 4\mu\text{m}$). This leads to a low charge density ρ in the intrinsic region according to Poissons relation

$$\nabla^2\phi = -\nabla \cdot D = -\frac{\rho}{\epsilon\epsilon_0} \quad (3.18)$$

where D is the electric displacement, ϵ the relative permittivity of silicon and ϕ the electric potential across the region. For reverse bias operation to have an effect there has to be carriers to extract. According to equation (3.18) this is done by increasing the electric displacement field gradient by reducing the intrinsic region width or increasing the built-in potential. In order to see the effect of charge density modulation we are therefore restricted to slower forward bias operation for this device. Although the initial blueshift on figure 3.25a is predicted, it is sufficiently shallow that it is uncertain whether higher current injection rates will be able to produce enough of a phase shift to effectively modulate light at high speed. Fortunately the TOE depends on cooling and heating rates which are slow compared to the responsivity of electrons and as a result will have a lower bandwidth than the electric response. We can therefore distinguish the two effects in the temporal domain. The modulation bandwidth of the device is deduced from the frequency response of the modulator when driven in a 50Ω system using a network analyser. Figure 3.26 shows the optical response corresponding to the S_{21} parameter as a function of harmonic frequency for the device driven in forward bias mode for two different modulator lengths. The 3dB bandwidth is seen to be 380MHz in both cases. This is too low for any highspeed modulation experiment. Even with aggressive high-pass filtering a factor of 10 in bandwidth might be obtainable, but this will still only mean a few GHz of modulation speed. However, a bandwidth of 380MHz does suggest a modulation mechanism much faster than what would be expected from thermal modulation.

To asses the different time constants between the thermal and electronic modulation, the modulator was driven with slow 502ns square pulses with

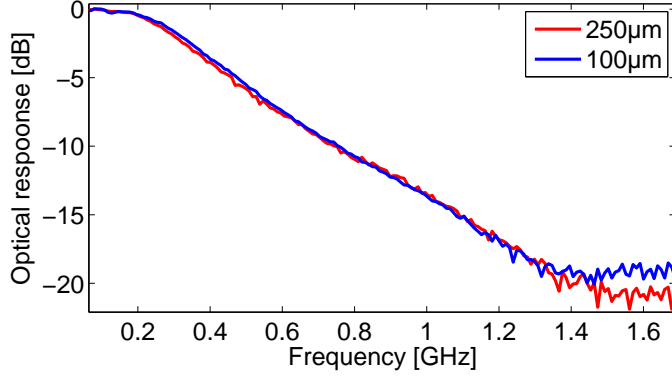


Figure 3.26: Measured $|S_{21}|$ parameter for two phase shifter lengths. Similar frequency response is observed regardless of phaseshifter length.

50% duty cycle in forward bias with a peak-to-peak voltage of $0.1V_{pp}$ around a voltage offset of 1.0V. The resulting waveform is seen on figure 3.27a. It is clear that two time constants are in play. The fast rise and fall times of a few ns corresponds to expected electronic speeds while the much slower rise and fall times of a few μs , which corresponds well with thermal modulation.

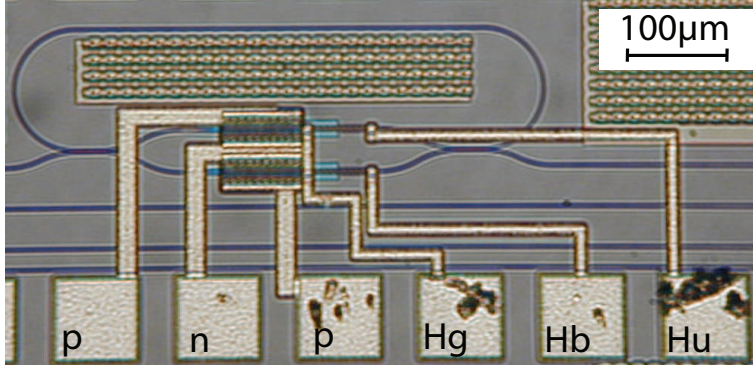
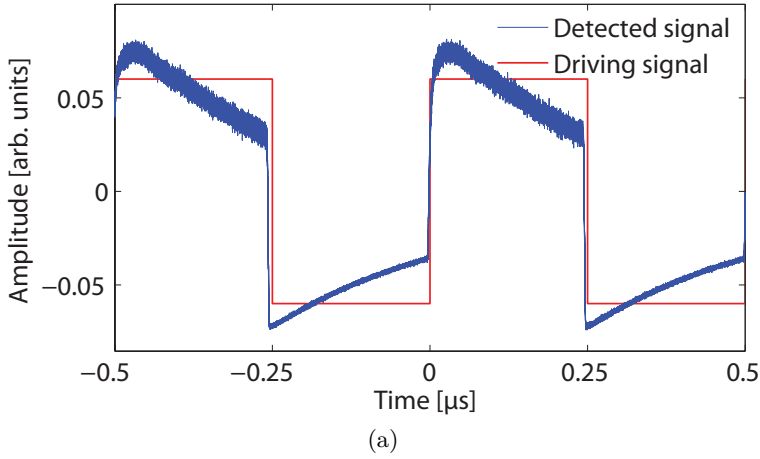


Figure 3.27: (a)(blue): Detected signal after modulation using the device shown in (a) where the PiN diode is driven in forward bias by (red): 502ns square pulse electrical driving signal with 50% duty cycle. The negative amplitude does not correspond to reverse bias. Only forward bias is used, the bias point of the electrical drive signal is offset with a bias tee. (b): Picture of the ring resonator device used in this experiment. The contact labels "p" and "n" indicate contacts for n and p doped regions respectively. "Hg" is the ground contact for the heaters, while "Hb" and "Hu" are the contacts for the bottom and upper heater respectively. Dark spots on the contacts are scratches from contact with the electrical probing equipment.

Summary

It is thus shown that electronic modulation of the evanescent field in a silicon slab is possible. Significant extinction is achievable with a $100\mu\text{m}$

hybrid waveguide phase shifter when used in conjunction with a ring resonator even with less than 1% of the optical mode confined to the PiN region in the SOI slab according to figure 3.6 on page 51. The speed is thus largely dictated by the characteristics of the PiN junction. Shortening of the intrinsic region would help increase the carrier concentration in the intrinsic region and allow for fast reverse bias operation. Power efficiency depends on quality factor of the resonator and confinement factor of the active region, which can be increased in various ways as discussed in section 3.1 on page 44 or designed for TE mode which in general has 5-10 times the SOI slab confinement factor relative to TM polarisation for the same slab thickness.

3.7 Linear all-optical modulation in a hybrid waveguide

This section reports the demonstration of coupling modulation in a silicon nitride microring resonator of a continuous wave signal around 1550nm. Modulation is achieved through a optically induced phase shift in the underlying silicon slab of a hybrid waveguide, induced by a near infrared modulation signal at 808nm.

As already shown in this chapter, the hybrid waveguide configuration can be used to electrically modulate light via charge carrier density modulation. However, charge carriers can also be induced via direct absorption of light with photon energies above the bandgap energy. While the absorption of light around 1550nm in bulk silicon is almost absent, for light around 800nm the extinction coefficient $k=0.005$ [112] which corresponds to a bulk propagation loss of $0.33\text{dB}/\mu\text{m}$. The free charge carriers generated via absorption of 800nm light, is capable of modulating the light via the EOE similar to how it was done electrically earlier in this chapter.

In order to achieve this, a coupling modulated silicon nitride micro ring resonator (MRR) seen in the picture in figure 3.28b. The device is identical to the device used in 3.6, but without ion implantation or metallisation.

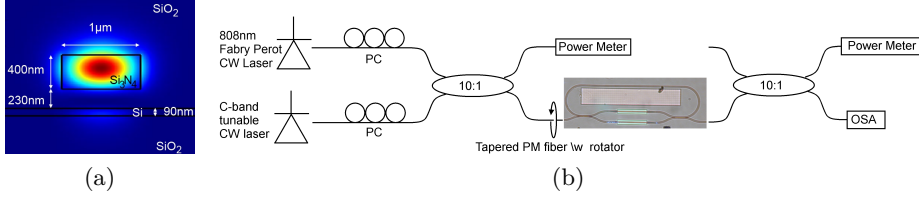


Figure 3.28: (a): TE mode profile and dimensions for the structure that make up the hybrid Si/Si₃N₄ phase shifters. The only difference between the phase shifter structure and the rest of the waveguide is the presence of the Si slab. (b): Experimental setup.

Experiment

Figure 3.28a shows the structures and TE mode profile at 1550 nm for the phase shifters. The only structural difference between the phase shifters and the waveguides in the rest of the optical circuit is the presence of the silicon slab. Light is coupled from the silicon nitride waveguide into the hybrid silicon/silicon nitride phase shifter via adiabatic tapering of the silicon slab.

The 3 dB couplers of the MZI equivalent are designed for wavelengths around 1550 nm and does not couple light efficiently between the waveguides at wavelengths in the 800 nm range. Since silicon nitride is transparent at wavelengths well below 800 nm and silicon effectively absorbs light at this wavelength, 800 nm light can be used to generate free carriers in the silicon slab in the "through" arm of the MZI leading to a phase shift due to the EOE and TOE. In terms of polarisation there is a couple of important points to be made. First, the 400 nm × 1 μm SiN waveguide is a multimode waveguide at 808 nm as seen on figure 3.29. This is partly responsible for the scattering loss we see on figure 3.31 and 3.32. However, the scattering allows us to probe the intensity of light with a camera as it propagates through the device. As can be seen on figure 3.31b 808 nm light passes through the "through" arm of the couplers designed to couple 3 dB for TM polarisation at 1550 nm. The light then enters the hybrid section through the tapered sections of the hybrid waveguide and is rapidly attenuated. At the end of the hybrid section only a bit of scattered light is seen from the termination of the slab and the tip of the slab taper. The rapid attenuation is most likely a combination of effective coupling from the SiN core to the Si slab mode due to the much higher effective index [113] ($n_{eff} = 2.66$) of the TE slab mode compared to the guided hybrid mode ($n_{eff} \approx 1.8$).

The high effective index of the slab mode is also an indication of high confinement to the slab which in turn means effective absorption. The extinction coefficient for silicon around 808nm is ~ 0.005 which in bulk corresponds to a propagation loss of $0.33\text{dB}/\mu\text{m}$. 50% or 3dB of a signal at 808nm is thus absorbed after just $9\mu\text{m}$, meaning light coupled into the slab is readily absorbed. However, the coupling to the slab is gradual and the confinement to the slab is not immediately 100% why residual light is still seen towards the end of the $150\mu\text{m}$ hybrid waveguide on figure 3.31b. On figure 3.32a the hybrid waveguide section is much longer ($550\mu\text{m}$) and little to no light scattering is seen from the last half for TE polarised light at 808nm wavelength.

For TM polarisation the story is slightly different. The TM slab mode has an effective index n_{eff} of 1.72, close to the effective index of the TM guided hybrid waveguide modes depicted on figure 3.30. Additionally, the TM slab mode confinement to the slab is rather low which means absorption is low. This difference in interaction with the hybrid waveguide and slab between the TE and TM polarisation can be seen on figure 3.32. For maximum effect, the experiment is carried out in TE polarisation. If the TOE would dominate the EOE, the polarisation of the 808nm signal could be tuned in order to distribute the absorption along the the phase shifter and hence distribute the heating as well.

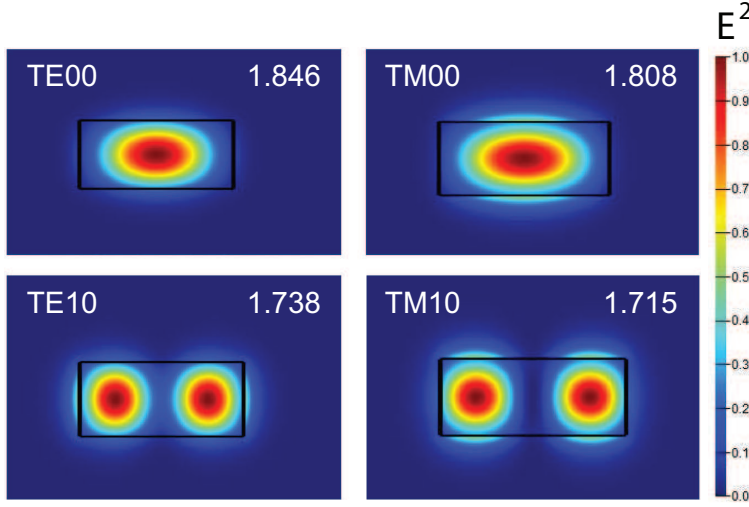


Figure 3.29: Calculated optical modes in a SiN waveguide at 808nm wavelength. It is seen that the waveguide supports multiple modes at each polarisation.

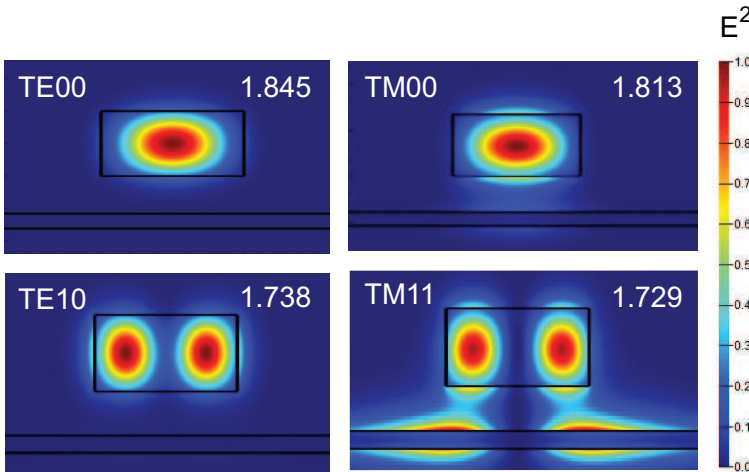
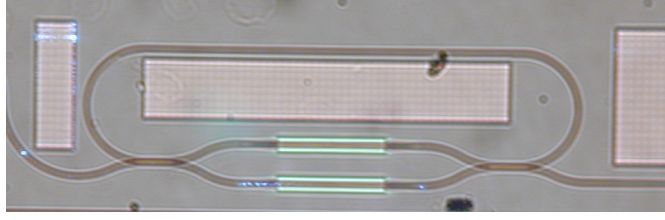


Figure 3.30: Simulated optical modes at 808nm in the hybrid waveguide. The number in the upper right corner of each figure corresponds to the respective n_{eff} . The corresponding n_{eff} 's of the slab are 2.66 and 1.72 for TE and TM polarisation respectively.



(a)



(b)

Figure 3.31: (a): Coupling modulated ring resonator during operation, illuminated and taken with visible light camera. Scattered blue light is the camera interpretation of the 808nm laser light. (b): Same device as (a), but without microscope illumination. The 808nm laser signal enters in the waveguide from the left and is clearly attenuated in the hybrid waveguide section of the lower arm.

Figure 3.28b shows the experimental setup used in this work. The outputs of a -4 dBm c-band cw tunable laser and a tunable 808nm wavelength fiber coupled Fabry-Perot laser is combined using a 10:1 fiber coupler designed for telecom wavelengths. At a wavelength of 808nm it applies only -1dB to the power through its cross port allowing us to multiplex the two outputs with only -1dB attenuation on both. The combined signal is then inserted into the nitride waveguide using a tapered polarisation maintaining fiber with a known polarisation output, mounted in a fiber rotating device. The output is analysed with an optical spectrum analyser.

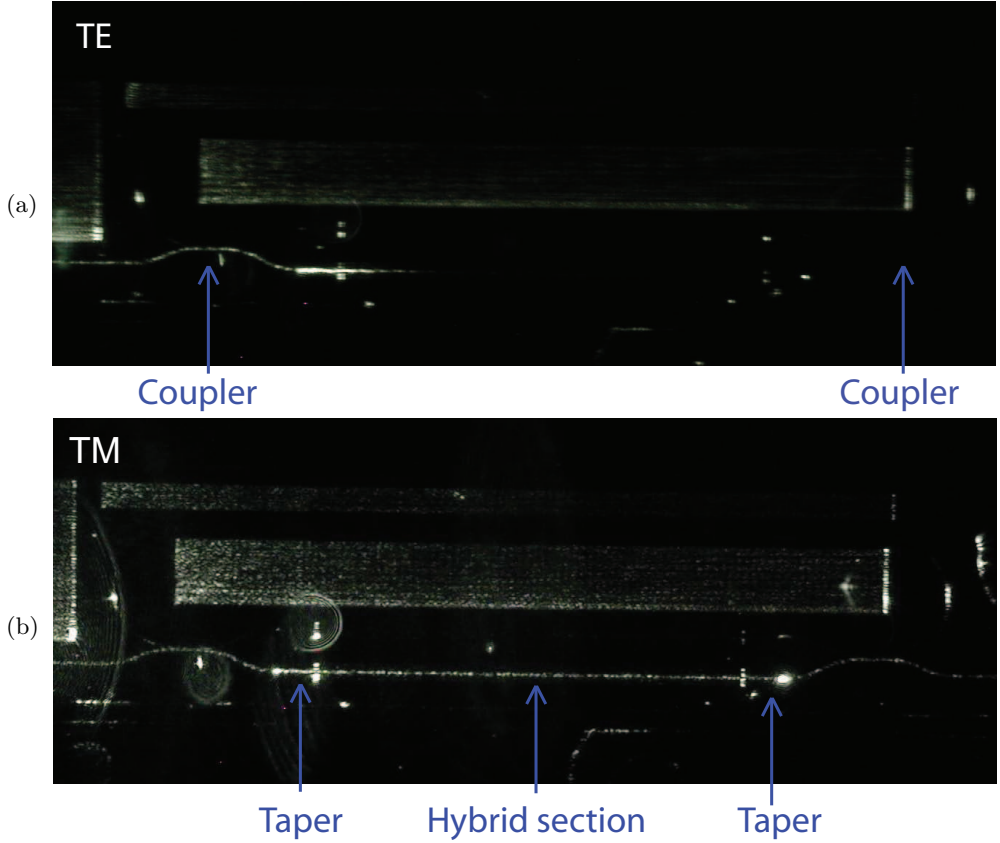


Figure 3.32: Comparison of scattering of an 808nm wavelength optical signal through a coupling modulated ring resonator as the one seen on figure 3.31a, albeit with a $550\mu\text{m}$ hybrid waveguide section. Light enters through the SiN waveguide from the left and as expected, TM polarised light in (b) passes through the hybrid waveguide with less attenuation than the TE signal in (a).

Modulation results

Figure 3.33 shows static transmission spectra and normalized transmission at resonance as a function of 808nm laser power measured before insertion into the chip. In figure 3.33a it is seen that a resonance goes from undercoupled to critical coupling between 5mW and 14mW demonstrating complete "on"/"off" functionality. The wavelength blue shift seen in 3.33b is due to a change in the resonator path length as a result of the phase modulation in the lower arm of the MZI seen in figure 3.28b. It can thus be concluded that the modulation is not due to simple heating, but charge carrier generation from light absorption.

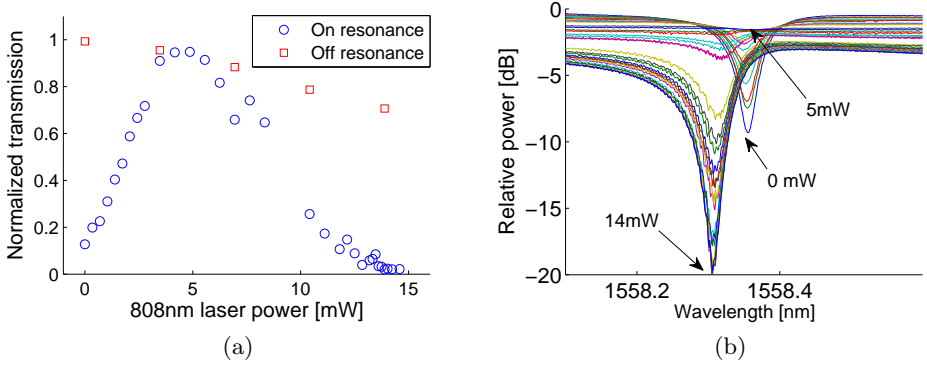


Figure 3.33: (a): Normalized transmission vs. 808 nm laser modulation power. Laser power is measured before being inserted into the chip. (b): Transmission spectra for various values of inserted modulation power. Both a wavelength shift due to the change in optical path length as modulation power is increased is seen along with resonance asymmetry with Fano resonances [114].

Summary

We have successfully demonstrated the modulation of a telecom CW signal in a silicon nitride waveguide using a hybrid silicon/silicon nitride phase shifter. Full "on"/"off" capabilities were demonstrated using a 5mW 808nm wavelength signal to induce an electro-optic phase shift in the silicon slab of the hybrid silicon/silicon nitride waveguide.

3.8 Summary

This chapter demonstrates a novel approach to optical signal modulation. A hybrid waveguide is described which consists of a SiN core waveguide underlined by an SOI slab separated by an oxide gap. Transition loss from a low loss SiN waveguide to this hybrid structure is shown to lie in the range 0.09dB to 0.15dB depending on the method used in the analysis. The transition can also be omitted completely by allowing the SOI slab to span the entire wafer possibly with a small penalty to propagation loss. This could not be explored with the fabricated devices as there were no two devices available with the same cross sectional structure but with and without SOI patterning. However, the structures tested here using the cutback method suggest the propagation loss remain somewhere between 0.4dB/cm and 2.0dB/cm depending on the SOI slab and oxide gap thickness at 1550nm which is still low compared to the best as-fabricated SOI waveguides.

400nm LPCVD nitride for the SiN core of the hybrid waveguides was realised on 300mm SOI wafers with the SOI slab and oxide gap layer already formed. 400nm LPCVD nitride without layer failure was achieved by depositing LPCVD nitride in two 200nm deposition steps with an intermittent backside removal to relieve stress from the front side layer.

The hybrid waveguide was tested as a phase modulator in a coupling modulated ring resonator. Restraints in fabrication meant that the PIN junction used for free carrier based modulation in the SOI slab was restricted to forward bias. Along with high series resistance this meant the potential for high bandwidth modulation could not be demonstrated with these devices. Instead the low voltage switching capabilities were demonstrated at low bandwidth. The voltage needed to switch between an on and off state for a coupling modulated resonator depends on the roundtrip loss of the ring resonator system. For high Q resonators the phase shift required in order to flip the switch is a small fraction of π . The device demonstrated here was able to efficiently modulate a signal at 1540nm wavelength by inducing only $0.18 \cdot \pi$ phase shift difference between the arms of the resonator embedded MZI.

Finally, all-optical linear modulation was demonstrated in a chip without ion implantation or metallisation, using a co-propagating 808nm laser signal as the modulation signal. Static on/off functionality was demonstrated with only 5mW of modulation laser power. Based on an observed blueshift in resonances, the dominant driving effect is attributed to an

electro-optic change in refractive index of the silicon slab as a result of free charge carriers, generated through absorption of 808nm light.

All devices in this chapter are designed for, and operated in TM polarisation at 1550nm. As is shown, the limiting factor for designing a similar device for TE polarisation is the the SOI slab thickness. For slab thickness's larger than $\sim 50\text{nm}$ the effective refractive index of the slab mode surpasses that of the hybrid mode resulting in effective energy transfer from the guided hybrid mode into the unguided slab mode from where light dissipate leading to significant loss of signal. Reducing the slab thickness also reduces the slab confinement factor which governs the modulation efficiency. However, the oxide gap separating the SiN core and the SOI slab has a similar effect and can be used to optimise the confinement factor as well. Although TE polarisation provides for more rigid design rules as it limits the SOI slab thickness, TE polarisation may be of more interest for a couple of reasons. According to simulations, the evanescent field penetrates the slab more efficiently leading to slab confinement factors 5-10 times higher than TM polarisation does for the same structure. This is due to the TM mode taking on the characteristics of a slot waveguide mode with the main part of its field in the oxide gap while the TE tend to occupy the large index structures such as the SiN core and the silicon slab. This is also the reason TE operation would be more viable for nonlinear optical signal processing schemes where confinement to the high index core is needed.

Chapter 4

Conclusion

Silicon photonics is slowly starting to realise its commercial potential after decades of research. Within the past few years the The work presented here explores the use of silicon as a waveguide material for ultra-fast all optical signal processing using the nonlinear Kerr effect in silicon. In order for the nonlinear effect to properly build over the span of a waveguide, the light intensity must be maintained through reduction of loss contributions. This thesis examines various treatments towards reducing the propagation loss resulting from line edge roughness on silicon waveguides fabricated from SOI wafers. The techniques here described include thermal reflow of photoresist, polymer aggregate dissociation using ultra-sound, semi isotropic plasma etch and shallow high temperature oxidation. For the standard rectangular waveguide with $300\text{nm} \times 450\text{nm}$ cross section, the loss was not significantly reduced below 2.0dB/cm with any of the approaches. Regardless of the inability to achieve lower loss, the 2.0dB/cm stil proved sufficient to demonstrate all optical signal regeneration of a 40Gb/s OTDM signal using cross-phase modulation and wavelength conversion of a 320Gb/s Nyquist OTDM signal using four wave mixing.

This Ph.D. thesis treats various aspects of silicon photonics. From the limitations of silicon as a linear and nonlinear waveguide medium to its synergy with alternative waveguide materials. Various methods for reducing sidewall roughness and line edge roughness of silicon waveguides are attempted. The methods include enhancements of etch mask roughness as well as etch isotropy and direct reduction of already present sidewall roughness. Although promising roughness assessments were made based on electron microscopy images, it did not translate into significantly lower propagation loss in fabricated silicon waveguides compared to waveguides

fabricated with a single step oxidation smoothing and a propagation loss of 2.0dB/cm around 1550nm wavelength. As an alternative to crystalline silicon waveguides for nonlinear optical applications, amorphous silicon was explored using RF sputtering potentially allowing for low density of detrimental hydrogen content in the final material. Unfortunately, the linear optical loss in the material was too high for any practical applications. It is speculated that the attempt at creating a material with low density of dangling bonds was unsuccessful.

Nevertheless, linear losses of 2.0dB/cm at 1550nm wavelength in the crystalline SOI waveguides remained sufficiently low that high speed nonlinear optical signal processing could be demonstrated. This includes four wave mixing based wavelength conversion of a 320Gb/s Nyquist OTDM signal and cross phase modulation based signal regeneration of a 40Gb/s OTDM signal.

Finally, a new type of low loss electrically driven optical modulator in silicon and silicon nitride is demonstrated. The device is an attempt to bridge the gap between the low loss platform of silicon nitride and the electrical capabilities of silicon on insulator. In this hybrid waveguide device, light is modulated via evanescent coupling from a nitride strip waveguide to a charge carrier based PIN modulator in a thin silicon slab. The device is demonstrated in conjunction with a coupling modulated ring resonator, a device which benefits from the low loss characteristics of this type of this hybrid waveguide phase shifter. The results of the characterisation demonstrates low propagation loss for the hybrid waveguide structure but higher than expected transition loss between a nitride strip waveguide and the hybrid structure even with adiabatic tapering of the slab. The quality factor of ring resonators where these hybrid waveguide sections are used for modulation are therefore dictated by the transition loss. Since propagation loss is generally below 2dB/cm for this structure higher Q could be achieved simply by composing the entire ring resonator device of the hybrid waveguide structure. One such device was tested with an intrinsic Q of 102000 at 1558nm.

The capabilities of the hybrid waveguide in conjunction with a ring resonator device as a modulator was tested with both electrical and optical modulation of charge carrier concentration in the SOI slab. As electrical modulation, the device was applied a 502ns square pulse signal in forward bias. The transmitted waveform revealed both a fast varying feature with a bandwidth around 300MHz attributed to carrier modulation and a slowly varying modulation attributed to the thermo-optic effect. Optical mod-

ulation was accomplished as a result of the wavelength dispersion of the coupling coefficients of the MZI equivalents in the coupling modulated ring resonator. This allowed for a high intensity signal to enter one arm of the MZI equivalent and excite charge carriers in the SOI slab the result of which was a blueshift in the resonance wavelength corresponding to a refractive index change as a result of charge carrier modulation. The charge carrier density modulation capabilities was thus described and demonstrated. What remains is, among other obstacles, to increase the electrical bandwidth of the slab PIN and the driving circuit which was not a main priority in this work.

Epilogue

Although the obstacles associated with silicon as a waveguide material remain, the platform is in a better shape than ever. The foundry services and commercial framework is coming together, forming the foundation for the second age of silicon in communication systems.

Silicon has persistently demonstrated its viability, not only for all optical signal processing, but as the waveguide material of choice for the handful of startups and established companies who has successfully commercialised integrated silicon photonic based products. It seems there is indeed a bright future ahead for silicon photonics. A question remains. With all the research being focused towards the field of photonics and silicon alternatives; How long will silicon reign supreme?

Appendix A

Transmission model derivation

The transmission model is derived using the scattering matrix approach. The variable dependencies are indicated on figure A.1. The device contains two resonant pathways given by the partial racetrack and the

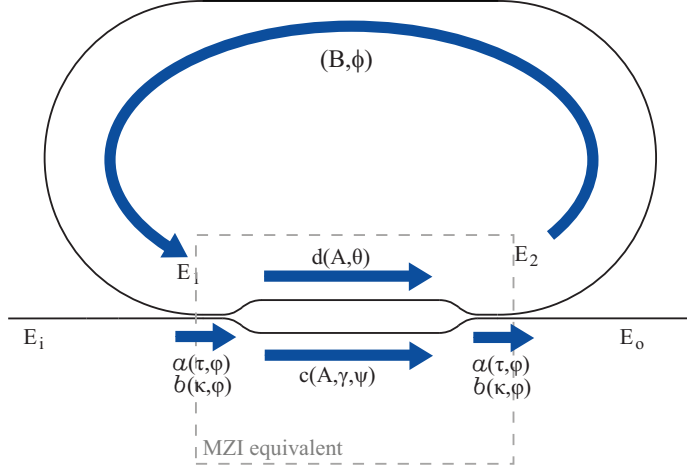


Figure A.1: Conceptual model of a coupling modulated ring resonator with a racetrack type resonator and MZI coupling modulator. Blue arrows indicate light pathways with their corresponding dependent variables and parameters.

$$\begin{bmatrix} E_o \\ E_2 \end{bmatrix} = \begin{bmatrix} a & b \\ b & a \end{bmatrix} \begin{bmatrix} c & 0 \\ 0 & d \end{bmatrix} \begin{bmatrix} a & b \\ b & a \end{bmatrix} \begin{bmatrix} E_i \\ E_1 \end{bmatrix} \quad (\text{A.1})$$

$$= \begin{bmatrix} E_i (ca^2 + db^2) + E_1 (abc + abd) \\ E_i (abc + abd) + E_1 (da^2 + cb^2) \end{bmatrix} \quad (\text{A.2})$$

$$a = \tau e^{-i\varphi} \quad (\text{A.3})$$

$$b = \kappa e^{-i(\varphi + \frac{\pi}{2})} \quad (\text{A.4})$$

$$c = A\gamma e^{-i\psi} \quad (\text{A.5})$$

$$d = Ae^{-i\theta} \quad (\text{A.6})$$

$$E_1 = Be^{-i\phi} E_2 \quad (\text{A.7})$$

Where τ and κ are the transmission and coupling coefficients respectively for the couplers.

A is the transmission coefficient associated with the MZI arms in the absence of modulation.

B is the transmission coefficient for the ring roundtrip from the directional coupler output port to its input port.

$\varphi = n_{eff1} L_C (2\pi/\lambda)$ is the phase shift associated with the length of the couplers.

$\theta = n_{eff2} L_{MZI} (2\pi/\lambda)$ is the phase shift of the MZI arms in the absence of modulation.

$\psi = \theta + \delta\psi$ is the phase shift of an MZI arm when modulation is present and $\delta\psi$ is the phase contribution from modulation. This model assumes modulation of the 'through' arm of the MZI only. $\delta\psi$ comes from a change in refractive index in this case from the thermo-optic effect in silicon that leads to a temperature and wavelength dependent change in n_{eff2} in the 'through' phase shifter.

γ is the transmission coefficient of an MZI arm in the presence of modulation.

$\phi = n_{eff1} L_R (2\pi/\lambda)$ is the phase change associated with the ring roundtrip.

$$E_o = E_i (ca^2 + db^2) + Be^{-i\phi} E_2 (abc + abd) \quad (\text{A.8})$$

$$E_2 = E_i (abc + abd) + Be^{-i\phi} E_2 (da^2 + cb^2) \quad (\text{A.9})$$

$$E_2 = \frac{E_i (abc + abd)}{1 - Be^{-i\phi} (da^2 + cb^2)} \quad (\text{A.10})$$

which leads to

$$E_o = E_i (ca^2 + db^2) + \frac{Be^{-i\phi} E_i (abc + abd)^2}{1 - Be^{-i\phi} (da^2 + cb^2)} \quad (\text{A.11})$$

$$\Downarrow$$

$$\frac{E_o}{E_i} = (ca^2 + db^2) + \frac{Be^{-i\phi} (abc + abd)^2}{1 - Be^{-i\phi} (da^2 + cb^2)} \quad (\text{A.12})$$

Inserting the expressions for a , b , c and d we get

$$\begin{aligned} \frac{E_o}{E_i} &= \left(A\gamma e^{-i\psi} (\tau e^{-i\varphi})^2 + A e^{-i\theta} (\kappa e^{-i(\varphi+\frac{\pi}{2})})^2 \right) \\ &+ \frac{Be^{-i\phi} (\tau e^{-i\varphi} \kappa e^{-i(\varphi+\frac{\pi}{2})} A\gamma e^{-i\psi} + \tau e^{-i\varphi} \kappa e^{-i(\varphi+\frac{\pi}{2})} A e^{-i\theta})^2}{1 - Be^{-i\phi} (A e^{-i\theta} (\tau e^{-i\varphi})^2 + A\gamma e^{-i\psi} (\kappa e^{-i(\varphi+\frac{\pi}{2})})^2)} \end{aligned} \quad (\text{A.13})$$

$$\begin{aligned} &= A (\gamma \tau^2 e^{-i(\psi+2\varphi)} + \kappa^2 e^{-i(\theta+2\varphi+\pi)}) \\ &+ \frac{A^2 B \tau^2 \kappa^2 e^{-i\phi} (\gamma e^{-i(2\varphi+\frac{\pi}{2}+\psi)} + e^{-i(2\varphi+\frac{\pi}{2}+\theta)})^2}{1 - A B e^{-i\phi} (\tau^2 e^{-i(\theta+2\varphi)} + \gamma \kappa^2 e^{-i(\psi+2\varphi+\pi)})} \end{aligned} \quad (\text{A.14})$$

$$\begin{aligned} &= A e^{-i2\varphi} (\gamma \tau^2 e^{-i\psi} - \kappa^2 e^{-i\theta}) \\ &+ \frac{A^2 B \tau^2 \kappa^2 e^{-i\phi} (\gamma e^{-i(2\varphi+\frac{\pi}{2}+\psi)} + e^{-i(2\varphi+\frac{\pi}{2}+\theta)})^2}{1 - A B e^{-i(\phi+2\varphi)} (\tau^2 e^{-i\theta} - \gamma \kappa^2 e^{-i\psi})} \end{aligned} \quad (\text{A.15})$$

$$\begin{aligned} &= A e^{-i2\varphi} (\gamma \tau^2 e^{-i\psi} - \kappa^2 e^{-i\theta}) \\ &+ \frac{A^2 B \tau^2 \kappa^2 e^{-i\phi} (\gamma^2 e^{-i(4\varphi+\pi+2\psi)} + e^{-i(4\varphi+\pi+2\theta)} + 2\gamma e^{-i(4\varphi+\pi+\psi+\theta)})}{1 - A B e^{-i(\phi+2\varphi)} (\tau^2 e^{-i\theta} - \gamma \kappa^2 e^{-i\psi})} \end{aligned} \quad (\text{A.16})$$

$$\begin{aligned} &= A e^{-i2\varphi} (\gamma \tau^2 e^{-i\psi} - \kappa^2 e^{-i\theta}) \\ &- \frac{A^2 B \tau^2 \kappa^2 e^{-i(\phi+4\varphi)} (\gamma^2 e^{-i2\psi} + e^{-i2\theta} + 2\gamma e^{-i(\psi+\theta)})}{1 - A B e^{-i(\phi+2\varphi)} (\tau^2 e^{-i\theta} - \gamma \kappa^2 e^{-i\psi})} \end{aligned} \quad (\text{A.17})$$

$$\frac{E_o}{E_i} = Ae^{-i2\varphi} \left(\gamma\tau^2 e^{-i\psi} - \kappa^2 e^{-i\theta} \right) - \frac{A^2 B \tau^2 \kappa^2 e^{-i(\phi+4\varphi)} \left(\gamma e^{-i\psi} + e^{-i\theta} \right)^2}{1 - AB e^{-i(\phi+2\varphi)} (\tau^2 e^{-i\theta} - \gamma \kappa^2 e^{-i\psi})} \quad (\text{A.18})$$

The output intensity of the device can then be expressed as

$$\begin{aligned} \frac{I_o}{I_i} &= \left| \frac{E_o}{E_i} \right|^2 \\ &= \left| Ae^{-i2\varphi} \left(\gamma\tau^2 e^{-i\psi} - \kappa^2 e^{-i\theta} \right) - \frac{A^2 B \tau^2 \kappa^2 e^{-i(\phi+4\varphi)} \left(\gamma e^{-i\psi} + e^{-i\theta} \right)^2}{1 - AB e^{-i(\phi+2\varphi)} (\tau^2 e^{-i\theta} - \gamma \kappa^2 e^{-i\psi})} \right|^2 \end{aligned} \quad (\text{A.19})$$

The first term contains none of the parameters associated with the racetrack ring section. It thus describes the field in the absence of the ring section i.e. the undercoupled case. The second term contains in the nominator the terms describing the two overcoupled pathways and the second term in the denominator describes the two resonant pathways. One interesting observation is the phase shift contributions of the racetrack ψ and those associated with the MZI equivalent region φ and Θ . It is seen that inducing a phase shift ψ or Θ has twice the effect on the total phase shift than does an induced phase shift in the ring section ϕ .

Appendix B

Reflow heating simulation

In order to assess the thermal distribution for the reflow experiment where a chip with patterned ZEP520A is placed face down over an air cavity, which is etched into a silicon wafer and placed on a hotplate at 145°C . This system was simulated using COMSOL Multiphysics 4.4 and the "Heat Transfer in Solids" module. Here air is modelled as a moist air with a relative humidity of 0.5 at 1atm and a lateral flow defined as $-5\text{m/s} \cdot \hat{x}$. The resulting temperature and flow profile can be seen on figure B.2b. It is seen, that the chip is uniformly heated to the hotplate temperature regardless of airflow. The box size was chosen to be 3cm wide and 5mm high. The boundary conditions chosen were ambient temperature along the air boundary, 145°C along the bottom boundary representing the hotplate/wafer interface. Finally, the sides of the wafer is chosen to be thermal insulating as the simulation window has been chosen wide enough that heat flow through those small boundaries does not affect the center where the chip is located.

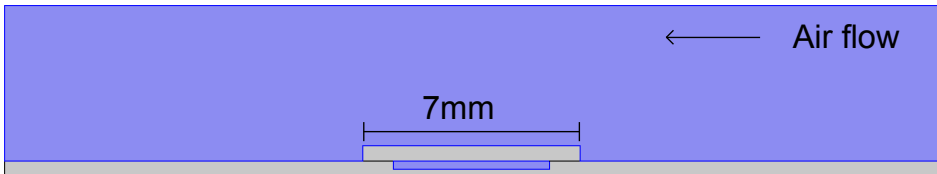
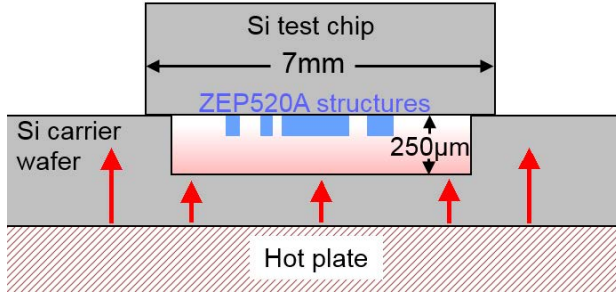
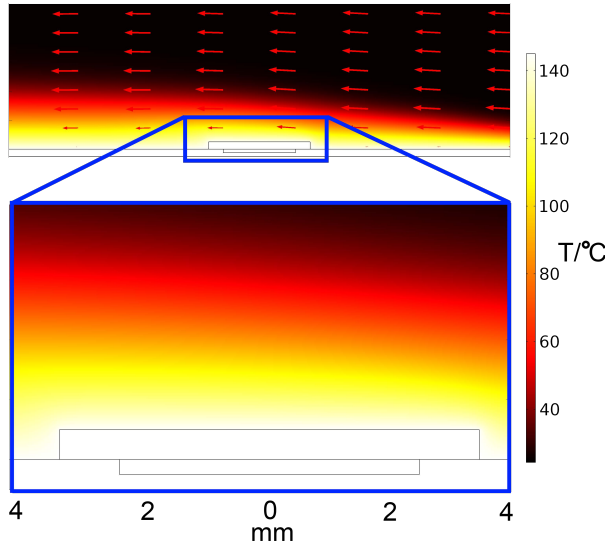


Figure B.1: Simulation box for simulating the thermal distribution. The entire box is 3cm wide and 5.5mm high. The air gap between the chip and the wafer is $250\mu\text{m}$ deep.



(a)



(b)

Figure B.2: (a): Conceptual outline of the reflow experiment. The test chip is placed upside down on a Si carrier wafer with an etched trench which allows for the air around the ZEP520A structures to reach the reflow temperature and provides some ambient cooling of the chip as the backside is exposed. Relative sizes are not to scale. (b): Finite elements analysis using COMSOL Multiphysics to solve for the steady state temperature distribution during the experiment under typical fumehood air flow. Top image shows the solution for the entire simulation window with red arrows indicating direction of airflow. Bottom image shows a closeup of the structure of interest. Temperature drops less than half a celsius from the carrier wafer to the exposed test chip backside.

Appendix C

Thermal simulations of SiN hybrid phase shifter

Running current through a PiN junction not only changes the charge density in the intrinsic region, it also leads to ohmic heating.

Both free carrier concentration and heating contributes to the phase change when a PiN junction is used as a phase shifter.

In the case of the hybrid SiN/Si phase shifter the PiN junction is in the Si slab and the slab therefore effectively acts as a heat source as well as a free carrier based phase shifter. Unlike phase shift induced by free carriers, the thermal phase shift comes from all heated components.

The thermal distribution is simulated using COMSOL Multiphysics 4.4. The joule heating module is used and the simulation window can be seen on [C.1](#). The upper domain is stagnant room temperature air. The lower boundary is set $5\mu\text{m}$ below the Si_3N_4 nanowire in the SiO_2 layer at room temperature as well. The boundaries on the side of the simulation box are set to allow outflow of heat in the presence of a temperature gradient, but it could be argued that a set ambient temperature might be more appropriate considering the extend of the simulation box. However, it was found not to affect the temperature distribution at the SiN core by any notable amount. These boundary conditions are chosen to mimic the laboratory conditions where the upper face of the chip is exposed to ambient air and the bottom of the chip is set on a thermostatic holder likewise set to room temperature. The size of the simulation window is chosen so the temperature distribution in the area corresponding to the lowest order TM mode profile converges. The width of the simulation window of $20\mu\text{m}$ also corresponds to the width

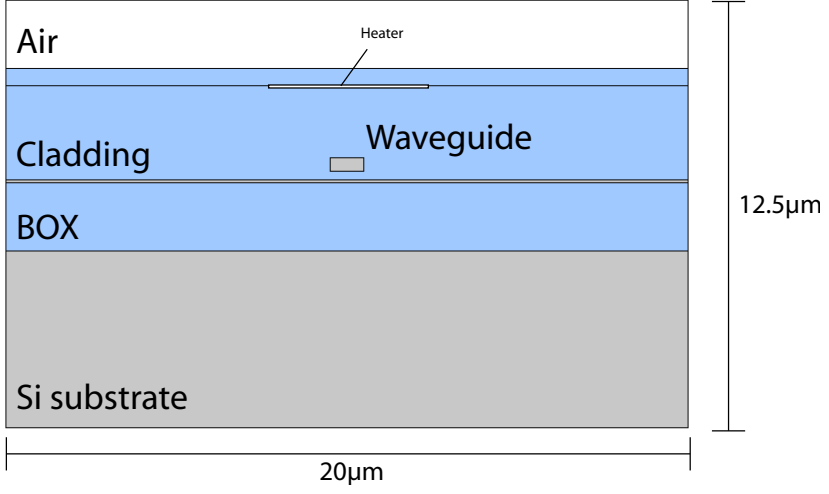


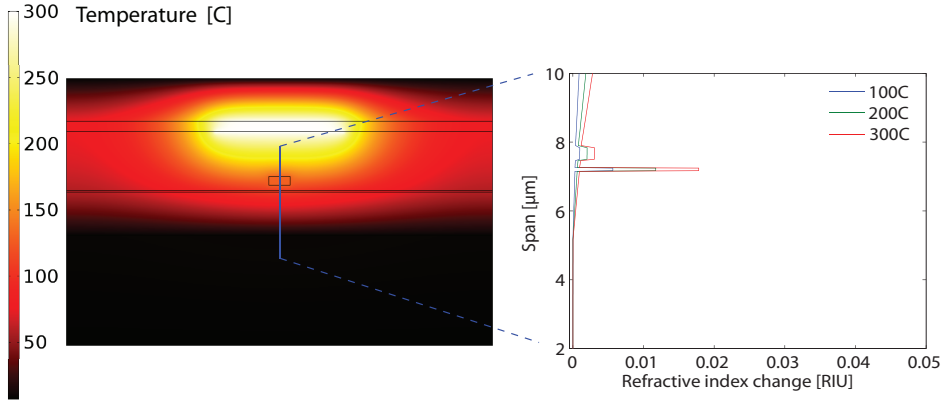
Figure C.1: Simulation window with materials indicated. A $6\mu\text{m}$ wide heater is included $2\mu\text{m}$ above the SiN waveguide, embedded in the cladding oxide. The structure can thus be heated in two ways; by running a current through either the heater or the PIN diode in the slab.

of the phase shifter slabs in the IME Astar chip designs.

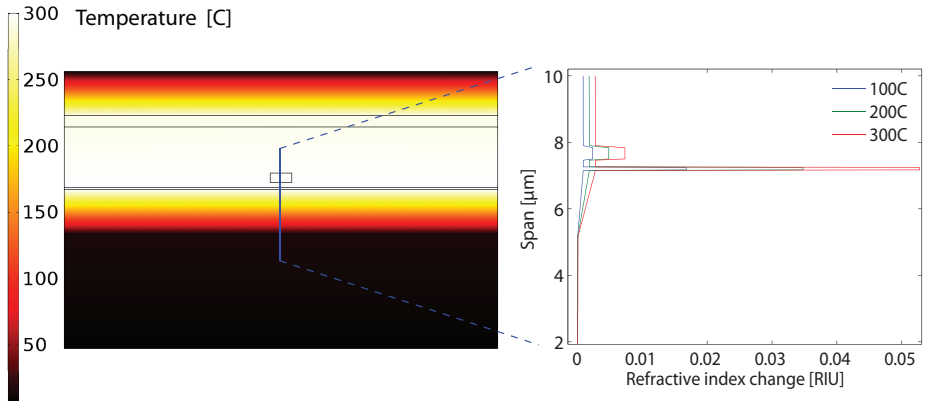
The result of the simulation is the steady state temperature distribution seen on figure C.2. Depending on whether the source of heating is the SOI slab or the metal heater embedded in the cladding, the temperature distribution varies significantly. This is largely attributed to the thermal conductivity of silicon and in particular the Si substrate which acts as an efficient heatsink compared to air at the top boundary.

Material	dn/dT [RIU/ $^{\circ}\text{K}$]	ρ [kg/m^3]	k [$\text{W}/\text{m}\cdot^{\circ}\text{K}$]	C_p [$\text{J}/\text{kg}\cdot^{\circ}\text{K}$]
SiO_2	$0.95 \cdot 10^{-5}$	2200	1.4	730
Si	$1.8 \cdot 10^{-4}$	2329	131	700
Si_3N_4	$2.45 \cdot 10^{-5}$	3200	30	710
Air	N/A	1.225	0.024	1010

It is clear that any mode overlap with the Si slab will experience the strongest modulation.



(a)



(b)

Figure C.2: Temperature profile and material refractive index change for (a): Sample heated via metal heater embedded in cladding oxide, and (b): Ohmic heating from the PIN junction in the silicon slab.

Bibliography

- [1] D. Pierce and W. Spicer, “Electronic Structure of Amorphous Si from Photoemission and Optical Studies,” *Physical Review B*, vol. 5, no. 8, pp. 3017–3029, 1972.
- [2] D. E. Aspnes and J. B. Theeten, “Optical Properties of the Interface between Si and Its Thermally Grown Oxide,” *Phys. Rev. Lett.*, vol. 43, no. 14, p. 1046, 1979.
- [3] S. Sze and J. Irvin, “Resistivity, mobility and impurity levels in GaAs, Ge, and Si at 300K,” *Solid-State Electronics*, vol. 11, no. 6, pp. 599–602, 1968.
- [4] B. K. Jalali and S. K. Fathpour, “Silicon photonics,” *Journal of Lightwave Technology*, vol. 24, no. 12, pp. 4600–4615, 2006. [Online]. Available: [http://books.google.com/books?hl=en{&}lr={&}id=PgmmFRYE6a0C{&}oi=fnd{&}pg=PA1{&}dq=silicon+photonics{&}ots=SxTvnEZXu{&}sig=XI3a9MgviIrSa2rNkpVt1FZ21g](http://books.google.com/books?hl=en&lr={&}id=PgmmFRYE6a0C{&}oi=fnd{&}pg=PA1{&}dq=silicon+photonics{&}ots=SxTvnEZXu{&}sig=XI3a9MgviIrSa2rNkpVt1FZ21g)
- [5] M. Hochberg and T. Baehr-Jones, “Towards fabless silicon photonics,” *Nature Photonics*, vol. 4, no. 8, pp. 492–494, 2010. [Online]. Available: <http://www.nature.com/doifinder/10.1038/nphoton.2010.172>
- [6] A. Rickman, “The commercialization of silicon photonics,” *Nature Photonics*, vol. 8, no. 8, pp. 579–582, 2014. [Online]. Available: <http://www.nature.com/doifinder/10.1038/nphoton.2014.175>
- [7] T. Morioka, “New generation optical infrastructure technologies; EXAT initiatives; towards 2020 and beyond,” *OptoElectronics and Communications Conference, 2009. OECC 2009. 14th*, no. 81, pp. 1–2, 2009.

- [8] O. Boyraz and B. Jalali, "Demonstration of a silicon Raman laser." *Optics express*, vol. 12, no. 21, pp. 5269–5273, 2004.
- [9] L. Vivien, J. Osmond, J.-M. Fédéli, D. Marris-Morini, P. Crozat, J.-F. Damlencourt, E. Cassan, Y. Lecunff, and S. Laval, "42 GHz p.i.n Germanium photodetector integrated in a silicon-on-insulator waveguide." *Optics Express*, vol. 17, no. 8, pp. 6252–7, 2009. [Online]. Available: <http://www.ncbi.nlm.nih.gov/pubmed/19365450>
- [10] S. Akiyama and T. Usuki, "High-speed and efficient silicon modulator based on forward-biased pin diodes," *Frontiers in Physics*, vol. 2, no. November, pp. 1–7, 2014. [Online]. Available: <http://journal.frontiersin.org/article/10.3389/fphy.2014.00065/abstract>
- [11] R. Soref and B. Bennett, "Electrooptical effects in silicon," *IEEE Journal of Quantum Electronics*, vol. 23, no. 1, pp. 123–129, 1987.
- [12] A. Liu, L. Liao, D. Rubin, H. Nguyen, B. Ciftcioglu, Y. Chetrit, N. Izhaky, and M. Paniccia, "High-speed optical modulation based on carrier depletion in a silicon waveguide," *Optics Express*, vol. 15, no. 2, p. 660, jan 2007. [Online]. Available: <http://www.ncbi.nlm.nih.gov/pubmed/19532289><https://www.osapublishing.org/oe/abstract.cfm?uri=oe-15-2-660>
- [13] C. Gunn, "CMOS Photonics for High-Speed Interconnects," *IEEE Micro*, vol. 26, no. 2, pp. 58–66, 2006.
- [14] J. Petrilla, "CFP MSA Hardware Specification," *ReVision*, no. June, pp. 1–53, 2010. [Online]. Available: <http://www.cfp-msa.org/documents.html>
- [15] A. E.-J. Lim, Junfeng Song, Qing Fang, Chao Li, Xiaoguang Tu, Ning Duan, Kok Kiong Chen, R. P.-C. Tern, and Tsung-Yang Liow, "Review of Silicon Photonics Foundry Efforts," *IEEE Journal of Selected Topics in Quantum Electronics*, vol. 20, no. 4, pp. 405–416, jul 2014. [Online]. Available: <http://ieeexplore.ieee.org/lpdocs/epic03/wrapper.htm?arnumber=6676843>
- [16] a. D. Buckingham and J. a. Pople, "Theoretical Studies of the Kerr Effect: I - Deviations from a Linear Polarization Law," *Proceedings of the Physical Society. Section A*, vol. 68, no. 11, pp. 1091–1091, 1955.

- [17] R. H. Stolen and C. Lin, “Self-phase-modulation in silica optical fibers,” *Physical Review A*, vol. 17, no. 4, pp. 1448–1453, 1978.
- [18] I.-w. Hsieh, X. Chen, J. I. Dadap, N. C. Panoiu, R. M. Osgood, S. J. McNab, and Y. A. Vlasov, “Cross-phase modulation-induced spectral and temporal effects on co-propagating femtosecond pulses in silicon photonic wires.” *Optics express*, vol. 15, no. 3, pp. 1135–1146, 2007.
- [19] H. Fukuda, K. Yamada, T. Shoji, M. Takahashi, T. Tsuchizawa, T. Watanabe, J.-I. Takahashi, and S.-I. Itabashi, “Four-wave mixing in silicon wire waveguides.” *Optics express*, vol. 13, no. 12, pp. 4629–4637, 2005.
- [20] F. Da Ros, D. Vukovic, A. Gajda, K. Dalgaard, L. Zimmermann, B. Tillack, M. Galili, K. Petermann, and C. Peucheret, “Phase regeneration of DPSK signals in a silicon waveguide with reverse-biased p-i-n junction.” *Optics express*, vol. 22, no. 5, pp. 5029–36, 2014. [Online]. Available: <http://www.ncbi.nlm.nih.gov/pubmed/24663841>
- [21] Y. Okawachi, K. Saha, J. S. Levy, Y. H. Wen, M. Lipson, and A. L. Gaeta, “Octave-spanning frequency comb generation in a silicon nitride chip.” *Optics letters*, vol. 36, no. 17, pp. 3398–3400, 2011.
- [22] A. G. Griffith, R. K. W. Lau, J. Cardenas, Y. Okawachi, R. Fain, Y. Ho, D. Lee, M. Yu, C. T. Phare, B. Carl, A. L. Gaeta, and M. Lipson, “Silicon-chip mid-infrared frequency comb generation,” *Nature Communications*, vol. 6, no. 6299, 2015.
- [23] K.-Y. Wang and A. C. Foster, “Ultralow power continuous-wave frequency conversion in hydrogenated amorphous silicon waveguides,” *Optics Letters*, vol. 37, no. 8, p. 1331, 2012.
- [24] H. Hu, E. Palushani, M. Galili, H. C. H. Mulvad, A. Clausen, L. K. Oxenløwe, and P. Jeppesen, “640 Gbit/s and 1.28 Tbit/s polarisation insensitive all optical wavelength conversion.” *Optics express*, vol. 18, no. 10, pp. 9961–6, may 2010. [Online]. Available: <http://www.ncbi.nlm.nih.gov/pubmed/20588850>
- [25] S. Lavdas, J. B. Driscoll, R. R. Grote, R. M. Osgood, and N. C. Panoiu, “Pulse compression in adiabatically tapered silicon photonic wires,” *Optics Express*, vol. 22, no. 6, pp. 755–757, 2014. [Online]. Available: <http://www.ncbi.nlm.nih.gov/pubmed/24663978>

- [26] K. K. Lee, D. R. Lim, H.-C. Luan, A. Agarwal, J. Foresi, and L. C. Kimerling, "Effect of size and roughness on light transmission in a Si/SiO₂ waveguide: Experiments and model," *Applied Physics Letters*, vol. 77, no. 11, p. 1617, 2000. [Online]. Available: <http://link.aip.org/link/APPLAB/v77/i11/p1617/s1{&}Agg=doi>
- [27] G. P. Agrawal, *Fiber-Optic communication systems*, 4th ed. Wiley, 2010.
- [28] T. Barwicz and H. Haus, "Three-dimensional analysis of scattering losses due to sidewall roughness in microphotonic waveguides," *Journal of Lightwave Technology*, vol. 23, no. 9, pp. 2719–2732, 2005. [Online]. Available: <http://ieeexplore.ieee.org/lpdocs/epic03/wrapper.htm?arnumber=1506850>
- [29] "Soitec FD-2D Wafers." [Online]. Available: http://www.soitec.com/pdf/Soitec-FD-2D-product{__}brief.pdf
- [30] U. Fischer, T. Zinke, J.-R. Kropp, F. Arndt, and K. Petermann, "0.1 dB/cm waveguide losses in single-mode SOI rib waveguides," *IEEE Photonics Technology Letters*, vol. 8, no. 5, pp. 647–648, 1996. [Online]. Available: <http://ieeexplore.ieee.org/lpdocs/epic03/wrapper.htm?arnumber=491567>
- [31] C. A. Barrios, V. R. Almeida, R. Panepucci, and M. Lipson, "Electrooptic Modulation of Silicon-on-Insulator Submicrometer-Size Waveguide Devices," *Journal of Lightwave Technology*, vol. 21, no. 10, pp. 2332–2339, 2003.
- [32] A. Gajda, L. Zimmermann, M. Jazayerifar, G. Winzer, H. Tian, R. Elschner, T. Richter, C. Schubert, B. Tillack, and K. Petermann, "Highly efficient CW parametric conversion at 1550 nm in SOI waveguides by reverse biased p-i-n junction," *Optics Express*, vol. 20, no. 12, p. 13100, 2012.
- [33] a. Gajda, F. Da Ros, D. Vukovic, L. Zimmermann, C. Peucheret, B. Tillack, and K. Peterman, "High efficiency wavelength conversion of 40 Gbps signals at 1550 nm in SOI nano-rib waveguides using p-i-n diodes," *10th International Conference on Group IV Photonics*, vol. 3, pp. 160–161, 2013. [Online]. Available: <http://ieeexplore.ieee.org/lpdocs/epic03/wrapper.htm?arnumber=6644420>

- [34] W.-C. Lai, S. Chakravarty, X. Wang, C. Lin, and R. T. Chen, “On-chip methane sensing by near-IR absorption signatures in a photonic crystal slot waveguide,” *Optics Letters*, vol. 36, no. 6, pp. 984–986, 2011.
- [35] H. Zengzhi, Y. Zhang, C. Zeng, D. Li, and M. S. Nisar, “High Confinement Factor Ridge Slot Waveguide for Optical Sensing,” vol. 27, no. 22, pp. 2395–2398, 2015.
- [36] Q. Liu, X. Tu, K. W. Kim, J. S. Kee, Y. Shin, K. Han, Y.-J. Yoon, G.-Q. Lo, and M. K. Park, “Highly sensitive Mach–Zehnder interferometer biosensor based on silicon nitride slot waveguide,” *Sensors and Actuators B: Chemical*, vol. 188, pp. 681–688, 2013. [Online]. Available: <http://linkinghub.elsevier.com/retrieve/pii/S0925400513008502>
- [37] H. Zhang, J. Zhang, S. Chen, J. Song, J. S. Kee, M. Yu, and G.-Q. Lo, “CMOS-Compatible Fabrication of Silicon-Based Sub-100-nm Slot Waveguide With Efficient Channel-Slot Coupler,” *IEEE Photonics Technology Letters*, vol. 24, no. 1, pp. 10–12, 2012. [Online]. Available: <http://ieeexplore.ieee.org/lpdocs/epic03/wrapper.htm?arnumber=6044704>
- [38] L. C. Kimerling, H. Atwater, M. L. Brongersma, L. D. Negro, T. L. Koch, P. Fauchet, M. Lipson, J. Michel, and C. A. Barrios, “Electrically pumped extrinsic semiconductor optical amplifier with slot waveguide,” 2013. [Online]. Available: <https://www.google.com/patents/US8619358>
- [39] P. Bienstman and R. Baets, “Optical modelling of photonic crystals and VCSELs using eigenmode expansion and perfectly matched layers,” *Optical and Quantum Electronics*, vol. 33, no. 4-5, pp. 327–341, 2001.
- [40] Y. Chung and N. Dagli, “An assessment of finite difference beam propagation method,” *IEEE Journal of Quantum Electronics*, vol. 26, no. 2, pp. 1335–1339, 1990. [Online]. Available: http://ieeexplore.ieee.org/xpls/abs{__}all.jsp?arnumber=59679
- [41] K. Yee, “Numerical solution of initial boundary value problems involving Maxwell’s equations in isotropic media,” pp. 302–307, 1966. [Online]. Available: <http://ieeexplore.ieee.org/lpdocs/epic03/>

[wrapper.htm?arnumber=1138693&\delimiter"026E30F\\$&nhttp://ieeexplore.ieee.org/xpls/abs/_all.jsp?arnumber=1138693](http://ieeexplore.ieee.org/xpls/abs/_all.jsp?arnumber=1138693)

- [42] A. Taflov, "Application of the Finite-Difference Time-Domain Method to Sinusoidal Steady-State Electromagnetic-Penetration Problems," pp. 191–202, 1980. [Online]. Available: <http://ieeexplore.ieee.org/lpdocs/epic03/wrapper.htm?arnumber=4091372>
- [43] J. A. Roden and S. D. Gedney, "Convolution PML (CPML): An efficient FDTD implementation of the CFS-PML for arbitrary media," *Microwave and Optical Technology Letters*, vol. 27, no. 5, pp. 334–339, 2000. [Online]. Available: [http://doi.wiley.com/10.1002/1098-2760\(20001205\)27:5<334::AID-MOP14>3.0.CO;2-A](http://doi.wiley.com/10.1002/1098-2760(20001205)27:5<334::AID-MOP14>3.0.CO;2-A)
- [44] F. Zheng and Z. Chen, "Numerical dispersion analysis of the unconditionally stable 3-D ADI-FDTD method," *IEEE Transactions on Microwave Theory and Techniques*, vol. 49, no. 5, pp. 1006–1009, 2001.
- [45] J. T. Robinson, K. Preston, O. Painter, and M. Lipson, "First-principle derivation of gain in high-index-contrast waveguides," *Optics Express*, vol. 16, no. 21, p. 16659, oct 2008.
- [46] J. S. Orcutt, S. D. Tang, S. Kramer, K. Mehta, H. Li, V. Stojanović, and R. J. Ram, "Low-loss polysilicon waveguides fabricated in an emulated high-volume electronics process," *Optics Express*, vol. 20, no. 7, p. 7243, 2012.
- [47] S. Sridaran and S. a. Bhav, "Nanophotonic devices on thin buried oxide Silicon-On-Insulator substrates." *Optics express*, vol. 18, no. 4, pp. 3850–3857, 2010.
- [48] S. Grillanda and F. Morichetti, "Light-induced metal-like surface of silicon photonic waveguides," *Nature Communications*, vol. 6, p. 8182, 2015. [Online]. Available: <http://www.nature.com/doifinder/10.1038/ncomms9182>
- [49] L. Alloatti, C. Koos, and J. Leuthold, "Optical loss by surface transfer doping in silicon waveguides," *Applied Physics Letters*, vol. 107, no. 3, p. 031107, 2015. [Online]. Available: <http://scitation.aip.org/content/aip/journal/apl/107/3/10.1063/1.4927313>

- [50] C.-S. Guo, L.-B. Luo, G.-D. Yuan, X.-B. Yang, R.-Q. Zhang, W.-J. Zhang, and S.-T. Lee, "Surface Passivation and Transfer Doping of Silicon Nanowires," *Angewandte Chemie*, vol. 121, no. 52, pp. 10 080–10 084, 2009. [Online]. Available: <http://doi.wiley.com/10.1002/ange.200904890>
- [51] T. Yamaguchi, H. Namatsu, M. Nagase, K. Yamazaki, and K. Kurihara, "A new approach to reducing line-edge roughness by using a cross-linked positive-tone resist," *Japanese Journal of Applied Physics Part 1-Regular Papers Short Notes & Review Papers*, vol. 38, no. 12B, pp. 7114–7118, 1999. [Online]. Available: <http://gotosi.riken.go.jp/000166201800032>
- [52] T. Yamaguchi, H. Namatsu, M. Nagase, K. Yamazaki, and K. Kurihara, "Suppressed Aggregate Extraction Development (SAGEX) Resists." *Journal of Photopolymer Science and Technology*, vol. 13, no. 3, pp. 427–433, 2000.
- [53] T. Yamaguchi, K. Yamazaki, and H. Namatsu, "Influence of molecular weight of resist polymers on surface roughness and line-edge roughness," *Journal of Vacuum Science & Technology B: Microelectronics and Nanometer Structures*, vol. 22, no. 6, p. 2604, 2004. [Online]. Available: <http://scitation.aip.org/content/avs/journal/jvstb/22/6/10.1116/1.1805546>
- [54] L. E. Ocola and a. Stein, "Effect of cold development on improvement in electron-beam nanopatterning resolution and line roughness," *Journal of Vacuum Science & Technology B: Microelectronics and Nanometer Structures*, vol. 24, no. 6, p. 3061, 2006.
- [55] B. C. L. Chochos, E. Ismailova, C. Brochon, N. Leclerc, R. Tiron, C. Sourd, P. Bandelier, J. Foucher, H. Ridaoui, A. Dirani, O. Soppera, D. Perret, C. Brault, C. A. Serra, and G. Hadzioannou, "Hyperbranched Polymers for Photolithographic Applications – Towards Understanding the Relationship between Chemical Structure of Polymer Resin and Lithographic Performances," *ADVance materials*, vol. 21, pp. 1121–1125, 2009.
- [56] H. Namatsu, "Three-dimensional siloxane resist for the formation of nanopatterns with minimum linewidth fluctuations," *Journal of Vacuum Science & Technology B: Microelectronics and Nanometer*

- Structures*, vol. 16, no. 1, p. 69, jan 1998. [Online]. Available: <http://scitation.aip.org/content/avs/journal/jvstb/16/1/10.1116/1.589837>
- [57] H. Namatsu, T. Yamaguchi, and K. Kurihara, "Resist Materials Providing Small Line-Edge Roughness," *MRS Proceedings*, vol. 584, p. 135, jan 1999. [Online]. Available: <http://journals.cambridge.org/abstract{ }S1946427400182387>
- [58] M. Borselli, T. Johnson, and O. Painter, "Beyond the Rayleigh scattering limit in high-Q silicon microdisks: theory and experiment." *Optics express*, vol. 13, no. 5, pp. 1515–1530, 2005.
- [59] B. P. Downey, D. J. Meyer, R. Bass, D. S. Katzer, and S. C. Binari, "Thermally reflowed ZEP 520A for gate length reduction and profile rounding in T-gate fabrication," *Journal of Vacuum Science & Technology B: Microelectronics and Nanometer Structures*, vol. 30, no. 5, p. 051603, 2012. [Online]. Available: <http://link.aip.org/link/JVTBD9/v30/i5/p051603/s1{&}Agg=doi>
- [60] G. C. Schwartz, "Reactive ion etching of silicon," *Journal of Vacuum Science and Technology*, vol. 16, no. 2, p. 410, 1979.
- [61] K. K. Lee, D. R. Lim, L. C. Kimerling, J. Shin, and F. Cerrina, "Fabrication of ultralow-loss Si/SiO(2) waveguides by roughness reduction." *Optics letters*, vol. 26, no. 23, pp. 1888–1890, 2001.
- [62] B. E. Deal and A. S. Grove, "General Relationship for the Thermal Oxidation of Silicon," *Journal of Applied Physics*, vol. 36, no. 12, pp. 3770–3778, 1965.
- [63] S. A. Campbell, *Fabrication engineering at the micro and nanoscale*, 3rd ed. Oxford University press, 2008.
- [64] H. Z. Massoud, "Thermal Oxidation of Silicon in Dry Oxygen: Growth-Rate Enhancement in the Thin Regime," *Journal of The Electrochemical Society*, vol. 132, no. 11, p. 2693, 1985.
- [65] A. Fargeix, G. Ghibaudo, and G. Kamarinos, "A revised analysis of dry oxidation of silicon," *Journal of Applied Physics*, vol. 54, no. 5, p. 2878, 1983. [Online]. Available: <http://scitation.aip.org/content/aip/journal/jap/54/5/10.1063/1.332286>

- [66] M. Tang, "Growth temperature dependence of the Si (001)/SiO₂ interface width," *Applied physics letters*, vol. 64, no. 6, pp. 748–750, 1994.
- [67] E. P. EerNisse, "Stress in thermal SiO₂ during growth," *Applied Physics Letters*, vol. 35, no. 1, pp. 8–10, 1979. [Online]. Available: <http://link.aip.org/link/APPLAB/v35/i1/p8/s1{&}Agg=doi>
- [68] K. P. Yap, A. Delage, J. Lapointe, B. Lamontagne, J. Schmid, P. Waldron, B. Syrett, and S. Janz, "Correlation of Scattering Loss, Sidewall Roughness and Waveguide Width in Silicon-on-Insulator (SOI) Ridge Waveguides," *Journal of Lightwave Technology*, vol. 27, no. 18, pp. 3999–4008, 2009.
- [69] M. Pu, L. Liu, H. Ou, K. Yvind, and J. M. Hvam, "Ultra-low-loss inverted taper coupler for silicon-on-insulator ridge waveguide," *Optics Communications*, vol. 283, no. 19, pp. 3678–3682, 2010. [Online]. Available: <http://dx.doi.org/10.1016/j.optcom.2010.05.034>
- [70] A. H. M. Smets, M. a. Wank, B. Vet, M. Fischer, R. a. C. M. M. Van Swaaij, M. Zeman, D. C. Bobela, C. R. Wronski, and R. M. C. M. Van De Sanden, "The relation between the bandgap and the anisotropic nature of hydrogenated amorphous silicon," *IEEE Journal of Photovoltaics*, vol. 2, no. 2, pp. 94–98, 2012.
- [71] B. von Blanckenhagen, D. Tonova, and J. Ullmann, "Application of the Tauc-Lorentz formulation to the interband absorption of optical coating materials." *Applied optics*, vol. 41, no. 16, pp. 3137–3141, 2002.
- [72] R. V. Kruzelecky, C. Ukah, D. Racansky, S. Zukotynski, and J. M. Perz, "Interband optical absorption in amorphous silicon," *Journal of Non-Crystalline Solids*, vol. 103, no. 2-3, pp. 234–249, 1988. [Online]. Available: <http://www.sciencedirect.com/science/article/B6TXM-48J4YVK-HH/2/ba8e69d7ab2bbce383b8b360eadb5edd>
- [73] B. Kuyken, H. Ji, S. Clemmen, S. K. Selvaraja, H. Hu, M. Pu, M. Galili, P. Jeppesen, G. Morthier, S. Massar, L. K. Oxenløwe, G. Roelkens, and R. Baets, "Nonlinear properties of and nonlinear processing in hydrogenated amorphous silicon waveguides." *Optics express*, vol. 19, no. 26, pp. B146–53, dec 2011. [Online]. Available: <http://www.ncbi.nlm.nih.gov/pubmed/22274011>

- [74] D. L. Staebler and C. R. Wronski, "Reversible conductivity changes in discharge-produced amorphous Si," *Applied Physics Letters*, vol. 31, no. 4, pp. 292–294, 1977.
- [75] —, "Optically induced conductivity changes in discharge-produced hydrogenated amorphous silicon," *Journal of Applied Physics*, vol. 51, no. 1980, pp. 3262–3268, 1980.
- [76] F. Kohler, T. Zimmermann, S. Muthmann, A. Gordijn, and R. Carius, "Structural Order and Staebler-Wronski Effect in Hydrogenated Amorphous Silicon Films and Solar Cells," *IEEE Journal of Photovoltaics*, vol. 4, no. 1, pp. 4–9, 2014. [Online]. Available: <http://ieeexplore.ieee.org/lpdocs/epic03/wrapper.htm?arnumber=6661343>
- [77] T. Kamei, N. Hata, A. Matsuda, T. Uchiyama, S. Amano, K. Tsukamoto, Y. Yoshioka, and T. Hirao, "Deposition and extensive light soaking of highly pure hydrogenated amorphous silicon," *Applied Physics Letters*, vol. 68, no. 17, p. 2380, 1996. [Online]. Available: <http://scitation.aip.org/content/aip/journal/apl/68/17/10.1063/1.116140>
- [78] H. Dersch, "Light-induced dangling bonds in hydrogenated amorphous silicon," *Applied Physics Letters*, vol. 38, no. 6, p. 456, 1981. [Online]. Available: <http://scitation.aip.org/content/aip/journal/apl/38/6/10.1063/1.92402>
- [79] H. Branz, "Hydrogen collision model: Quantitative description of metastability in amorphous silicon." *Physical Review B*, vol. 59, no. 8, pp. 5498–5512, 1999.
- [80] T. Su, P. C. Taylor, G. Ganguly, and D. E. Carlson, "Direct Role of Hydrogen in the Staebler-Wronski Effect in Hydrogenated Amorphous Silicon," *Physical Review Letters*, vol. 89, no. 1, p. 015502, 2002. [Online]. Available: <http://link.aps.org/doi/10.1103/PhysRevLett.89.015502>
- [81] M. Fehr, A. Schnegg, B. Rech, O. Astakhov, F. Finger, R. Bittl, C. Teutloff, and K. Lips, "Metastable Defect Formation at Microvoids Identified as a Source of Light-Induced Degradation in a-Si:H," *Physical Review Letters*, vol. 112, no. 6, p. 066403, 2014. [Online]. Available: <http://link.aps.org/doi/10.1103/PhysRevLett.112.066403>

- [82] L. Liao, D. R. Lim, A. M. Agarwal, X. Duan, K. K. Lee, and L. C. Kimerling, "Optical transmission losses in polycrystalline silicon strip waveguides: Effects of waveguide dimensions, thermal treatment, hydrogen passivation, and wavelength," *Journal of Electronic Materials*, vol. 29, no. 12, pp. 1380–1386, 2000.
- [83] J. Tauc, R. Grigorovi, and A. Vanc, "Optical Properties and Electronic Structure of Amorphous Germanium," *Basic solid state physics*, vol. 15, pp. 627–637, 1966.
- [84] N. Savvides, "Deposition parameters and film properties of hydrogenated amorphous silicon prepared by high rate dc planar magnetron reactive sputtering," *Journal of Applied Physics*, vol. 55, no. 12, p. 4232, 1984. [Online]. Available: <http://scitation.aip.org/content/aip/journal/jap/55/12/10.1063/1.333024>
- [85] M. C. M. Lee and M. C. Wu, "Thermal annealing in Hydrogen for 3-D profile transformation on silicon-on-insulator and sidewall roughness reduction," *Journal of Microelectromechanical Systems*, vol. 15, no. 2, pp. 338–343, 2006.
- [86] A. D. Bristow, N. Rotenberg, and H. M. van Driel, "Two-photon absorption and Kerr coefficients of silicon for 850-2200 nm," *Applied Physics Letters*, vol. 90, no. 19, p. 191104, 2007.
- [87] A. D. Ellis and J. Zhao, *Impact of Nonlinearities on Fiber Optic Communications*, S. Kumar, Ed. New York, NY: Springer New York, 2011. [Online]. Available: <http://link.springer.com/10.1007/978-1-4419-8139-4>
- [88] R. Salem, M. a. Foster, A. C. Turner, D. F. Geraghty, M. Lipson, and A. L. Gaeta, "Signal regeneration using low-power four-wave mixing on silicon chip," *Nature Photonics*, vol. 2, no. 1, pp. 35–38, dec 2007. [Online]. Available: <http://www.nature.com/doifinder/10.1038/nphoton.2007.249>
- [89] W. Astar, J. B. Driscoll, X. Liu, J. I. Dadap, W. M. J. Green, Y. a. Vlasov, G. M. Carter, and R. M. Osgood, "Conversion of 10 Gb/s NRZ-OOK to RZ-OOK utilizing XPM in a Si nanowire." *Optics express*, vol. 17, no. 15, pp. 12 987–99, jul 2009. [Online]. Available: <http://www.ncbi.nlm.nih.gov/pubmed/19654703>

- [90] H. Hu, H. Ji, M. Galili, M. Pu, K. Yvind, P. Jeppesen, and L. K. Oxenløwe, "160 Gbit/s optical packet switching using a silicon chip," in *IEEE Photonics Conference 2012*. IEEE, sep 2012, pp. 915–916. [Online]. Available: <http://ieeexplore.ieee.org/lpdocs/epic03/wrapper.htm?arnumber=6359293>
- [91] A. Chralyvy, "Plenary paper: The coming capacity crunch," in *2009 35th European Conference on Optical Communication*, 2009, p. 8007. [Online]. Available: [Chralyvy2009](#)
- [92] M. Nakazawa, T. Hirooka, P. Ruan, and P. Guan, "Ultrahigh-speed "orthogonal" TDM transmission with an optical Nyquist pulse train." *Optics express*, vol. 20, no. 2, pp. 1129–40, jan 2012. [Online]. Available: <http://www.ncbi.nlm.nih.gov/pubmed/22274458>
- [93] H. Hu, D. Kong, E. Palushani, J. D. Andersen, A. Rasmussen, B. M. Sørensen, M. Galili, H. C. H. Mulvad, K. J. Larsen, S. Forchhammer, P. Jeppesen, and L. K. Oxenløwe, "1.28 Tbaud Nyquist Signal Transmission using Time-Domain Optical Fourier Transformation based Receiver," in *CLEO: Science and Innovations 2013*, San Jose, 2013.
- [94] H. Hu, H. Ji, M. Galili, M. Pu, C. Peucheret, H. Christian H Mulvad, K. Yvind, J. M. Hvam, P. Jeppesen, and L. K. Oxenløwe, "Ultra-high-speed wavelength conversion in a silicon photonic chip." *Optics express*, vol. 19, no. 21, pp. 19 886–94, oct 2011. [Online]. Available: <http://www.ncbi.nlm.nih.gov/pubmed/21996996>
- [95] W. D. Sacher, Y. Huang, G.-Q. Lo, and J. K. S. Poon, "Multilayer Silicon Nitride-on-Silicon Integrated Photonic Platforms and Devices," *Journal of Lightwave Technology*, vol. 33, no. 4, pp. 901–910, 2015. [Online]. Available: <http://ieeexplore.ieee.org/lpdocs/epic03/wrapper.htm?arnumber=7014292>
- [96] C. R. Doerr, L. L. Buhl, L. Chen, and N. Dupuis, "Monolithic flexible-grid 1 & 2 wavelength-selective switch in silicon photonics," *Journal of Lightwave Technology*, vol. 30, no. 4, pp. 473–478, 2012. [Online]. Available: <http://ieeexplore.ieee.org/lpdocs/epic03/wrapper.htm?arnumber=6062626>
- [97] P. Rabiei, W. H. Steier, C. Zhang, and L. R. Dalton, "Polymer micro-ring filters and modulators," *Journal of Lightwave Technology*, vol. 20, no. 11, pp. 1968–1975, 2002.

- [98] W. D. Sacher and J. K. S. Poon, "Characteristics of microring resonators with waveguide-resonator coupling modulation," *Journal of Lightwave Technology*, vol. 27, no. 17, pp. 3800–3811, 2009.
- [99] W. Sacher, W. Green, and S. Assefa, "Coupling modulation of microrings at rates beyond the linewidth limit," *Optics Express*, vol. 21, no. 8, pp. 242–249, 2013. [Online]. Available: <http://www.opticsinfobase.org/abstract.cfm?URI=oe-21-8-9722>
- [100] S. Feng, X. Luo, S. Du, and A. W. Poon, "Electro-optical tunable time delay and advance in a silicon feedback-microring resonator." *Optics letters*, vol. 36, no. 7, pp. 1278–1280, 2011.
- [101] L. Zhou and A. W. Poon, "Electrically reconfigurable silicon microring resonator-based filter with waveguide-coupled feedback." *Optics express*, vol. 15, no. 15, pp. 9194–9204, 2007.
- [102] W. Green, R. Lee, G. Derose, A. Scherer, and A. Yariv, "Hybrid InGaAsP-InP Mach-Zehnder Racetrack Resonator for Thermo-optic Switching and Coupling Control." *Optics express*, vol. 13, no. 5, pp. 1651–1659, 2005.
- [103] T. Inukai and K. Ono, "Optical Characteristics of Amorphous Silicon Nitride Thin Films Prepared by Electron Cyclotron Resonance Plasma Chemical Vapor Deposition," *Japanese Journal of Applied Physics*, vol. 33, no. Part 1, No. 5A, pp. 2593–2598, 1994.
- [104] J. S. Levy, A. Gondarenko, M. A. Foster, A. C. Turner-Foster, A. L. Gaeta, and M. Lipson, "CMOS-compatible multiple-wavelength oscillator for on-chip optical interconnects," *Nature Photonics*, vol. 4, no. 1, pp. 37–40, 2010. [Online]. Available: <http://www.nature.com/doifinder/10.1038/nphoton.2009.259>
- [105] B. Zheng, C. Zhou, Q. Wang, Y. Chen, and W. Xue, "Deposition of low stress silicon nitride thin film and its application in surface micromachining device structures," *Advances in Materials Science and Engineering*, vol. 2013, 2013.
- [106] A. Yariv, "Critical coupling and its control in optical waveguide-resonator systems," *IEEE Photonics Technology Letters*, vol. 14, no. 4, pp. 483–485, 2002.

- [107] S. Selvaraja, G. Murdoch, A. Milenin, C. Delvaux, P. Ong, S. Pathak, D. Vermeulen, G. Sterckx, G. Winroth, P. Verheyen, G. Lepage, W. Bogaerts, R. Baets, J. Van Campenhout, and P. Absil, “Advanced 300-mm Waferscale Patterning for Silicon Photonics Devices with Record Low Loss and Phase Errors,” in *17th OptoElectronics and Communications Conference (OECC)*, 2012, pp. PDP2–2 p15.
- [108] P. Alipour, A. A. Eftekhari, A. H. Atabaki, Q. Li, S. Yegnanarayanan, C. K. Madsen, and A. Adibi, “Fully reconfigurable compact RF photonic filters using high-Q silicon microdisk resonators.” *Optics express*, vol. 19, no. 17, pp. 15 899–15 907, 2011. [Online]. Available: <http://www.ncbi.nlm.nih.gov/pubmed/21934953>
- [109] D. Dai, Z. Wang, J. F. Bauters, M.-C. Tien, M. J. R. Heck, D. J. Blumenthal, and J. E. Bowers, “Low-loss Si₃N₄ arrayed-waveguide grating (de)multiplexer using nano-core optical waveguides,” *Optics Express*, vol. 19, no. 15, p. 14130, 2011.
- [110] J. S. Levy, A. Gondarenko, A. C. Turner-Foster, M. A. Foster, A. L. Gaeta, and M. Lipson, “Four-wave mixing in integrated silicon nitride waveguides,” in *Conference on Lasers and Electro-Optics*, 2009.
- [111] J. Komma, C. Schwarz, G. Hofmann, D. Heinert, and R. Nawrodt, “Thermo-optic coefficient of silicon at 1550 nm and cryogenic temperatures,” *Applied Physics Letters*, vol. 101, no. 4, pp. 4–8, 2012.
- [112] D. E. Aspnes and A. A. Studna, “Dielectric functions and optical parameters of Si, Ge, GaP, GaAs, GaSb, InP, InAs, and InSb from 1.5 to 6.0 eV,” *Physical Review B*, vol. 27, no. 2, pp. 985–1009, 1983.
- [113] A. W. Snyder and J. D. Love, “Mode coupling,” in *Optical Waveguide Theory*. Boston, MA: Springer US, 1983, pp. 542–552. [Online]. Available: http://link.springer.com/10.1007/978-1-4613-2813-1_{_}29
- [114] D. Ding, M. J. a. de Dood, J. F. Bauters, M. J. R. Heck, J. E. Bowers, and D. Bouwmeester, “Fano resonances in a multimode waveguide coupled to a high-Q silicon nitride ring resonator.” *Optics express*, vol. 22, no. 6, pp. 6778–90, 2014. [Online]. Available: <http://www.ncbi.nlm.nih.gov/pubmed/24664026>